



Title	Numerical Investigation of the Aerodynamics of a Golf Ball
Author(s)	李, 景
Citation	北海道大学. 博士(工学) 甲第12376号
Issue Date	2016-06-30
DOI	10.14943/doctoral.k12376
Doc URL	http://hdl.handle.net/2115/62487
Type	theses (doctoral)
File Information	Jing_Li.pdf



[Instructions for use](#)

Numerical Investigation of the Aerodynamics of a Golf Ball

by

Li Jing

Dissertation

Presented to the Division of Mechanical and Space Engineering

Graduate School of Engineering

Hokkaido University

in partial fulfillment of the requirements for the degree of

Doctor of Philosophy

Hokkaido University

Japan

June 2016

Acknowledgements

I would like to first express my most sincere gratitude to my supervisor Professor Nobuyuki Oshima for his patience, professional guidance, invaluable support and encouragement throughout the whole work.

My sincere appreciation also goes to Professor Makoto Tsubokura for his expertise, enormous support and great guidance to this work through all these years.

I am also grateful to Professor Y. Murai, Professor M. Watanabe and Associate Professor H. Terashima for their work as the members of the examination committee.

I would like to thank all the members in our laboratory for your kindness and warm-hearted help. Special thanks go to Dr. Ikeda for his great support in many aspects, Mr. Johnson for his efforts to revising my English language, and Mr. Dani for his important advices.

I also wish to thank Sumitomo Rubber Industries, Ltd. who provided the golf ball model used in the present study. Special thanks go to Dr. Tsunoda and Dr. Kim for their support.

My thanks also go to Hokkaido University, especially to the staffs in E3 office and academic office who offered endless help to foreign students.

I would like to express my special gratitude to the China Scholarship Council (CSC) for the financial support during my Ph.D. study. My thanks also go to Chongqing University.

感谢始终关心和支持着我的父亲母亲。

Table of Contents

Abstract.....	I
List of Figures and Tables.....	IV
List of Symbols.....	XII
Chapter 1: Introduction.....	1
1.1 Background and motivation.....	1
1.2 Objectives.....	3
1.3 Literature review.....	4
1.3.1 Flow past smooth spheres.....	4
1.3.2 Flow past roughness spheres.....	8
1.3.3 Flow past golf balls.....	8
Chapter 2: Numerical Methods.....	11
2.1 Large-eddy simulation.....	11
2.2 Governing equations of large-eddy simulation.....	12
2.3 Discretization and numerical schemes.....	14
2.4 Arbitrary Lagrangian-Eulerian Method.....	15
2.5 Definition of coordinate system, force direction and force coefficients.....	16
2.6 Geometry and mesh generation.....	18
2.7 Computation domains and boundary conditions.....	21
2.8 The reproducing of self-spinning motion.....	23
2.9 Software and hardware.....	24
Chapter 3: Flow past the stationary golf ball and smooth sphere.....	27
3.1 Drag crisis of flow past the golf ball.....	27
3.2 Flow visualization around the stationary golf ball and smooth sphere.....	32
3.3 Mechanism of drag reduction by golf ball dimples.....	35
3.4 Development of the unsteady aerodynamic forces and wake flow structure.....	44
3.4.1 Transient lateral force and wake flow structure in the subcritical regime.....	44
3.4.2 Transient lateral force and wake flow structure in the critical regime.....	49
3.4.3 Transient lateral force and wake flow structure in the supercritical regime.....	53
Chapter 4: Flow past the self-spinning golf ball and smooth sphere.....	61

4.1 Variation of the drag and lift coefficients	61
4.2 Flow visualizations around the self-spinning golf ball and smooth sphere	63
4.3 Mechanism of the ordinary and negative Magnus effect	67
4.4 Development of the unsteady aerodynamic forces and wake flow structure	75
4.4.1 Transient lateral force and wake flow structure in the subcritical regime.....	77
4.4.2 Transient lateral force and wake flow structure in the critical regime	82
4.4.3 Transient lateral force and wake flow structure in the supercritical regime	86
Chapter 5: Conclusions	93
5.1 General conclusions	93
5.2 Future work	96
References	97

Abstract

As one of the most appealing topics relating to both the fundamental fluid dynamics and science behind sports ball games, the aerodynamics of a golf ball has been progressively receiving attention in the past decades. Two important factors that strongly affect the golf ball aerodynamics are the surface roughness introduced by the dimples and the golf ball's self-spinning motion. The former is usually discussed in terms of the enhancement of the drag crisis, which remarkably reduces the drag force and increases the flying distance in the direction against the incoming flow, whereas the latter is considered to directly affect the flying trajectory through the additional lift force generated as a result of the Magnus effect. However, there are still some open questions regarding the golf ball aerodynamics which remain not fully understood, such as the mechanism of drag reduction by dimples, the ordinary/negative Magnus effect on golf balls, the lateral force variation on both stationary and self-spinning golf balls, and the transient features of golf ball aerodynamics. Accordingly, the aims of the present research are to numerically study the above unresolved questions, and achieve a more comprehensive understanding of the aerodynamics of a golf ball.

The geometry models used in the present research are a real golf ball product, and a smooth sphere for the sake of comparison. For both models, triangular meshes are generated on the geometry surface while prism layers are allocated along the normal-wall direction of the surface. The numerical method adopted for the flow simulation in the present study is the Large-eddy simulation (LES) method. The dynamic subgrid-scale eddy viscosity model is used for properly resolving the boundary layer flow. Particularly, the arbitrary Lagrangian-Eulerian (ALE) method was applied to impose the self-spinning motion on the golf ball, whereas for the smooth sphere, the rotating motion was imposed by directly adding an angular velocity on the geometry surface as a boundary condition.

The simulation results obtained in the present study successfully reproduced the drag crisis of the stationary golf ball at a visibly lower critical Reynolds number than the smooth sphere, which agrees very well with the experimental data. The detailed analysis on the local flow behaviors inside individual dimples reveals the mechanism responsible for the drag reduction of the golf ball occurring at a lower Reynolds number when compared to the smooth sphere. It is observed that the flow locally separates on the leading edges of some dimples when it passes over the golf ball surface in the supercritical regime. The locally detached shear layer quickly becomes unstable and oscillates considerably as it travels further

downstream. Meanwhile, small-scale vortices are generated inside the individual dimples. As a result of the shear layer instability, the momentum in the near-wall flow increases, and with the increased momentum, the flow that reattaches on the trailing edges of the dimples is able to overcome the adverse pressure gradient more and travel further downstream, which consequently delays the full flow separation.

The investigation of the lateral force variation and wake flow structure for the stationary cases shows that for both the golf ball and smooth sphere, the lateral forces change irregularly with time in both the magnitude and direction in the subcritical regime, and a large-scale wave motion is pronounced in the wake areas of both models with a wavelength similar to each other. In the critical regime, the lateral forces acting on both models exhibit a larger magnitude of oscillation when compared to the subcritical cases, and the directions of the lateral forces differ irregularly with time. In the supercritical regime, both models are subjected to a nonzero lateral force during a long time interval, and the lateral force direction exhibits a rotation trend with time. However, the magnitude of the lateral force acting on the golf ball is visibly smaller when compared to the smooth sphere, indicating a suppression of the lateral force in the supercritical golf ball case.

The ordinary Magnus effect and negative Magnus effect were successfully reproduced for both the self-spinning golf ball and smooth sphere. In the subcritical and supercritical regimes, the boundary layers on the top side, where the geometry surface rotates with the approaching flow, and the bottom side, where the geometry surface rotates against the approaching flow, exist in the same state. As a result of the self-spinning motion, the near-wall flow gains momentum on the top side while it loses momentum on the bottom side. This further leads to the flow separating at a position further downstream on the top side than on the bottom side, which consequently gives rise to a positive Magnus force acting on both of the models. In contrast, in the critical regime, the boundary layer on the top side stays laminar whereas on the bottom side it becomes turbulent. This is attributed to the locally higher relative Reynolds number on the bottom side which makes the flow on this side more sensitive to perturbations and consequently promotes the laminar-turbulent boundary layer transition. As a result, the flow separates at a position further downstream on the bottom side than on the top side, which consequently produces a negative Magnus force acting on both models.

The investigation of the lateral force variation and wake flow structure for the self-spinning cases shows that for both models in the subcritical regime, the variation of the lateral force is more regular when compared to the stationary cases, and the lateral force

oscillation is more dominant in the lift force direction than in the side force direction. In the critical regime, the lateral force acting on the rotating golf ball experiences a visibly smaller oscillation when compared to the stationary case, whereas the lateral force acting on the rotating smooth sphere exhibits a considerable oscillation in the lift force direction. In the supercritical regime, the variation of the lateral force is more regular for both rotating models when compared to the stationary cases. Interestingly, the lift force acting on the golf ball is around 40% smaller when compared to the smooth sphere, while the drag force acting on these two models remains comparable.

List of Figures and Tables

Fig.1-1 Drag crisis of a smooth sphere as a function of Reynolds number ²	2
Fig.2-1 Schematic diagram of eddies of different sizes contained in a turbulence flow and the corresponding resolved scale in LES and DNS ²²	12
Fig.2-2 Schematic diagram of a two-dimensional vertex-centered control volume.	14
Fig.2-3 Coordinate system and force direction	17
Fig.2-4 Geometry details of the golf ball respectively visualized from the (a) upstream view; (b) negative side force view; (c) positive side force view.	19
Fig.2-5 Details of the numerical grid in the vicinity of individual dimples	20
Fig.2-6 Computation domain used for the stationary smooth sphere, self-spinning smooth sphere, and stationary golf ball cases.	21
Fig.2-7 Computation domain used for the self-spinning golf ball cases	22
Fig.2-8 Translation of the spherical computation domain with time for the self-spinning golf ball cases; the moving direction is from the right to the left; $t_1 < t_2 < t_3$	25
Fig.2-9 Change of the golf ball's angular position at the corresponding time step shown in Fig.2-8; the golf ball is rotating clockwise; $t_1 < t_2 < t_3$	26
Fig.3-1 Comparison of the drag coefficients for golf balls and smooth spheres; Lines: experimental results; Symbols: numerical results	27
Fig.3-2 Time-averaged surface pressure distributions on the golf ball (obtained in the section $y=0$; see Fig.2-4 (a) in Chapter 2) and the smooth spheres in the (a) subcritical regime; (b) critical regime; (c) supercritical regime; Lines: numerical simulation results; Symbols: experimental results.	29
Fig.3-3 Comparison of the time-averaged surface pressure distribution on the golf ball obtained respectively in the plane $y=0$ and plane y_v (see Fig.2-4 (a) in Chapter 2) along the same polar angular direction at the (a) subcritical regime; (b) critical regime; (c) supercritical regime.	31
Fig.3-4 Instantaneous surface pressure distribution and contours of the instantaneous non-dimensional streamwise velocity distribution around the separation points of the golf ball and smooth sphere viewed in the plane $y=0$	33

Fig.3-5 Time-averaged surface pressure distribution and time-averaged non-dimensional streamwise velocity distribution in the wake area of the golf ball and smooth sphere viewed in the plane $y=0$ 34

Fig.3-6 Time-averaged non-dimensional streamwise velocity distribution around the golf ball dimples at $Re=1.1 \times 10^5$ viewed on the y_v plane: (a) complete view from 65° to 115° ; (b) detailed view from 65° to 90° ; (c) detailed view from 90° to 115° ; the parts of the golf ball surface colored by ‘yellow’ represent a positive streamwise velocity on the prism layer cell attached on the boundary surface, indicating a flow attachment at corresponding areas; the parts colored by ‘gray’ represent a negative streamwise velocity on the prism layer cell attached on the boundary surface, indicating a flow detachment at corresponding areas. 36

Fig.3-7 Time-averaged surface pressure distribution on the golf ball obtained respectively in the plane $y=0$ and plane y_v (see Fig.2-4 (a) in Chapter 2) along the same polar angular direction from 25° to 85° ; (a) $Re=4.3 \times 10^4$; subcritical regime; (b) $Re=1.1 \times 10^5$; supercritical regime. 38

Fig.3-8 The distribution of the instantaneous velocity vectors inside the dimple spanning from 32.5° to 43° ; the incoming flow moves from the left to right; (a) Indication of position of the dimple spanning from 32.5° to 43° ; (b) $Re=4.3 \times 10^4$; subcritical regime; (c) $Re=1.1 \times 10^5$; supercritical regime. 39

Fig.3-9 The distribution of the instantaneous velocity vectors inside the dimple spanning from 65° to 75° ; the incoming flow moves from the left to right; (a) Indication of position of the dimple spanning from 65° to 75° ; (b) $Re=4.3 \times 10^4$; subcritical regime; (c) $Re=1.1 \times 10^5$; supercritical regime. 40

Fig.3-10 Profiles of the time-averaged streamwise velocity and the r.m.s fluctuation of the streamwise velocity measured above the dimple spanning from 65° to 75° at $Re=1.1 \times 10^5$: (a) position 1-4 for profile plotting; (b) profiles obtained at position 1; (c) profiles obtained at position 2; (d) profiles obtained at position 3; (e) profiles obtained at position 4. 41

Fig.3-11 Contours of the instantaneous azimuthal vorticity viewed on the y_v plane at different Reynolds numbers; the vorticity direction is out-of-plane; (a) $Re=4.3 \times 10^4$, subcritical; (b) $Re=7.5 \times 10^4$, critical; (c) $Re=1.1 \times 10^5$, supercritical; (d) $Re=1.7 \times 10^5$, supercritical. 43

Table.3-1 Summary of the time-averaged mean value and standard deviation (s.d.) of the side force coefficient C_s and lift force coefficient C_l for the stationary golf ball and smooth sphere at the subcritical, critical and supercritical Reynolds numbers. 44

Fig.3-12 Time series of the drag and lateral force coefficients for the stationary golf ball at subcritical $Re=4.3 \times 10^4$ after the flow reached a statistically steady state: (a) temporal evolution of the drag coefficient C_d , side force coefficient C_s and lift coefficient C_l ; (b) phase diagram of C_s and C_l , the red

point represents the resultant lateral force at the non-dimensional moment indicated in Fig.3-14; the angle α indicates the instantaneous direction of the resultant lateral force looking from the downstream view of the geometry; (c) power spectrum of the side force coefficient C_s and lift coefficient C_l 45

Fig.3-13 Time series of the drag and lateral force coefficients for the stationary smooth sphere at subcritical $Re=1.0 \times 10^4$ after the flow reached a statistically steady state: (a) temporal evolution of the drag coefficient C_d , side force coefficient C_s and lift coefficient C_l ; (b) phase diagram of C_s and C_l , the red point represents the resultant lateral force at the non-dimensional moment indicated in Fig.3-15; (c) power spectrum of the side force coefficient C_s and lift coefficient C_l 46

Fig.3-14 Visualization of the instantaneous vortical structures in the wake area of the stationary golf ball at $Re=4.3 \times 10^4$ using ISO surface of Q ($Ut/D=21.5$, the resultant lateral force at this moment is indicated in Fig.3-12 (b) by the red point). 47

Fig.3-15 Visualization of the instantaneous vortical structures in the wake area of the stationary smooth sphere at $Re=1.0 \times 10^4$ using ISO surface of Q ($Ut/D=21.5$, the resultant lateral force at this moment is indicated in Fig.3-13 (b) by the red point). 48

Fig.3-16 Time-dependent trace of the instantaneous vortical structures around the stationary golf ball at $Re=4.3 \times 10^4$ visualized from the upstream view. 49

Fig.3-17 Time series of the drag and lateral force coefficients for the stationary golf ball at $Re=7.5 \times 10^4$ after the flow reached a statistically steady state: (a) temporal evolution of the drag coefficient C_d , side force coefficient C_s and lift coefficient C_l ; (b) phase diagram of C_s and C_l , the red point represents the resultant lateral force at the non-dimensional moment indicated in Fig.3-19; (c) power spectrum of the side force coefficient C_s and lift coefficient C_l 50

Fig.3-18 Time series of the drag and lateral force coefficients for the stationary smooth sphere at $Re=2.0 \times 10^5$ after the flow reached a statistically steady state: (a) temporal evolution of the drag coefficient C_d , side force coefficient C_s and lift coefficient C_l ; (b) phase diagram of C_s and C_l , the red point represents the resultant lateral force at the non-dimensional moment indicated in Fig.3-20; (c) power spectrum of the side force coefficient C_s and lift coefficient C_l 51

Fig.3-19 Visualization of the instantaneous vortical structures in the wake area of the stationary golf ball at $Re=7.5 \times 10^4$ using ISO surface of Q ($Ut/D=20.8$, the resultant lateral force at this moment is indicated in Fig.3-17 (b) by the red point). 52

Fig.3-20 Visualization of the instantaneous vortical structures in the wake area of the stationary smooth sphere at $Re=2.0 \times 10^5$ using ISO surface of Q ($Ut/D=25.5$, the resultant lateral force at this moment is indicated in Fig.3-18 (b) by the red point).	52
Fig.3-21 Time series of the drag and lateral force coefficients for the stationary golf ball at $Re=1.1 \times 10^5$ after the flow reached a statistically steady state: (a) temporal evolution of the drag coefficient C_d , side force coefficient C_s and lift coefficient C_l ; (b) phase diagram of C_s and C_l , the red point represents the resultant lateral force at the non-dimensional moment indicated in Fig.3-23; (c) power spectrum of the side force coefficient C_s and lift coefficient C_l	54
Fig.3-22 Time series of the drag and lateral force coefficients for the stationary smooth sphere at $Re=1.14 \times 10^6$ after the flow reached a statistically steady state: (a) temporal evolution of the drag coefficient C_d , side force coefficient C_s and lift coefficient C_l ; (b) phase diagram of C_s and C_l , the red point represents the resultant lateral force at the non-dimensional moment indicated in Fig.3-24; (c) power spectrum of the side force coefficient C_s and lift coefficient C_l	55
Fig.3-23 Visualization of the instantaneous vortical structures in the wake area of the stationary golf ball at $Re=1.1 \times 10^5$ using ISO surface of Q ($Ut/D=28.9$, the resultant lateral force at this moment is indicated in Fig.3-21 (b) by the red point).	56
Fig.3-24 Visualization of the instantaneous vortical structures in the wake area of the stationary smooth sphere at $Re=1.14 \times 10^6$ using ISO surface of Q ($Ut/D=31.9$, the resultant lateral force at this moment is indicated in Fig.3-22 (b) by the red point).	56
Fig.3-25 Streamwise vorticity component in the wake flow of the stationary golf ball viewed in the crossflow plane at: (a) $x/D=1.0$; (b) $x/D=1.5$; (c) $x/D=3.0$; $Re=1.1 \times 10^5$ ($Ut/D=28.9$).	57
Fig.3-26 Streamwise vorticity component in the wake flow of the stationary smooth sphere viewed in the crossflow plane at: (a) $x/D=1.0$; (b) $x/D=1.5$; (c) $x/D=3.0$; $Re=1.14 \times 10^6$ ($Ut/D=31.9$).	57
Fig.3-27 Streamlines around the stationary golf ball at $Re=1.1 \times 10^5$ viewed from: (a) -y view; (b) +z view; (c) an isometric view.	59
Fig.3-28 Streamlines around the stationary smooth sphere at $Re=1.14 \times 10^6$ viewed from: (a) -y view; (b) +z view; (c) an isometric view.	60
Fig.4-1 Comparison of the drag coefficients between the self-spinning and stationary cases for the golf ball and smooth sphere.	62

Fig.4-2 Lift coefficients of the corresponding self-spinning golf ball and smooth sphere cases shown in Fig.4-1.....	62
Fig.4-3 Instantaneous surface pressure distribution and non-dimensional streamwise velocity distribution in the wake area of the self-spinning golf ball at the: (a) subcritical, (b) critical, (c) supercritical Reynolds numbers; incoming flow is from $-x$ to $+x$; backspin motion is imposed around 'y' axis; the velocity distribution is viewed in section $y=0$	65
Fig.4-4 Contours of the instantaneous azimuthal vorticity viewed in section $y=0$ around the separation point on the top side of the corresponding rotating golf balls shown in Fig.4-3; the red arrows indicate the positions of flow separation.	65
Fig.4-5 Contours of the instantaneous azimuthal vorticity viewed in section $y=0$ around the separation point on the bottom side of the corresponding rotating golf balls shown in Fig.4-3; the red arrows indicate the positions of flow separation.....	65
Fig.4-6 Instantaneous surface pressure distribution and non-dimensional streamwise velocity distribution in the wake area of the self-spinning smooth sphere at the: (a) subcritical, (b) critical, (c) supercritical Reynolds numbers; incoming flow is from $-x$ to $+x$; backspin motion is imposed around 'y' axis; the velocity distribution is viewed in section $y=0$	66
Fig.4-7 Contours of the instantaneous azimuthal vorticity viewed in section $y=0$ around the separation point on the top side of the corresponding rotating smooth spheres shown in Fig.4-6; the red arrows indicate the positions of flow separation.....	66
Fig.4-8 Contours of the instantaneous azimuthal vorticity viewed in section $y=0$ around the separation point on the bottom side of the corresponding rotating smooth spheres shown in Fig.4-6; the red arrows indicate the positions of flow separation.....	66
Fig.4-9 Instantaneous surface pressure distribution obtained in section $y=0$ respectively along the top side and bottom side of the golf balls displayed in Fig.4-3.	67
Fig.4-10 Instantaneous surface pressure distribution obtained in section $y=0$ respectively along the top side and bottom side of the smooth spheres displayed in Fig.4-6.....	67
Fig.4-11 Visualization of the instantaneous vortical structures around the golf ball using ISO surface of Q respectively viewed from the: (a) top view; (b) bottom view; $Re=4.3 \times 10^4$, subcritical.....	69
Fig.4-12 Visualization of the instantaneous vortical structures around the golf ball using ISO surface of Q respectively viewed from the: (a) top view; (b) bottom view; $Re=7.5 \times 10^4$, critical.	70

Fig.4-13 Visualization of the instantaneous vortical structures around the golf ball using ISO surface of Q respectively viewed from the: (a) top view; (b) bottom view; $Re=1.1 \times 10^5$, supercritical..... 71

Fig.4-14 Contours of the instantaneous azimuthal vorticity viewed on the y_v plane at $Re=7.5 \times 10^4$; $Ut/D=6.8$; the vorticity direction is out-of-plane. 72

Fig.4-15 Contours of the instantaneous azimuthal vorticity viewed on the y_v plane at $Re=7.5 \times 10^4$; $Ut/D=10.3$; the vorticity direction is out-of-plane. 72

Fig.4-16 Contours of the instantaneous azimuthal vorticity viewed on the y_v plane at $Re=7.5 \times 10^4$; $Ut/D=13.8$; the vorticity direction is out-of-plane. 73

Fig.4-17 Contours of the instantaneous azimuthal vorticity viewed on the y_v plane at $Re=7.5 \times 10^4$; $Ut/D=17.3$; the vorticity direction is out-of-plane. 73

Fig.4-18 Contours of the instantaneous azimuthal vorticity viewed on the y_v plane at $Re=7.5 \times 10^4$; $Ut/D=20.8$; the vorticity direction is out-of-plane. 74

Fig.4-19 Contours of the instantaneous azimuthal vorticity viewed on the y_v plane at $Re=7.5 \times 10^4$; $Ut/D=24.3$; the vorticity direction is out-of-plane. 74

Table.4-1 Summary of the time-averaged mean value and standard deviation (s.d.) of the drag coefficient C_d , side force coefficient C_s , lift coefficient C_l , and the ratio of lift/drag for the self-spinning golf ball and smooth sphere, and the change of the drag coefficients in the rotating cases (C_d) relative to the stationary cases (C_{d_sta})..... 75

Fig.4-20 Schematic diagram of the time-averaged drag force, lift force and the corresponding resultant force in the drag-lift plane acting on the golf ball and smooth sphere; blue vector: drag force normalized by its magnitude, with unit length for all the cases; red vector: lift force normalized by the magnitude of drag force, with the length equaling C_l/C_d ; black vector: the resultant force of the drag and lift forces. 76

Fig.4-21 Time series of the drag, side force and lift coefficients for the self-spinning golf ball at subcritical $Re=4.3 \times 10^4$ after the flow reached a statistically steady state: (a) temporal evolution of the drag coefficient C_d , side force coefficient C_s and lift coefficient C_l ; (b) phase diagram of C_s and C_l , the red point represents the resultant lateral force at the non-dimensional moment indicated in Fig.4-23; the red dash line represents the corresponding variation in the stationary golf ball case at the same Reynolds number; (c) power spectrum of the side force coefficient C_s and lift coefficient C_l 79

Fig.4-22 Time series of the drag, side force and lift coefficients for the self-spinning smooth sphere at subcritical $Re=1.0\times 10^4$ after the flow reached a statistically steady state: (a) temporal evolution of the drag coefficient C_d , side force coefficient C_s and lift coefficient C_l ; (b) phase diagram of C_s and C_l , the red point represents the resultant lateral force at the non-dimensional moment indicated in Fig.4-24; the red dash line represents the corresponding variation in the stationary smooth sphere case at the same Reynolds number; (c) power spectrum of the side force coefficient C_s and lift coefficient C_l 80

Fig.4-23 Visualization of the instantaneous vortical structures in the wake area of the self-spinning golf ball at $Re=4.3\times 10^4$ using ISO surface of Q ($Ut/D=4.9$, the resultant lateral force at this moment is indicated in Fig.4-21 (b) by the red point). 81

Fig.4-24 Visualization of the instantaneous vortical structures in the wake area of the self-spinning smooth sphere at $Re=1.0\times 10^4$ using ISO surface of Q ($Ut/D=21.5$, the resultant lateral force at this moment is indicated in Fig.4-22 (b) by the red point). 81

Fig.4-25 Time series of the drag, side force and lift coefficients for the self-spinning golf ball at critical $Re=7.5\times 10^4$ after the flow reached a statistically steady state: (a) temporal evolution of the drag coefficient C_d , side force coefficient C_s and lift coefficient C_l ; (b) phase diagram of C_s and C_l , the red point represents the resultant lateral force at the non-dimensional moment indicated in Fig.4-27; the red dash line represents the corresponding variation in the stationary golf ball case at the same Reynolds number; (c) power spectrum of the side force coefficient C_s and lift coefficient C_l 83

Fig.4-26 Time series of the drag, side force and lift coefficients for the self-spinning smooth sphere at critical $Re=2.0\times 10^5$ after the flow reached a statistically steady state: (a) temporal evolution of the drag coefficient C_d , side force coefficient C_s and lift coefficient C_l ; (b) phase diagram of C_s and C_l , the red point represents the resultant lateral force at the non-dimensional moment indicated in Fig.4-28; the red dash line represents the corresponding variation in the stationary smooth sphere case at the same Reynolds number; (c) power spectrum of the side force coefficient C_s and lift coefficient C_l ... 84

Fig.4-27 Visualization of the instantaneous vortical structures in the wake area of the self-spinning golf ball at $Re=7.5\times 10^4$ using ISO surface of Q ($Ut/D=11.7$, the resultant lateral force at this moment is indicated in Fig.4-25 (b) by the red point). 86

Fig.4-28 Visualization of the instantaneous vortical structures in the wake area of the self-spinning smooth sphere at $Re=2.0\times 10^5$ using ISO surface of Q ($Ut/D=14.7$, the resultant lateral force at this moment is indicated in Fig.4-26 (b) by the red point). 86

Fig.4-29 Time series of the drag, side force and lift coefficients for the self-spinning golf ball at supercritical $Re=1.1\times 10^5$ after the flow reached a statistically steady state: (a) temporal evolution of

the drag coefficient C_d , side force coefficient C_s and lift coefficient C_l ; (b) phase diagram of C_s and C_l , the red point represents the resultant lateral force at the non-dimensional moment indicated in Fig.4-31; the red dash line represents the corresponding variation in the stationary golf ball case at the same Reynolds number; (c) power spectrum of the side force coefficient C_s and lift coefficient C_l 88

Fig.4-30 Time series of the drag, side force and lift coefficients for the self-spinning smooth sphere at supercritical $Re=1.14 \times 10^6$ after the flow reached a statistically steady state: (a) temporal evolution of the drag coefficient C_d , side force coefficient C_s and lift coefficient C_l ; (b) phase diagram of C_s and C_l , the red point represents the resultant lateral force at the non-dimensional moment indicated in Fig.4-32; the red dash line represents the corresponding variation in the stationary smooth sphere case at the same Reynolds number; (c) power spectrum of the side force coefficient C_s and lift coefficient C_l 89

Fig.4-31 Visualization of the instantaneous vortical structures in the wake area of the self-spinning golf ball at $Re=1.1 \times 10^5$ using ISO surface of Q ($Ut/D=18.8$, the resultant lateral force at this moment is indicated in Fig.4-29 (b) by the red point). 90

Fig.4-32 Visualization of the instantaneous vortical structures in the wake area of the self-spinning smooth sphere at $Re=1.14 \times 10^6$ using ISO surface of Q ($Ut/D=6.2$, the resultant lateral force at this moment is indicated in Fig.4-30 (b) by the red point). 90

Fig.4-33 Streamwise vorticity component in the wake flow of the self-spinning golf ball viewed in the crossflow plane at: (a) $x/D=1.0$; (b) $x/D=1.5$; (c) $x/D=3.0$; $Re=1.1 \times 10^5$ ($Ut/D=18.8$). 91

Fig.4-34 Streamwise vorticity component in the wake flow of the self-spinning smooth sphere viewed in the crossflow plane at: (a) $x/D=1.0$; (b) $x/D=1.5$; (c) $x/D=3.0$; $Re=1.14 \times 10^6$ ($Ut/D=6.2$). 91

Fig.5-1 Schematic diagram of the mechanism of local flow separation and reattachment inside a golf ball dimple. 94

List of Symbols

- A: projected frontal area
 A^+ : Van Driest damping function constant
 C^+ : logarithmic law constant
 C_d : drag coefficient
 C_{d_sta} : drag coefficient of stationary golf ball/smooth sphere
 C_s : side force coefficient
 C_l : lift coefficient
 C_p : pressure coefficient
 C_{SGS} : Smagorinsky model parameter
D: diameter of golf ball/smooth sphere
 D_g : diameter of golf ball
k: dimple depth
 k^+ : Karman constant
n: normal-wall distance
 p : static pressure
Re: Reynolds number
 R_{dom} : radius of the spherical domain
S: surface of control volume
St: Strouhal number
 S_{ij} : strain rate tensor
t: physical time
 u^+ : dimensionless velocity
u: streamwise velocity
 u_i, u_j : i-th
 u_τ : friction velocity
 u_{rms} : root mean square of streamwise velocity
U: incoming flow velocity
 y^+ : dimensionless wall distance
- n** : outward unit normal-wall vector of control volume surface
 u_d : velocity vector of mesh deformation
 v : velocity vector

δ_B : boundary layer thickness

α :

φ : polar angle

Γ : spin parameter

Δ : filter length scale

ρ : density of fluid

ν : kinematic viscosity of fluid

ν_{SGS} : subgrid-scale eddy viscosity

Ω : volume of control volume

Φ : intensive properties of flow

Δt : time increment between each time step

ω : angular velocity

ω_x : streamwise vorticity component

τ_w : shear stress

Chapter 1: Introduction

1.1 Background and motivation

The game of golf, first played hundreds of years ago, is one of the most popular sports all over the world. Interestingly, in almost all golf tournaments, golf balls are flying in the Reynolds number range in which also most other sports balls are played in their games ¹. On the other hand, as a typical rough sphere, the flow past a golf ball is one of the most interesting topics relating to the fluid dynamics of flow past bluff bodies. Therefore, investigating the aerodynamics of a golf ball will not only gain insights into the understanding of fundamental mechanisms of flow behaviors, but also shed light on the physics behind many other ball sports.

As one of the most basic and relevant topics to the research on the aerodynamics of a golf ball, the flow past a smooth sphere has been studied for a variety of aspects in past years. In the early stages, studies on the flow past spheres mainly focused on the mechanism responsible for the generation of drag force, since it was found that the flow behaviors show remarkable discrepancies from the results predicted by the potential flow theory when it passes over smooth spheres in real life (e.g. the surface pressure could not completely recover at the rear stagnation point). After boundary layer theory was developed in fluid mechanics, most of these discrepancies and the mechanism of the drag force generation could be properly explained as the influence of the boundary layer separation when the flow passes over the geometry surfaces.

The most well-known phenomenon relating to the boundary layer separation to date is probably the “drag crisis” phenomenon of smooth spheres, as shown in Fig.1-1 ². As indicated by the drag crisis phenomenon, when the flow passes a smooth sphere around certain Reynolds number range, the drag force exerted on the sphere reduces sharply with even a slight increase in Reynolds number. This has proved to be directly associated with the boundary layer transition from the laminar state to the turbulent state ², which reveals the influence of Reynolds number on the boundary layer separation and the drag force variation. Correspondingly, the Reynolds number regions around the drag crisis area are respectively defined as the subcritical (before drag crisis), critical (during drag crisis) and supercritical (after drag crisis) Reynolds number regions.

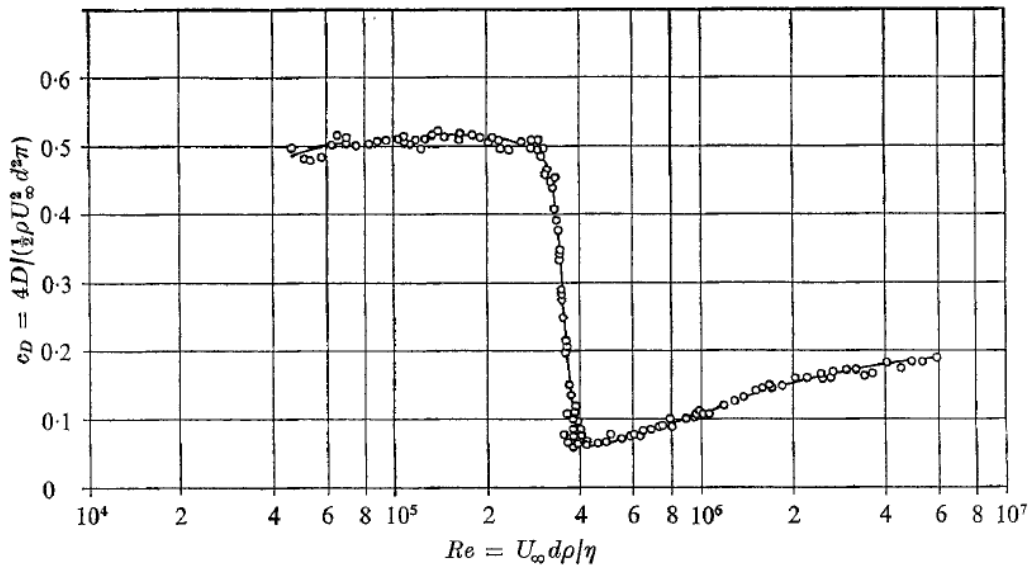


Fig.1-1 Drag crisis of a smooth sphere as a function of Reynolds number ²

Likewise, for the aerodynamics of a golf ball, one of the most important things is the drag crisis phenomenon. It was found in the previous studies ³⁻⁶ that the dimples on the golf ball surface as well as some other convex surface roughness could generally promote the drag crisis, i.e. when compared to a smooth sphere, the drag crisis occurs at a lower Reynolds number when the flow passes over a golf ball or other rough surfaced spheres. With the reduced drag force by dimples, golf balls are able to fly longer distances in the games, which is also one of the primary pursuits in golf ball manufacturing.

Another important factor that remarkably affects golf ball aerodynamics is the self-spinning motion, which a sports ball always experiences while flying in the real-life games. Generally, when a sphere placed in a flow field is rotating, a lift force is imposed on the sphere. This phenomenon is known as the Magnus effect ⁷. However, it was also found that, under some conditions, the lift force points to the direction opposite to the one predicted based on potential flow theory, which is termed as the negative Magnus effect ⁸⁻¹⁰. The lift force generated due to the ordinary/negative Magnus effect directly contributes to the change of flying trajectories of the sports balls. Therefore, to gain insights into the foundation of the effect of the self-spinning motion on the flow behaviors is of particular importance for the golf ball aerodynamics.

Although some studies regarding the effects of dimples and self-spinning motion on the golf ball aerodynamics have been conducted, there are still some questions that remain not clearly understood.

For the effect of dimple roughness on the drag crisis, most of the previous studies primarily focused on the general reproducing of the drag reduction by dimples at Reynolds numbers lower than smooth sphere cases. Despite some discussions more recently³⁻⁵, the underlying mechanism of how dimples lead to a lower critical Reynolds number range for golf balls needs to be investigated in detail.

In addition, to only shed light on the drag coefficient is not enough for comprehensively understanding the golf ball aerodynamics which comprises both the drag force (in the streamwise direction) and lateral force (normal to the streamwise direction). However, the lateral force acting on a golf ball was rarely discussed in previous literatures. Actually, a golfer expects not only a sufficiently long flying distance but also a precise flying trajectory when playing golf, and the lateral force exerted on the golf ball could strongly affect its flying path. Therefore the investigation of the lateral force development is essentially needed for fully understanding a golf ball's aerodynamic performance.

For the effect of self-spinning motion, the main focus in most of the previous studies was towards the ordinary and negative Magnus effects on the rotating smooth spheres, whereas only a few investigations of the rotating golf balls have been conducted. Although the negative lift force, analogous to the smooth spheres, were reported in the rotating golf ball cases^{3, 11}, the underlying mechanism of the negative Magnus effect on a self-spinning golf ball is still not fully understood. In addition, the effect of dimples on the ordinary/negative Magnus effect has not yet been clarified due to little comparison between cases of the rotating golf ball and rotating smooth sphere.

Finally, both the aerodynamics of golf balls and smooth spheres were mainly discussed by means of time-averaged statistics in most of the existing research. The variation of the unsteady aerodynamic forces, which directly reflects the transient features of aerodynamics, was rarely estimated.

1.2 Objectives

Motivated by the unresolved questions mentioned above, the present research work aims to achieve the objectives as following:

1. To reproduce the drag crisis of a stationary golf ball and identify the underlying mechanism of the drag force reduction by golf ball dimples.
2. To investigate the lateral force development of the stationary golf ball and compare the corresponding results with a stationary smooth sphere.

3. To reproduce the ordinary and negative Magnus effects on the self-spinning golf ball, and address the corresponding physical mechanism of the Magnus effect.

4. To investigate the lateral force development of the self-spinning golf ball and compare the corresponding results with the self-spinning smooth sphere.

Particular attention is focused towards the analysis of the unsteady aerodynamics.

1.3 Literature review

1.3.1 Flow past smooth spheres

As one of the most basic and relevant topics to the research of golf balls, the investigation of the flow over smooth spheres is often studied for a variety of different aspects.

1) The drag crisis and wake flow structures

The probably most famous contribution is the experiment of the flow past smooth spheres conducted by Achenbach. In the year of 1971, Achenbach² directly measured the drag coefficient of the smooth spheres at the Reynolds numbers ranging from 5×10^4 to 6×10^6 , and successfully reproduced the whole drag crisis area from the subcritical regime to the supercritical regime. Based on the measurement results, it is indicated that the mechanism of the drag crisis phenomenon is attributed to the shifting of the position of boundary layer separation, which is caused by the boundary layer transition from the laminar state to the turbulent state.

In addition to the measurement of the drag force, the wake structure and vortex shedding pattern behind smooth spheres also received plenty of attentions. Achenbach¹² studied the features of the vortex shedding from the smooth spheres by directly measuring the vortex shedding signals using hot-wire equipment. It is suggested in this study that the vortex separation point rotates along the circumferential direction of the sphere, which is indicated by the phase shift of the vortex shedding signals obtained simultaneously at different azimuthal positions.

By applying oil-flow, smoke and tuft-grid methods, Taneda¹³ provided some impressive observations of the wake flow structures behind a smooth sphere in various Reynolds number regimes. The visualizations primarily lead to two interesting conclusions: At the subcritical and critical Reynolds numbers, a progressive wave motion is distinct in the sphere wake flow, and the plane comprising the streamwise central cross section of the sphere, in which the wave motion performs, rotates randomly about the streamwise axis across the center of the sphere. At the supercritical Reynolds number, a pair of streamwise

line vortices is formed, and this vortex pair rotates irregularly about the streamwise axis across the center of the sphere.

Using dyed water, Sakamoto and Haniu¹⁴ observed the vortex shedding of smooth spheres in the Reynolds number range relatively lower than that in Taneda's experiment. In this study, four regions of the variation of the Strouhal number as a function of Reynolds number was suggested, and the coexistence of the higher and lower Strouhal number modes was also observed in the subcritical Reynolds number regime.

More recently, owing to the improvement of computing technology, numerical methods have been increasingly applied to the corresponding studies.

Constantinescu and Squires¹⁵ investigated the flow over a smooth sphere in both the subcritical and supercritical regimes using detached-eddy simulation. The wake flow structures behind the sphere in both the subcritical and supercritical regimes were also investigated. The remarkable drag reduction as the Reynolds number changes from the subcritical value to the supercritical value was successfully reproduced in their numerical work, along with a good agreement of the surface pressure distribution with the corresponding experimental data. At the subcritical Reynolds number, the shedding of hairpin vortical structures and the progressive wave motion were observed. Moreover, at the supercritical Reynolds number, the considerable asymmetrical wake flow structure and the consequent non-zero lateral force revealed by Taneda were numerically demonstrated. However, Constantinescu and Squires obtained periodically shed hairpin vortices in the supercritical wake flow, which was not captured in Taneda's observation probably because the experimental data was based on the visualization of the averaged wake structure in the time interval of the photographic exposure. On the basis of above results, Constantinescu and Squires proposed that the non-zero mean lateral force exerted on the sphere in the supercritical regime was attributed to the shedding of the hairpin vortices instead of the pair of counter-rotating vortices suggested by Taneda, although the essences in terms of the contribution to the lateral force between these two mechanisms are the same.

Yun et al.¹⁶ provided some insights into the wake structures behind a smooth sphere at different Reynolds numbers in the subcritical regime by conducting large-eddy simulations (LES). The wave motion in the subcritical wake flow and its rotating feature, as proposed by Taneda, were both numerically demonstrated in their study. It is also suggested by the simulation results that the forming of the large-scale wave motion in the wake flow is attributed to the azimuthally different convection velocities of the vortices generated by the shear layer instability.

2) The development of the unsteady aerodynamic forces

In addition to the contributions mentioned above, Constantinescu and Squires¹⁵ further provided the time history data of both the drag coefficient and lateral force coefficients in the subcritical and supercritical regimes, as well as the power spectral analysis of the corresponding aerodynamic forces. It is indicated by the time-dependent force evolution that, at the subcritical Reynolds number, the mean lateral force is close to zero over a sufficiently long time interval, whereas at the supercritical Reynolds number, the mean lateral force is non-zero even during a long time period, which corresponds to the asymmetrical wake flow structures observed in this Reynolds number regime. Furthermore, it is revealed by the results obtained in the spectrum analysis that the Strouhal number associated with large-scale shedding in the supercritical regime is much higher than the one in the subcritical regime, leading to a more rapid rate of the shedding of large-scale vortices at the supercritical Reynolds number compared to the case at the subcritical Reynolds number. Yun et al.¹⁶ also investigated the time histories of the corresponding aerodynamic forces and concluded that the time-averaged lateral force in the subcritical regime was close to zero over a long time interval. In addition, Yun et al. provided some insights into the unsteady lateral force variation using phase diagrams. Based on the features of the total lateral force shown in the phase diagrams, it is indicated that both the magnitude and direction of the total lateral force vary irregularly in time in the subcritical Reynolds number regime.

More recently, Norman and McKeon¹⁷ conducted a comprehensive experimental measurement of the unsteady aerodynamic forces for the flow over a smooth sphere at the Reynolds numbers ranging from the subcritical value to supercritical value. It was found in this study that the large-scale vortex shedding frequency observed in the subcritical case appeared to be no longer distinct in the supercritical case. The measurements also indicate that the large-scale vortex shedding does not have significant effect on the drag force fluctuations for both the subcritical and supercritical cases. More interestingly, it is suggested in this study that the mean lateral force is close to zero at both the subcritical and supercritical Reynolds numbers. The latter conclusion is apparently contradictory to the results obtained by Taneda¹³ and Constantinescu and Squires¹⁵. However, it should be noted that the mean values of the lateral force reported by Norman and McKeon were obtained over more than one thousand dimensionless time units. This time interval was much longer when compared to the previous studies, especially the numerical works by Constantinescu and Squires¹⁵.

3) The ordinary/negative Magnus effect on self-spinning smooth spheres

When a sphere/cylinder placed in the flow field is rotating about an axis normal to the incoming flow direction, a lift force is imposed on the sphere/cylinder. This phenomenon is termed as the Magnus effect ⁷. However, under the conditions of certain Reynolds numbers and spinning speeds, the lift force exerted on the sphere/cylinder points to the direction opposite to the indication based on the ordinary Magnus effect. This phenomenon is known as the negative/negative Magnus effect ^{8-10, 18}.

After the ordinary and negative Magnus effects were revealed, Taneda ⁸ might be the first one who experimentally investigated the detailed conditions under which the negative Magnus effect occurred. It is indicated by the measurements that the negative Magnus force is generated at Reynolds number around 2.5×10^5 (critical regime) with the spin parameter (defined as the ratio of the tangential speed on the sphere to the incoming flow speed) less than 0.6. However, Taneda also pointed out that the Reynolds number range in which the negative Magnus effect occurs may shift depending on the disturbance in the main flow. Based on the indication that the corresponding Reynolds number was in the critical regime, Taneda further proposed the underlying mechanism of the negative Magnus effect on a smooth sphere attributing to the boundary layer transition. It is indicated that the negative Magnus effect occurs because the boundary layer becomes turbulent on the side rotating in the opposite direction to the main flow due to a larger relative speed, whereas the boundary layer stays laminar on the side rotating in the same direction of the main flow.

Due to the difficulty of measuring the near wall flow of a rotating sphere, the mechanism of the negative Magnus effect had not been quantitatively investigated until very recently.

Relying on the improved computing technology, Muto et al. ⁹ numerically investigated the ordinary and negative Magnus effects on a smooth sphere by conducting large-eddy simulations. The results obtained based on the numerical method quantitatively demonstrate the mechanism of the negative Magnus effect. When the sphere was rotating at the critical Reynolds number with a relatively small spin parameter, the boundary layer on the upstream-moving side became turbulent, which consequently delayed the flow separation and the recovery of surface pressure on this side, whereas the boundary layer on the downstream-moving side stayed laminar, leading to a flow separation at more upstream position and a quicker recovery of surface pressure on this side. These flow behaviors correspondingly lead to the generation of negative Magnus force. For the cases in which the

sphere was rotating at some other Reynolds numbers or with different spin parameters, the ordinary Magnus effect appeared.

Kray et al.¹⁹ also investigated the Magnus effect by means of experimental measurement under the conditions of various Reynolds numbers and spin parameters. The curves indicating the variation of the Magnus force as a function of the spin parameter were plotted for cases in different Reynolds number regimes. Additionally, Kray et al. obtained a considerable side force in their experiment when the negative Magnus effect occurred, and correspondingly concluded that the Magnus effect was of three-dimensional features.

More recently, Kim et al.¹⁰ further conducted an experimental investigation of the negative Magnus effect on a rotating smooth sphere. Based on the measurements, Kim et al. proposed an empirical model which can be used for predicting the negative Magnus area and the magnitude of the negative lift force.

1.3.2 Flow past roughness spheres

In addition to the contributions to the flow past smooth sphere, Achenbach also conducted experimental measurement of the flow past roughness spheres⁶. In his study, the surface roughness was obtained by pasting small glass spheres on the surface of the big smooth sphere. The probably most important conclusion made based on the measurements is that, as the height of the roughness elements increases, the critical Reynolds number decreases, whereas the drag coefficient in the supercritical and transcritical regimes increases. Another interesting observation is that the Strouhal number corresponding to the large-scale vortex shedding in the subcritical regime stays almost identical between cases with different roughness height. This indicates a somewhat limited effect of the surface roughness at the subcritical Reynolds numbers.

Norman and McKeon also extended their researches to the roughness sphere by placing isolated cylinder roughness element on the sphere surface²⁰. It is indicated by the measurements that, in the subcritical regime, the roughness element leads to a local delay in flow separation, whereas in the supercritical regime, the roughness element causes a premature flow separation.

1.3.3 Flow past golf balls

Davies¹⁸ might be among the first to experimentally investigate the aerodynamic forces of golf balls by dropping the spinning golf balls in a wind tunnel. However, the drag and lift forces were not directly measured but calculated based on the drift of the balls.

Therefore the results provided in Davies's study was limited, and the negative Magnus effect was not reported for the golf ball cases although a negative lift force was observed in the smooth sphere cases completed in the same study.

The probably most famous contribution to the aerodynamics of golf balls is the experimental measurement conducted by Bearman and Harvey ³. The aerodynamic forces exerted on the golf balls were measured over a wide range of Reynolds number and spin parameter using the wind tunnel technique developed in their study. The measurements reveal three important phenomena: (1) The dimples reduce the drag force at a lower Reynolds number, i.e. leads to a lower critical Reynolds number, when compared to smooth sphere cases, although the reduced drag coefficient is higher than those of smooth spheres. This phenomenon is similar to the corresponding effect of the positive roughness used by Achenbach ⁶. (2) The reduced drag coefficient barely increases as the Reynolds number further increases in the supercritical regime. This phenomenon is very different from the corresponding conclusions in the positive roughness cases. It is suggested by Bearman and Harvey that this difference is because the dimples are effective in tripping boundary layers without causing the thickening of the boundary layer. (3) Under the condition of some specific Reynolds number and spin parameter, the negative Magnus force appears on the spinning golf ball. It is assumed by Bearman and Harvey that, analogous to the smooth sphere cases, the negative lift force acting on the golf ball was generated because the boundary layer on the side spinning against the main flow became turbulent, while the one on the side spinning with the main flow stayed laminar. Moreover, Bearman and Harvey estimated the aerodynamic performance of golf balls with different dimple patterns. The result shows that a hexagonally-dimpled ball has a higher lift force and a lower drag force when compared to a spherically-dimpled ball.

Based on the measurements completed by Bearman and Harvey, Choi et al. ⁴ further investigated the detailed process of how golf ball dimples reduce the drag force at a lower Reynolds number when compared to smooth spheres. Using a hot-wire anemometer, they directly measured the streamwise velocity and its fluctuation inside individual dimples located at various angular positions. Based on the measurements, Choi et al. suggested the existence of the local separation bubbles when the flow traverses individual dimples. It is indicated that an unstable shear layer is induced inside the separation bubble, which helps to energize the boundary layer flow and consequently delay the full flow detachment. Moreover, Choi et al. examined the reason why the reduced drag coefficient barely increases as the Reynolds number further increases in the supercritical regime. It is indicated that, with

increasing Reynolds number, the shear layer instability inside the local separation bubble appears at further upstream angular positions, whereas the complete flow separation is nearly fixed at the same angular position.

Due to the challenges of computing the flow past golf balls²¹, the flow behaviors revealed by Choi had not been numerically demonstrated until recently. Smith et al.⁵ investigated the flow over a stationary golf ball at both the subcritical and supercritical Reynolds numbers by conducting direct numerical simulations (DNS) within the framework of an immersed boundary approach. The drag reduction of the golf ball, which occurred at a lower Reynolds number when compared to smooth spheres, was successfully captured in their numerical work, along with a satisfactory agreement of the drag coefficients with the experimental measurements. Moreover, the local separation bubble inside individual dimples proposed by Choi et al.⁴ was numerically demonstrated, and the corresponding small-scale turbulent flow structures were visualized.

More recently, Beratlis et al.¹¹ extended the work of Smith et al.⁵ to the investigation of flow past self-spinning golf balls. They conducted the direct numerical simulations of the rotating golf ball with the same spin parameter at four different Reynolds numbers spanning from the subcritical regime to the supercritical regime. The boundary conditions on the golf ball surface were solved based on the Eulerian grid using an embedded boundary formulation. When the golf ball was rotating, the part of the golf ball surface inside the dimples was considered as a porous surface. The negative Magnus force was obtained in the simulation results for one of the cases in the critical Reynolds number regime. Based on the measurements of the time-averaged tangential velocities on both sides of the golf ball, Beratlis et al. suggested that the flow separation on the side spinning against the main flow was delayed due to its local instability, which directly contributed to the generation of the negative lift force. This conclusion is analogous to the assumption by Bearman and Harvey³. However, although the negative Magnus effect was demonstrated by statistics, no details concerning the development of unsteady forces exerted on the spinning golf ball was provided in the work of Beratlis et al.¹¹.

Chapter 2: Numerical Methods

This chapter presents an overview of the numerical methods adopted in the present study.

2.1 Large-eddy simulation

For the computation of fluid dynamics, it is well known that three primary methods are widely adopted, which are respectively the Reynolds-averaged Navier–Stokes (RANS) method, large-eddy simulation (LES) method and direct numerical simulation (DNS) method.

Usually, RANS method is used for solving a steady flow field since it only provides the average characteristics of the flow field. The effects of the fluctuations on the average flow field are estimated through the modeling of the Reynolds Stresses. These average characteristics are enough for solving many practical engineering problems but, unfortunately, not enough for deeply understanding aerodynamics because unsteady features also play very important roles. However, the RANS method indeed requires much fewer computation resources and simulation time compared with the other two methods.

In contrast, DNS is the most accurate method for a turbulence simulation. It directly solves the Navier-Stokes equations without using any modeling or approximation so that all the motions contained in a flow field can be captured. It is also the simplest method from the conceptual point of view²². However, to conduct DNS usually requires enormous numerical grids because the grid size should be no larger than the smallest scale (Kolmogoroff scale) in order to capture the kinetic energy dissipation²². This makes DNS usually very computationally expensive and sometimes very difficult to conduct especially for cases with complicated wall boundaries. Therefore, DNS method is usually used in solving problems at relatively low Reynolds number and with simple geometry boundaries, such as the tunnel flow.

LES method is considered as a compromise between DNS and RANS in terms of the accuracy and consumption of computation resources. It solves for the large eddies while modeling the small eddies. This is achieved by filtering the governing equations, i.e. eddies that have size larger than the width of the filter, Δ , are considered as the ‘large eddies’, while the ones smaller than Δ are the ‘small eddies’. The concept of LES is also very reasonable from the physical point of view because the large scale motions are much more energetic and effective on the transportation of conserved properties when compared to the small scale

motions ²². A schematic diagram of the different eddies contained in a turbulence flow and the resolved scale respectively in LES and DNS are provided in Fig.2-1²². Actually, the accuracy of LES could be ‘adjusted’, i.e. when higher grid resolution and smaller Δ are used, the solution provided by LES, theoretically, approaches the solution obtained by DNS. However, LES is usually much less costly than DNS ²², which makes it more feasible especially for cases under high Reynolds number condition and/or with complicated geometries. Therefore for the present study, the LES method was adopted.

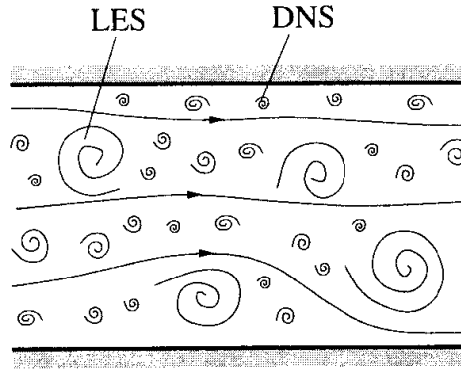


Fig.2-1 Schematic diagram of eddies of different sizes contained in a turbulence flow and the corresponding resolved scale in LES and DNS ²².

2.2 Governing equations of large-eddy simulation

In the present study, the spatially filtered continuity and Navier-Stokes equations for incompressible flow are solved as the governing equations in LES:

$$\frac{\partial \bar{u}_i}{\partial x_i} = 0 \quad (2.1)$$

$$\frac{\partial \bar{u}_i}{\partial t} + \frac{\partial}{\partial x_j} (\bar{u}_i \bar{u}_j) = -\frac{\partial \bar{P}}{\partial x_i} + 2 \frac{\partial}{\partial x_j} (\nu + \nu_{SGS}) \bar{S}_{ij} \quad (2.2)$$

$$\bar{P} = p/\rho + (\overline{u_i u_i} - \bar{u}_i \bar{u}_i)/3 \quad (2.3)$$

where u_i , p , ρ , ν and ν_{SGS} are respectively the i -th velocity component, pressure, density, kinematic viscosity of fluid and the subgrid-scale (SGS) eddy viscosity. The items with overbar represent the spatially filtered quantities. The strain rate tensor S_{ij} is defined as:

$$\bar{S}_{ij} = \frac{1}{2} \left(\frac{\partial \bar{u}_j}{\partial x_i} + \frac{\partial \bar{u}_i}{\partial x_j} \right) \quad (2.4)$$

The most commonly used model of the subgrid-scale eddy viscosity is the standard Smagorinsky model²³, which is:

$$\nu_{SGS} = (C_{SGS}\Delta)^2 \sqrt{2\bar{S}_{ij}\bar{S}_{ij}} \quad (2.5)$$

where C_{SGS} is a model parameter which needs to be determined and Δ is the filter length scale. For the most part, it requires that the C_{SGS} value should be reduced significantly in the vicinity of a solid wall boundary. Therefore the Van Driest damping function²⁴ is usually used to further modify the model of the subgrid-scale eddy viscosity as:

$$\nu_{SGS} = (C_{SGS}f_d\Delta)^2 \sqrt{2\bar{S}_{ij}\bar{S}_{ij}} \quad (2.6)$$

where the damping function f_d is defined as:

$$f_d = 1 - \exp\left(\frac{-y^+}{A^+}\right) \quad (2.7)$$

where y^+ is the dimensionless wall distance and A^+ is a constant.

However, although the standard Smagorinsky model is widely used, it still has some deficiencies. First, the parameter C_{SGS} is not always a constant for different flows. It may be determined based on Reynolds number and/or some other parameters²². In addition, the value of A^+ in the damping function (although usually is considered to be around 25) and even the form of the whole damping function, theoretically, should not be always the same for cases with different boundary layer states. Especially for the flow passing over a golf ball/smooth sphere around the drag crisis region, the transition of the boundary layer from the laminar to turbulent state occurs as the Reynolds number increases from the subcritical to supercritical value. It is very difficult for the standard Smagorinsky model to “adapt” to these changes of the boundary layer.

More recently, a dynamic Smagorinsky model was proposed by Germano et al.²⁵ and further modified by Lilly²⁶. Generally, this model is based on the concept that the smallest

resolved scale is similar to the largest subgrid scale in many ways, and it computes the model parameter at every spatial grid point and every time step directly from the LES results themselves^{25, 26, 22}. Compared with the standard Smagorinsky model, the dynamic Smagorinsky model is able to automatically reduce the model parameter in shear flows and near-wall regions^{25, 22}, which makes it more advantageous to problems with different boundary layer states. Some validations of the dynamic Smagorinsky model for sphere aerodynamics were provided by Constantinescu et al.^{27, 28} and Muto et al.⁹. For these reasons, the dynamic Smagorinsky model was selected for the present study.

2.3 Discretization and numerical schemes

In the present study, the governing equations were discretized based on the vertex-centered finite volume method. This method defines the dependent variables of the discretized governing equations on the vertex of the numerical grids, and a virtual control volume (CV) is generated around the vertex, as illustrated in Fig.2-2. During the simulation, the governing equations were integrated over each control volumes in the whole computation domain.

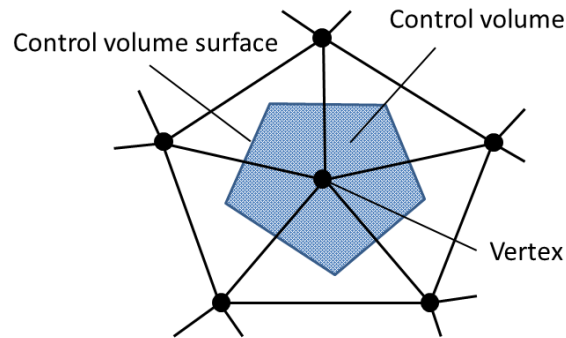


Fig.2-2 Schematic diagram of a two-dimensional vertex-centered control volume.

Using the vertex-centered finite volume method, the governing equations were arranged as the following integral form:

$$\frac{\partial}{\partial t} \int_{\Omega} \rho \Phi d\Omega + \int_S \rho \Phi \mathbf{v} \cdot \mathbf{n} dS = \int_S \Gamma \text{grad} \Phi \cdot \mathbf{n} dS \quad (2.8)$$

where Ω and S respectively represent the volume and the surface of the CV; \mathbf{v} and \mathbf{n} are respectively the velocity vector and the unit normal-wall vector of the CV surface pointing

outwards. Particularly, Φ represents an intensive property of the flow. When $\Phi=1$, eq. (2.8) represents the mass conservation equation; when $\Phi=\mathbf{v}$, eq. (2.8) becomes the momentum conservation equation.

For all the simulations conducted in the present study, the second-order central difference scheme was used for the spatial derivatives with 5% of the first-order upwind scheme being blended for the calculation of the convection term in order to avoid unexpected numerical oscillation. The Simplified Marker and Cell (SMAC) approach²⁹ was adopted for the coupling of the pressure and velocity fields.

For the time advancement, the first-order Euler implicit scheme was adopted. A validation of this scheme for sphere aerodynamics was provided by Muto et al.⁹. According to Muto's estimation, the simulation results obtained in their study showed very limited difference between the first-order Euler scheme and the third-order Adams-Moulton scheme when the maximum Courant number defined in the Courant-Friedrichs-Lewy (CFL) condition was kept to be less than 1.8. In the present study, the maximum Courant number was controlled to be less than 1.1.

According to the CFL condition, the Courant number value in a simulation is proportional to the time increment Δt between each time step and inversely proportional to the length interval determined by the grid resolution. This means that a higher grid resolution (smaller mesh size) and/or a larger Δt will lead to a larger Courant number. In the present study, since the grid resolution in the vicinity of the geometry was very high, especially for the golf ball (details are provided in section 2.5), the time increment was accordingly set to be small enough in order to keep the Courant number less than 1.1. Among all the cases conducted in the present study, the smallest time increment was $\Delta t=4.243 \times 10^{-7}$.

2.4 Arbitrary Lagrangian-Eulerian Method

In the present study, the Arbitrary Lagrangian-Eulerian (ALE) method³⁰ was adopted to impose a self-spinning motion on the golf ball (details are presented in section 2.8). This method allows instantaneously moving vertexes and/or changing the shape and/or size of numerical cells during a simulation.

For the sake of convenience, let us consider both the movement (translation and/or rotation) of the vertex and the change of cell shape as a "deformation" of a numerical grid. This is reasonable because the changes of the volume contained in the original cell at the original position produced by these two ways are qualitatively the same. One way to understand the function of the ALE method is the following³¹: suppose the mesh deformation

produces a mass flux on S , which is estimated by $-\rho \mathbf{u}_d \cdot \mathbf{n} S$, where \mathbf{u}_d is the velocity vector of the deformation of the center of S and \mathbf{n} is the unit normal-wall vector to S . Particularly, \mathbf{u}_d is estimated by the first-order time difference of the distance of deformation (e.g. the moving distance of a vertex) during the time step(s). It should be noted that the minus sign indicates the mass flux being generated in the direction opposite to the deformation.

Taking the mass flux produced by mesh deformation into account, the convection term in eq. (2.2) accordingly becomes:

$$\frac{\partial}{\partial x_j} (\bar{u}_i (\bar{u}_j - u_{d,j})) \quad (2.9)$$

and the corresponding pressure Poisson equation becomes:

$$\frac{\partial^2 \bar{P}}{\partial x_i^2} = \frac{1}{\Delta t} \left[\frac{\partial (\bar{u}_i - u_{d,i})}{\partial x_i} \right] \quad (2.10)$$

As presented in detail in section 2.8, at every new time step, the numerical meshes in the cases of the self-spinning golf ball considered in the present study translated and rotated to a new position determined by the specific rotating motion (no cell shape change exists in the present study), and the meshes at the new position appeared in a key-frame manner. During this process, the moving velocity of each CV was calculated and added into the corresponding convection terms of the governing equations, as shown in eq. (2.9) and (2.10).

2.5 Definition of coordinate system, force direction and force coefficients

The Cartesian coordinate system adopted in the present study for all cases (both the golf ball and smooth sphere) is shown in Fig.2-3. The geometry centers of both models are placed at the position $(x, y, z) = (0, 0, 0)$. The +x, +y, +z directions are respectively defined as the drag force direction, positive side force direction, positive lift force direction (it should be noted that the statements of “side force” and “lift force” are basically nominal for all the stationary cases, which means one can exchange their names without changing the conclusions of the corresponding discussions for the stationary cases. Therefore these two forces are sometimes referred as the “lateral force components” in Chapter 3). The incoming flow approaches from the -x direction, and the “streamwise direction” is accordingly defined as the direction from -x to +x. The angle φ shown in Fig.2-3 is defined as the polar angle on

the x-z plane measured from the front stagnation point of the golf ball/smooth sphere. The “azimuthal direction” considered in the present study is defined on the y-z plane.

For all the self-spinning cases conducted in the present study, a backspin motion rotating about the ‘y’ axis is imposed on the geometries, as indicated in Fig.2-3. The spin parameter Γ is defined as:

$$\Gamma = \frac{\omega \cdot D}{2U} \quad (2.11)$$

where ω represents the angular velocity, D is the diameter of the golf ball/smooth sphere and U is the incoming flow velocity. For all the rotating cases considered in the present study, $\Gamma=0.1$.

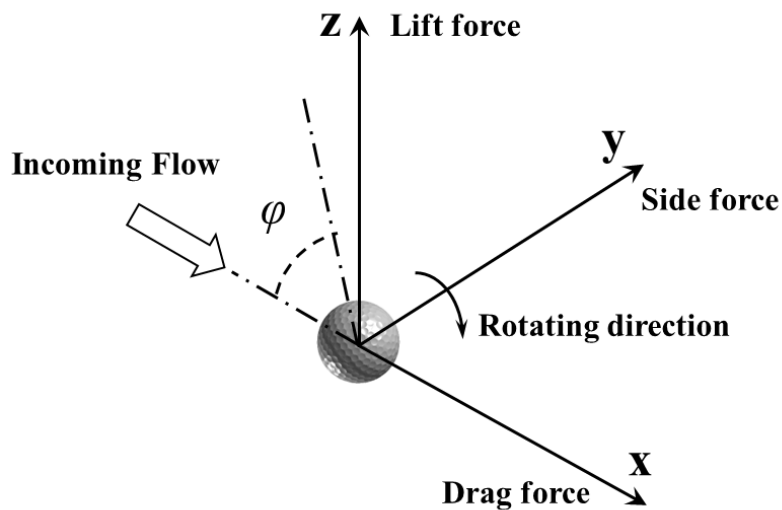


Fig.2-3 Coordinate system and force direction

The drag coefficient C_d , side force coefficient C_s and lift coefficient C_l are respectively defined in the present study as:

$$C_d = \frac{2F_d}{\rho AU^2} \quad (2.12)$$

$$C_s = \frac{2F_s}{\rho AU^2} \quad (2.13)$$

$$C_l = \frac{2F_l}{\rho AU^2} \quad (2.14)$$

where F_d , F_s and F_l respectively represent the drag force, side force and lift force; A represents the projected frontal area of the golf ball/smooth sphere. The pressure coefficient is defined as:

$$C_p = \frac{p}{0.5\rho U^2} \quad (2.15)$$

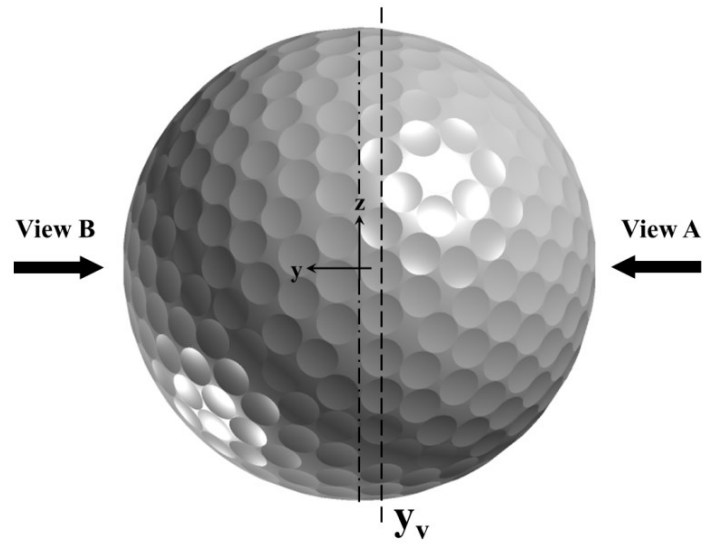
The Reynolds number considered in the present study is defined as:

$$Re = \frac{UD}{\nu} \quad (2.16)$$

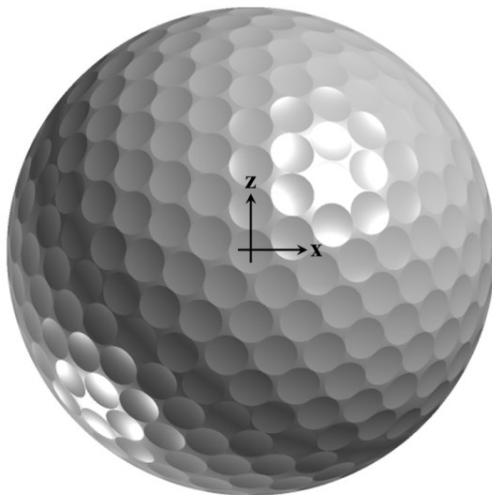
where U is the incoming flow velocity, D is the diameter of the golf ball/smooth sphere, ν is the kinematic viscosity.

2.6 Geometry and mesh generation

The golf ball used in the present study is a real product provided by Sumitomo Rubber Industries, and the corresponding geometry details are displayed in Fig.2-4 from various views. The golf ball consists of two hemispherical parts which share the same design of the dimple patterns. However, these two parts are merged together with an offset angle about 'y' axis. This leads to an asymmetric dimple distribution with respect to the x-z plane, as illustrated in Fig.2-4 (b) and Fig.2-4 (c). 392 uniform-sized spherical dimples are distributed on the golf ball surface. The diameter of the dimple is approximately $9.0 \times 10^{-2} D_g$, where D_g is the diameter of the golf ball. The dimensionless geometry parameter k/D_g , which quantitatively measures the surface roughness of the golf ball, is approximately 0.5×10^{-2} , where k represents the dimple depth. As displayed in Fig.2-4 (a), the path along the central joint line of the golf ball in the section $y=0$ does not go across any dimples on the golf ball surface. The plane y_v shown in Fig.2-4 (a) is located at $y \approx -4.7 \times 10^{-2} D_g$. This plane intersects the center of the row of dimples which stay closest to the central joint line of the golf ball, and is used as the visualization plane for some of the interpretations presented in Chapter 3 and Chapter 4. The smooth sphere used in the present study, for a better comparison, is the same as the one used by Muto et al. ⁹ in their study.

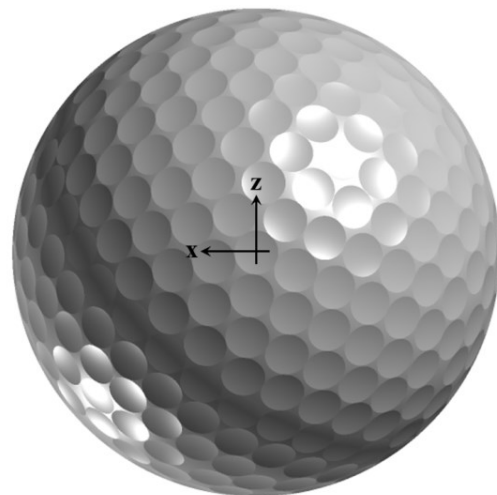


(a)



View A

(b)



View B

(c)

Fig.2-4 Geometry details of the golf ball respectively visualized from the (a) upstream view; (b) negative side force view; (c) positive side force view.

In the present study, an unstructured grid was adopted for the mesh generation of both models. Particularly, triangular elements were generated on the surface of the golf ball/smooth sphere, and prism layers were allocated along the normal-wall direction starting from the surface mesh.

For properly reproducing boundary layer separation and the laminar-turbulent boundary layer transition in the drag crisis region, the numerical grid around the solid wall boundaries must be of sufficient resolution^{5,9}. An estimation of the required grid resolution

for a smooth sphere was provided in Muto's ⁹ study, in which the corresponding grid resolution was determined based on the laminar boundary layer thickness δ_B measured at 90° from the front stagnation point of a sphere, which is estimated as ³²:

$$\delta_B = 3 \times \sqrt{\frac{Dv}{2U}} \quad (2.17)$$

For the smooth sphere used in the present study, by applying the grid resolution same as Muto's ⁹, the size of the surface mesh was set to be equal to δ_B , while the thickness of the first element of the prism layers was set to be about $1/20\delta_B$. It should be noted that δ_B is inversely proportional to Reynolds number, thus the grid resolution was accordingly increased with the Reynolds number.

For the golf ball, however, one should further consider that the numerical grid could properly reproduce the geometry details, such as the dimple shape etc. In the present study, the size of the surface mesh on the dimple edges was set to be about 0.1mm. There are about 40 triangular elements generated across each of the dimples, and about 28 prism layers allocated within the distance of dimple depth k . For both the stationary and rotating golf ball cases, the total cell number amounts to about 145 million. In addition, even comparing with the δ_B estimated based on the highest Reynolds number considered in the golf ball case ($Re=1.7 \times 10^5$) in the present study, the grid resolution of the surface mesh is smaller than $1/2 \delta_B$, and the thickness of the first element of the prism layers is approximately $1/28 \delta_B$. Some details of the numerical grid in the vicinity of the golf ball dimples are displayed in Fig.2-5.

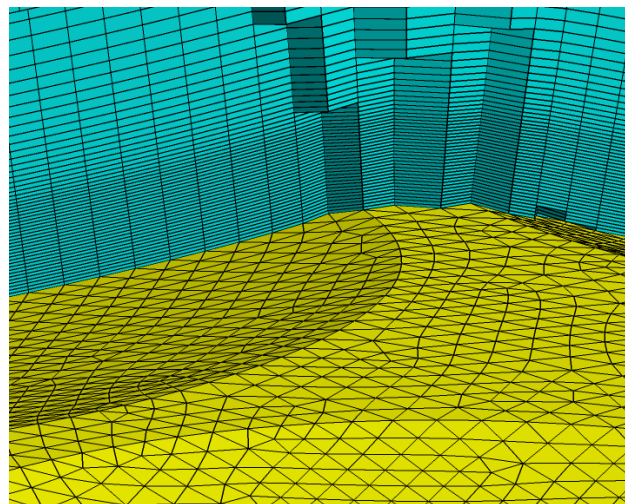


Fig.2-5 Details of the numerical grid in the vicinity of individual dimples

2.7 Computation domains and boundary conditions

In the present study, two different types of computation domains were used for different cases: (1) for the stationary smooth sphere, self-spinning smooth sphere, and stationary golf ball, a domain with the shape of rectangular duct was adopted, as shown in Fig.2-6, and the inertial coordinate system was fixed on the smooth sphere/golf ball; (2) for the self-spinning golf ball, in particular, a spherical computation domain was adopted, as shown in Fig.2-7, and the inertial coordinate system was fixed on the “ground”; This is because the self-spinning motion was imposed on the golf ball in a way different from the smooth sphere. More details about this part are presented in section 2.8. The scope of the rectangular domain was set to be $-13 \leq x/D \leq 13$, $-5.6 \leq y/D \leq 5.6$, and $-5.6 \leq z/D \leq 5.6$. The blockage ratio between the projection area of the geometry and the cross-section of the domain is smaller than 0.63%. The size of the spherical domain was set to be $R_{\text{dom}} = 15.2D_g$, where R_{dom} is the radius of the domain.

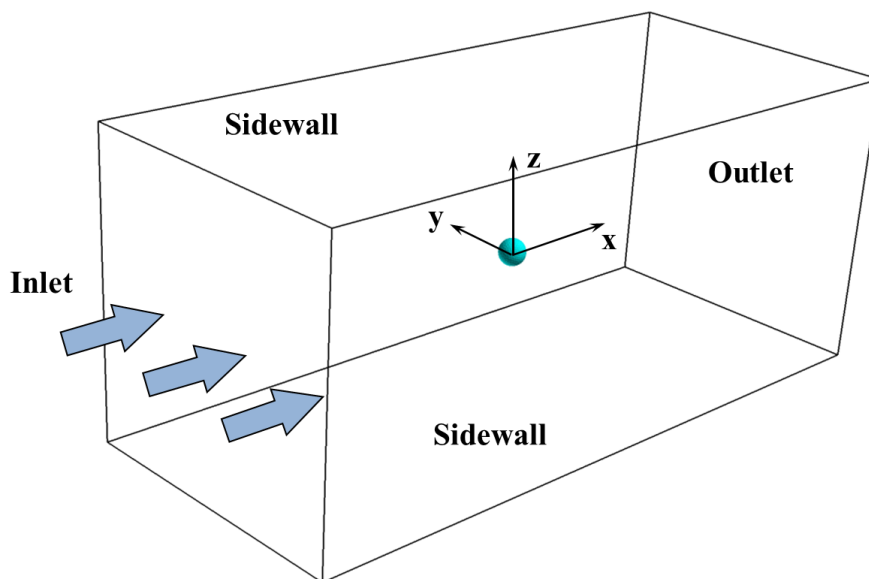


Fig.2-6 Computation domain used for the stationary smooth sphere, self-spinning smooth sphere, and stationary golf ball cases.

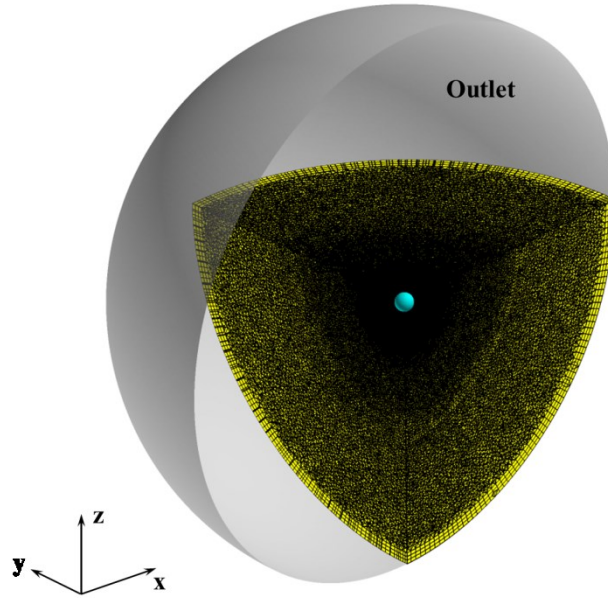


Fig.2-7 Computation domain used for the self-spinning golf ball cases.

On the smooth sphere solid wall boundary, for both the stationary and rotating cases, the no-slip condition was imposed ⁹. On the golf ball solid wall boundary, for both the stationary and rotating cases, the velocity profiles were initially assumed to follow the two-layer law (logarithmic law or linear law depending on y^+ value) because the appropriateness of the grid resolution in the vicinity of the golf ball surface was not clear before running the simulations.

Based on the two-layer law, when $30 < y^+ < 200$, the velocity profile is estimated by the logarithmic law, which is:

$$u^+ = \frac{1}{k^+} \ln y^+ + C^+ \quad (2.18)$$

and also:

$$u^+ = \frac{u}{u_\tau} \quad (2.19)$$

where u^+ is the dimensionless velocity, k^+ is the Karman constant with the value around 0.41, C^+ is an empirical constant which usually takes the value of 5.0~5.5, and u_τ is the friction velocity or shear velocity estimated as:

$$u_\tau = \sqrt{\frac{\tau_w}{\rho}} \quad (2.20)$$

where τ_w is the shear stress. In contrast, when $y^+ < 5$, the velocity profile is estimated by the linear law, which is:

$$u^+ = y^+ \quad (2.21)$$

In the region $5 < y^+ < 30$, which is known as the “buffer layer” area, neither the log law nor the linear law could independently provide a satisfactory estimation of the velocity profile for the whole region. Therefore the velocity profile in this region is usually estimated separately. In the LES code used in the present study (see section 2.9), the logarithmic law is applied when $y^+ \geq 11.63$, while the linear law is applied when $y^+ < 11.63$.

For the golf ball cases, the distance of the first nearest grid point from the solid wall boundary was investigated posteriorly, and it was found that the y^+ value was smaller than 1.0 on almost the whole boundary surface even in the supercritical regime. This indicates that the velocity profiles were estimated by using the linear law function, which corresponds to the no-slip condition. Actually, as shown in Fig.3-10 in Chapter 3, the velocity profile asymptotically becomes zero as the distance from the boundary surface approaches zero.

For all the cases using the rectangular computation domain, a uniform velocity profile of the incoming flow was imposed at the inlet boundary, as illustrated in Fig.2-6. At the outlet boundary, a zero-gradient condition was imposed. For all the sidewall boundaries, a free-slip condition was imposed in order to avoid the forming of unexpected boundary layers. For the spherical computation domain, there is only a single external boundary surface, which was treated as the outlet boundary where a zero-gradient condition was imposed. At the same time, a constant velocity was imposed on the whole computation domain. This is because the ALE method was applied to simulate the self-spinning golf ball, as presented in the following section.

2.8 The reproducing of self-spinning motion

In the present study, the self-spinning motion was imposed on the smooth sphere and golf ball in different ways. For the smooth sphere, which has a homogeneous geometry configuration, the self-spinning motion was imposed by directly adding an angular velocity on the sphere surface as a boundary condition. However, this method is not applicable to a

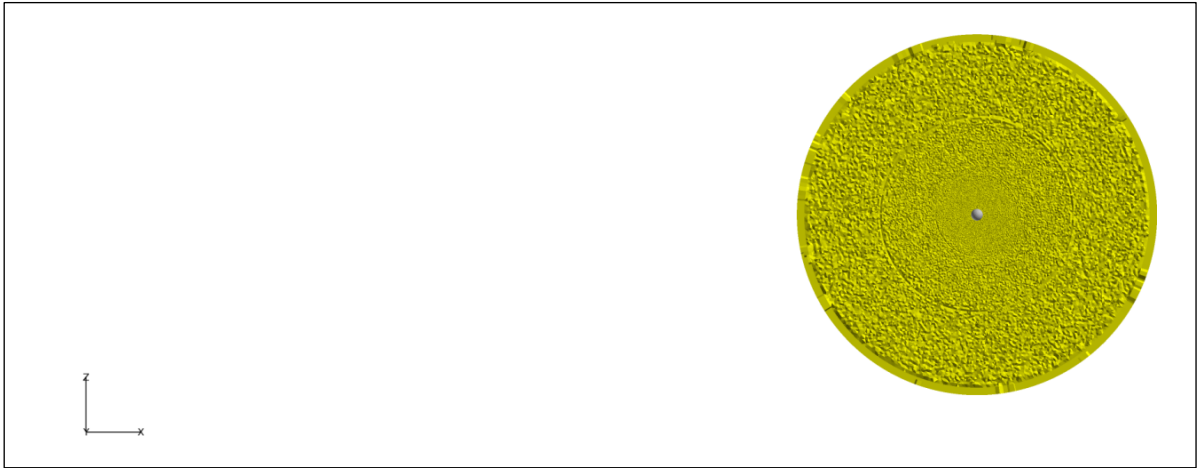
self-spinning golf ball because the configuration of the solid wall boundary with respect to the incoming flow direction continuously changes along with rotation due to the existence of dimples. Therefore, the ALE method (see section 2.4) by which this change of boundary surface configuration could be properly reproduced was applied in the present study.

Using the ALE method, the self-spinning motion was imposed on the entire computation domain without changing its coordinate fixed on the inertial frame of reference (see section 2.7). Meanwhile, a translational velocity was imposed on the entire computational domain, which corresponds to the incoming flow velocity imposed at the inlet boundary of the rectangular domain (see Fig.2-6). At every time step, all the numerical elements and vertices including those on the solid wall boundary moved to a new position (determined by the specific conditions of translation and rotation) computed in the inertial coordinate system fixed on the “ground”. However, this process also results in the position change of the external boundary of the computation domain. Thus an external boundary with a homogenous geometry configuration was needed, and that is why a spherical computation domain was used for the rotating golf ball cases.

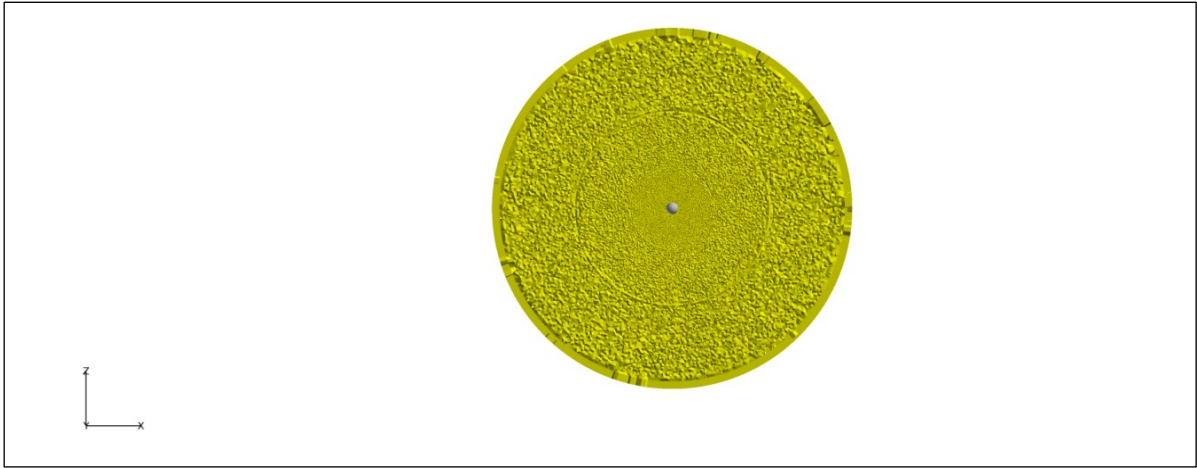
A further illustration of above process is shown in Fig.2-8 and Fig.2-9. As indicated in the figures, during the simulation, the entire computation domain continuously translated from the right to the left with a specific speed, and the golf ball was simultaneously rotating clockwise. This actually means that the process of “a rotating golf ball flying in the air” was simulated.

2.9 Software and hardware

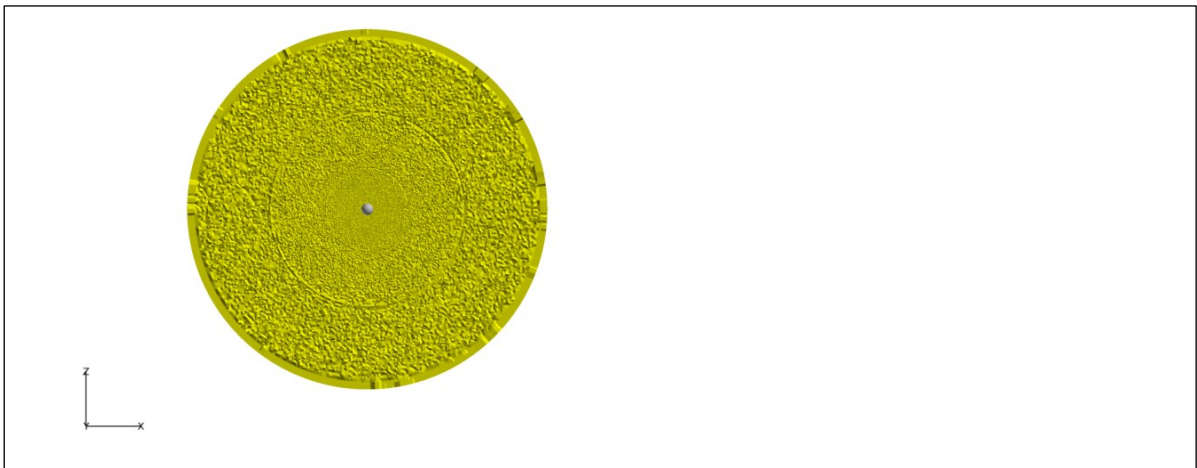
The numerical source code used in the present study is the in-house CFD code “FrontFlow/red” which was originally developed in our research group for the “Frontier Simulation Software for Industrial Science” project³³. Computational resources were provided by following supercomputer systems: HITACHI SR16000 M1 at Hokkaido University; HITACHI HA8000-tc/HT210 at Kyushu University and Dell PowerEdge R620 at Center for Research on Innovative Simulation Software, Institute of Industrial Science, University of Tokyo.



(a) $t=t_1$

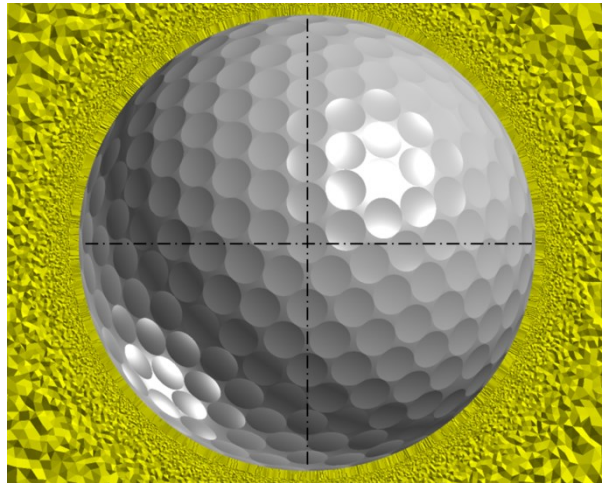


(b) $t=t_2$

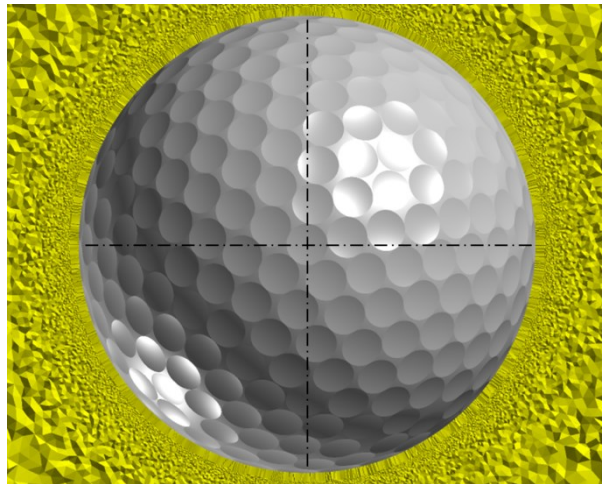


(c) $t=t_3$

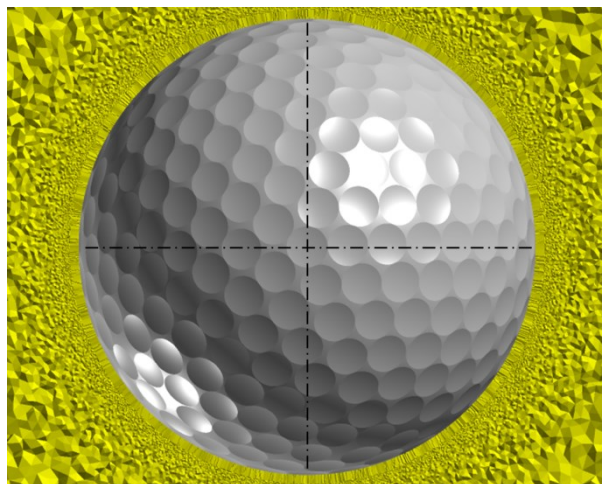
Fig.2-8 Translation of the spherical computation domain with time for the self-spinning golf ball cases; the moving direction is from the right to the left; $t_1 < t_2 < t_3$.



(a) $t=t_1$



(b) $t=t_2$



(c) $t=t_3$

Fig.2-9 Change of the golf ball's angular position at the corresponding time step shown in Fig.2-8; the golf ball is rotating clockwise; $t_1 < t_2 < t_3$.

Chapter 3: Flow past the stationary golf ball and smooth sphere

This chapter presents the investigation of flow past the stationary golf ball and smooth sphere. First, the drag crisis phenomenon of the stationary golf ball is validated. The underlying mechanism of how the dimple roughness lowers the critical Reynolds number range when compared to the smooth sphere is discussed. Finally, the transient features of the aerodynamic forces and wake flow structure is presented.

3.1 Drag crisis of flow past the golf ball

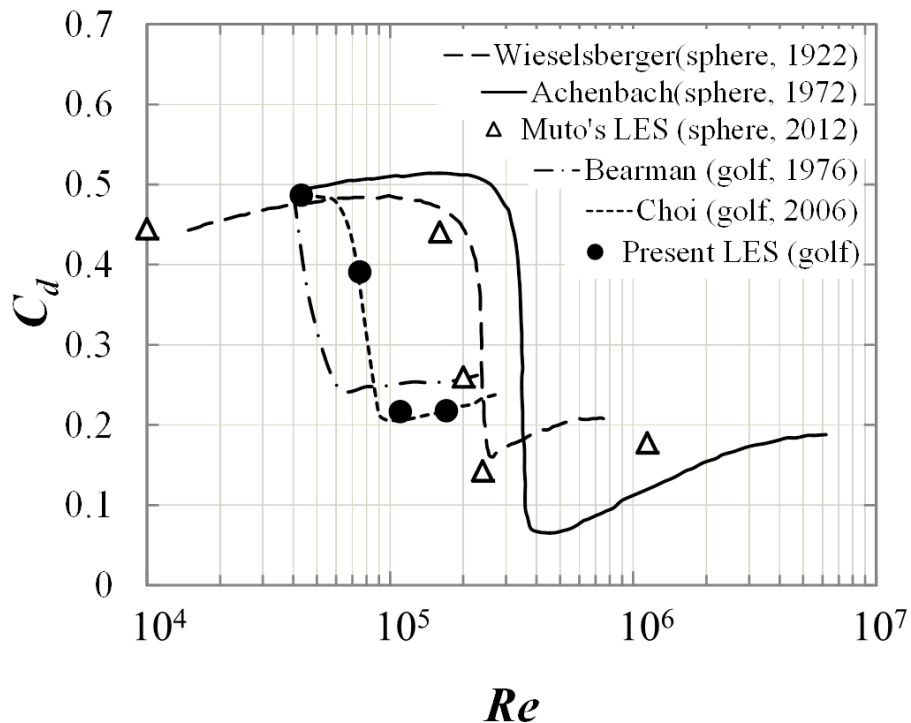


Fig.3-1 Comparison of the drag coefficients for golf balls and smooth spheres; Lines: experimental results; Symbols: numerical results.

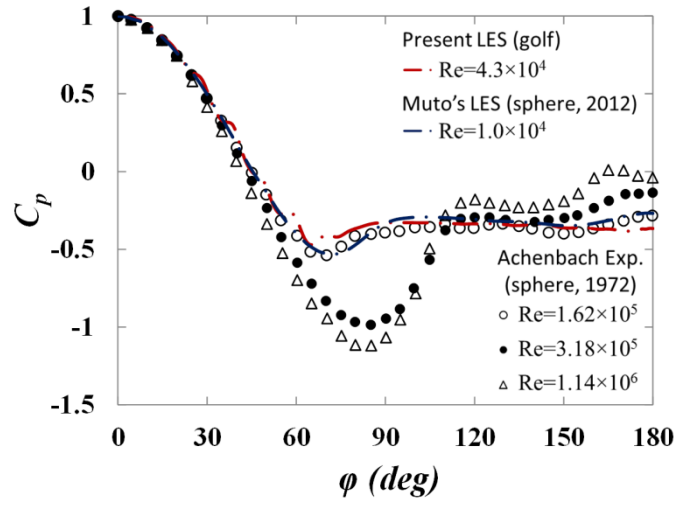
Fig.3-1 shows the drag coefficients of the present golf ball as a function of the Reynolds number. The numerical and experimental results reported in the previous literatures for both golf balls^{3,4} and smooth spheres^{2,9,34} are also included as references. As indicated in this figure, the drag force exerted on the present golf ball shows a considerable decrease as the Reynolds number increases around the critical area. At the subcritical Reynolds number $Re=4.3 \times 10^4$, the drag coefficient of the golf ball stays at around 0.49. This value is comparable to the ones reported in the literatures² for the smooth sphere cases at the same

Reynolds number regime. As the Reynolds number increases to $Re=7.5 \times 10^4$ in the critical regime, the drag coefficient remarkably decreases to around 0.39. When the Reynolds number further reaches to $Re=1.1 \times 10^5$ at the supercritical regime, the drag coefficient correspondingly decreases to around 0.22, which is approximately 55% smaller than the subcritical drag coefficient. However, the drag coefficient is found to stay at an almost constant value at the supercritical regime although the Reynolds number continues to increase to $Re=1.7 \times 10^5$. This trend agrees very well with the experimental measurements by Bearman and Harvey³ and Choi et al.⁴. Moreover, as shown in Fig.3-1, the supercritical drag coefficients of the golf balls are remarkably higher when compared to the smooth spheres. These results coincide with the conclusion by Achenbach obtained for the roughness sphere cases in which the surface roughness was generated using small glass spheres⁶.

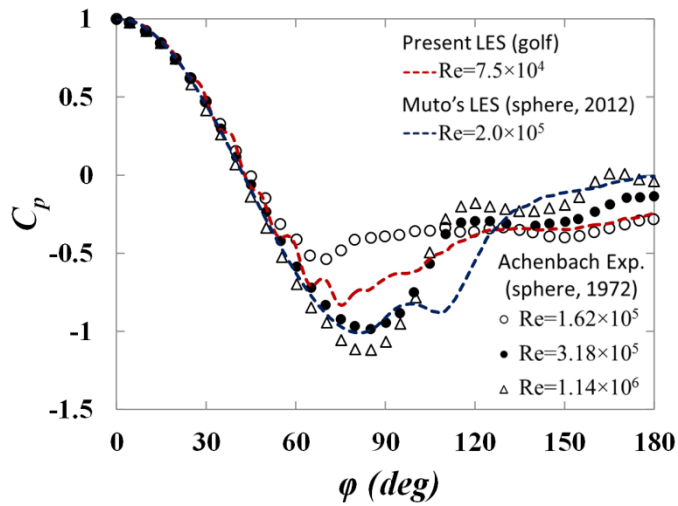
It is also clearly shown in Fig.3-1 that the drag crisis of the present golf ball occurs at a considerably lower Reynolds number than with the smooth spheres. Comparing the present golf ball case at $Re=1.7 \times 10^5$ to the smooth sphere case conducted by Muto et al.⁹ at a similar Reynolds number $Re=1.6 \times 10^5$, the drag coefficient of the golf ball has already decreased to nearly 50% of the drag coefficient of the smooth sphere.

As is also evidenced in the case of the sphere covered with glass roughness⁶, the dimensionless parameter k/D_g is considered as one of the factors that essentially affects the drag crisis of golf balls, especially in terms of the supercritical drag coefficient and the critical Reynolds number range³⁻⁵. Actually, the golf balls which have close k/D_g values are supposed to exhibit similar drag variations during the drag crisis process. Comparing the golf ball used in the present research with the ones used in previous studies, the relative dimple depth of our golf ball ($k/D_g=0.5 \times 10^{-2}$) is very close to that of the golf ball used in Choi's ($k/D_g=0.4 \times 10^{-2}$) study⁴, but remarkably smaller than the value of the golf ball used in Bearman's ($k/D_g=0.9 \times 10^{-2}$) study³. In addition, the present simulation results, as expected, show a very good agreement with Choi's⁴ experimental measurements but an obvious discrepancy from Bearman's³ measurements, as clearly indicated in Fig.3-1. This further demonstrates the good accuracy of the present numerical study.

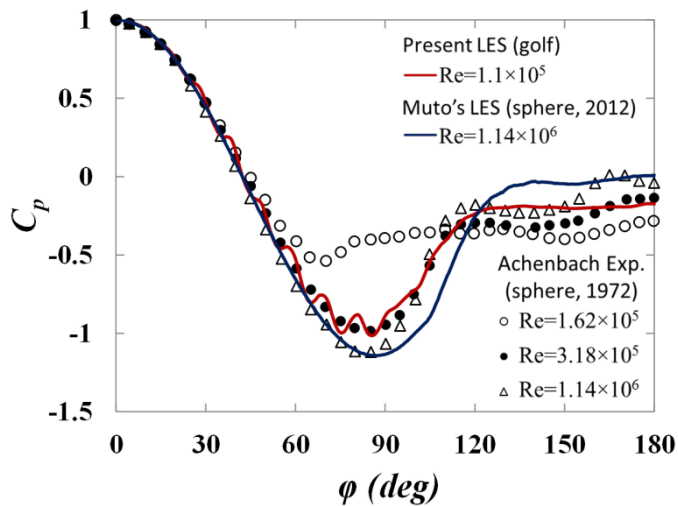
Plotted in Fig.3-2 are the time-averaged surface pressure distributions of the golf ball at different Reynolds number regimes. The time-averaged surface pressure distributions of the smooth spheres obtained at the corresponding regimes are also included as references^{2,9}. Particularly, for all the golf ball cases shown in Fig.3-2, the pressure coefficient C_p is calculated along the central joint line of the golf ball in the section $y=0$ (see Fig.2-4 (a) in Chapter 2). The pressure distribution obtained in the plane y_v will be presented later.



(a)



(b)



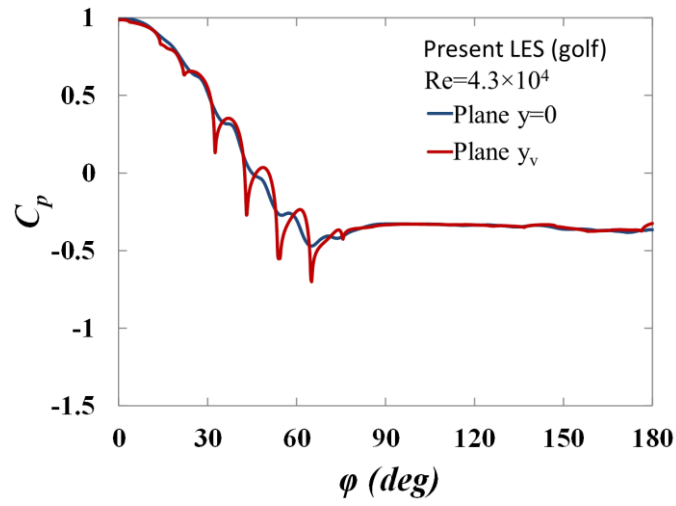
(c)

Fig.3-2 Time-averaged surface pressure distributions on the golf ball (obtained in the section $y=0$; see Fig.2-4 (a) in Chapter 2) and the smooth spheres in the (a) subcritical regime; (b) critical regime; (c) supercritical regime; Lines: numerical simulation results; Symbols: experimental results.

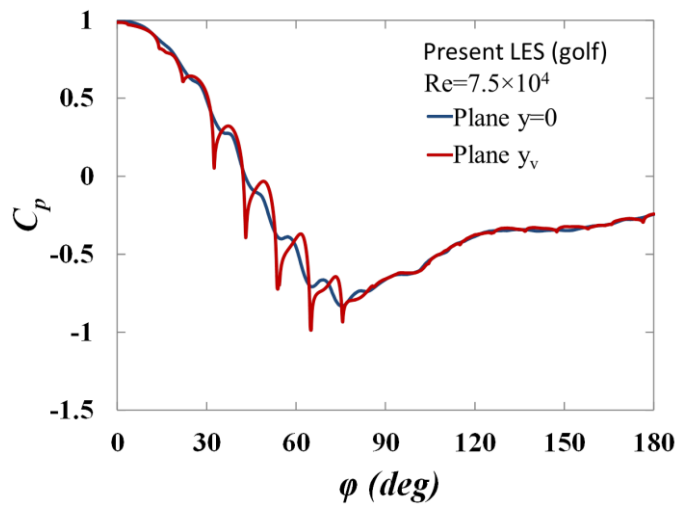
As shown in Fig.3-2 (a), the surface pressure distribution of the golf ball at the subcritical Reynolds number is very similar to the surface pressure distribution of the smooth spheres at the same Reynolds number regime, although the minimum C_p and its angular position are slightly different. This is due to the different positions of the boundary layer separation, as presented in section 3.2. When the Reynolds number goes into the critical range, as shown in Fig.3-2 (b), the surface pressure profiles of both the golf ball and smooth spheres drop rapidly with even a small increase to the Reynolds number. Such a feature of the pressure variation corresponds to the dramatic change of the drag coefficient, as plotted in Fig.3-1, which is attributed to the flow separation moving further downstream. At the supercritical Reynolds number regime, one can clearly observe from Fig.3-2 (c) that the pressure profile of the golf ball at $Re=1.1\times 10^5$ compares well with the pressure distribution of the smooth sphere at $Re=3.18\times 10^5$ obtained by Achenbach's experimental measurement, especially in terms of the minimum C_p and its angular position. This agreement also evidences the similarity of the drag coefficients between these two cases, as indicated in Fig.3-1. Additionally, one can observe that the C_p profiles of the golf ball cases exhibit some local fluctuation at certain angular positions. This is mainly affected by the pressure distribution inside the dimples in the vicinity of the central joint line.

Plotted in Fig.3-3 are the time-averaged surface pressure distributions of the present golf ball obtained respectively in the section $y=0$ and the visualization plane y_v (see Fig.2-4 (a) in Chapter 2) along the same polar angular direction. Since the path in the plane y_v goes across the dimples, several features of the local pressure variation inside the dimples can be identified through the corresponding pressure coefficient profiles.

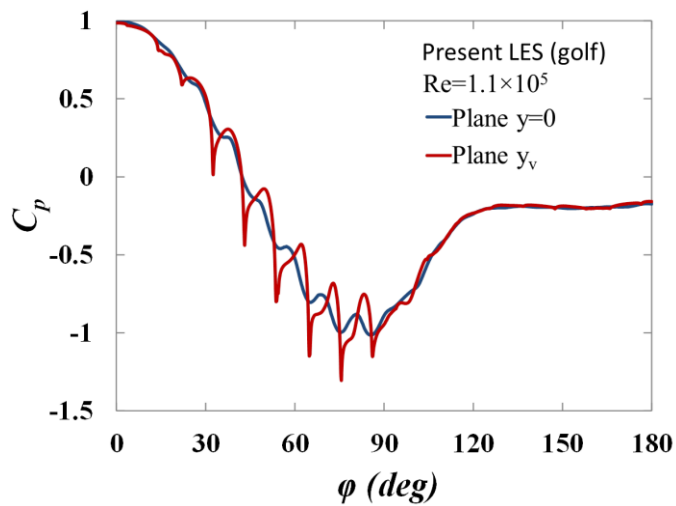
Interestingly, as shown in Fig.3-3, the pressure distribution profiles obtained in the two different planes are found to be almost identical on the golf ball's downwind side surface in each of the three different Reynolds number cases. This partial agreement of the pressure distribution indicates that the effect of the dimples on the flow field is unremarkable on the downwind side regardless of the Reynolds number regime. This phenomenon is probably attributed to the complete boundary layer separation. Actually, the insignificant effect of the dimples after a full detachment of the flow boundary layer was also evidenced by the drag force measurement in Choi's work ⁴. They directly measured the drag coefficients of a full-dimpled sphere and a half-dimpled sphere which had no dimples on the downwind side surface, and found the variations of the drag coefficient for these two models are nearly identical through the whole drag crisis area.



(a)



(b)



(c)

Fig.3-3 Comparison of the time-averaged surface pressure distribution on the golf ball obtained respectively in the plane $y=0$ and plane y_v (see Fig.2-4 (a) in Chapter 2) along the same polar angular direction at the (a) subcritical regime; (b) critical regime; (c) supercritical regime.

However, it is quite noticeable that the pressure distribution on the golf ball's upwind side surface shows a big difference between the profiles obtained in the two planes. At each of the three different Reynolds numbers, the C_p value shows a strong local variation inside the dimples before the boundary layer fully detaches. Generally, the surface pressure exhibits local maximums and minimums as the flow traverses the dimples. However, even inside the same dimple, the profiles show some differences between the cases at different Reynolds numbers. For example, the supercritical pressure coefficient exhibits a more flat profile before it reaches the local maximum peak inside the dimple at around 60° , whereas the subcritical pressure coefficient shows a smoother profile at the same position. Actually, these local changes of the pressure distribution are directly associated with the local flow behaviors inside the dimples which contribute to reducing the drag coefficient of the golf ball at lower Reynolds numbers when compared to the smooth spheres. The detailed discussion about this part is given in section 3.3.

3.2 Flow visualization around the stationary golf ball and smooth sphere

Fig.3-4 displays the instantaneous surface pressure distribution and the non-dimensional streamwise velocity magnitude in the flow field around the separation points of the golf ball and the smooth sphere. The arrows in the figure indicate the angular positions (value of φ) of the flow detachment. The boundary layer separation is identified at the point where the streamwise velocity of the prism layer cell attached on the geometry surface becomes negative.

As indicated in Fig.3-4, for the smooth sphere, the boundary layer separation point shifts downstream from around 87° at the subcritical Reynolds number to around 103° at the supercritical Reynolds number. For the golf ball, however, because of the existence of the dimple roughness, the boundary layer separation point varies more along the azimuthal direction when compared to the smooth sphere. Depending on the specific dimple distributions at different azimuthal positions, the separation point of the golf ball differs from 75° to 85° at the subcritical Reynolds number, and it varies azimuthally from 85° to 95° at the critical Reynolds number, and correspondingly changes between 105° and 110° at the supercritical Reynolds number.

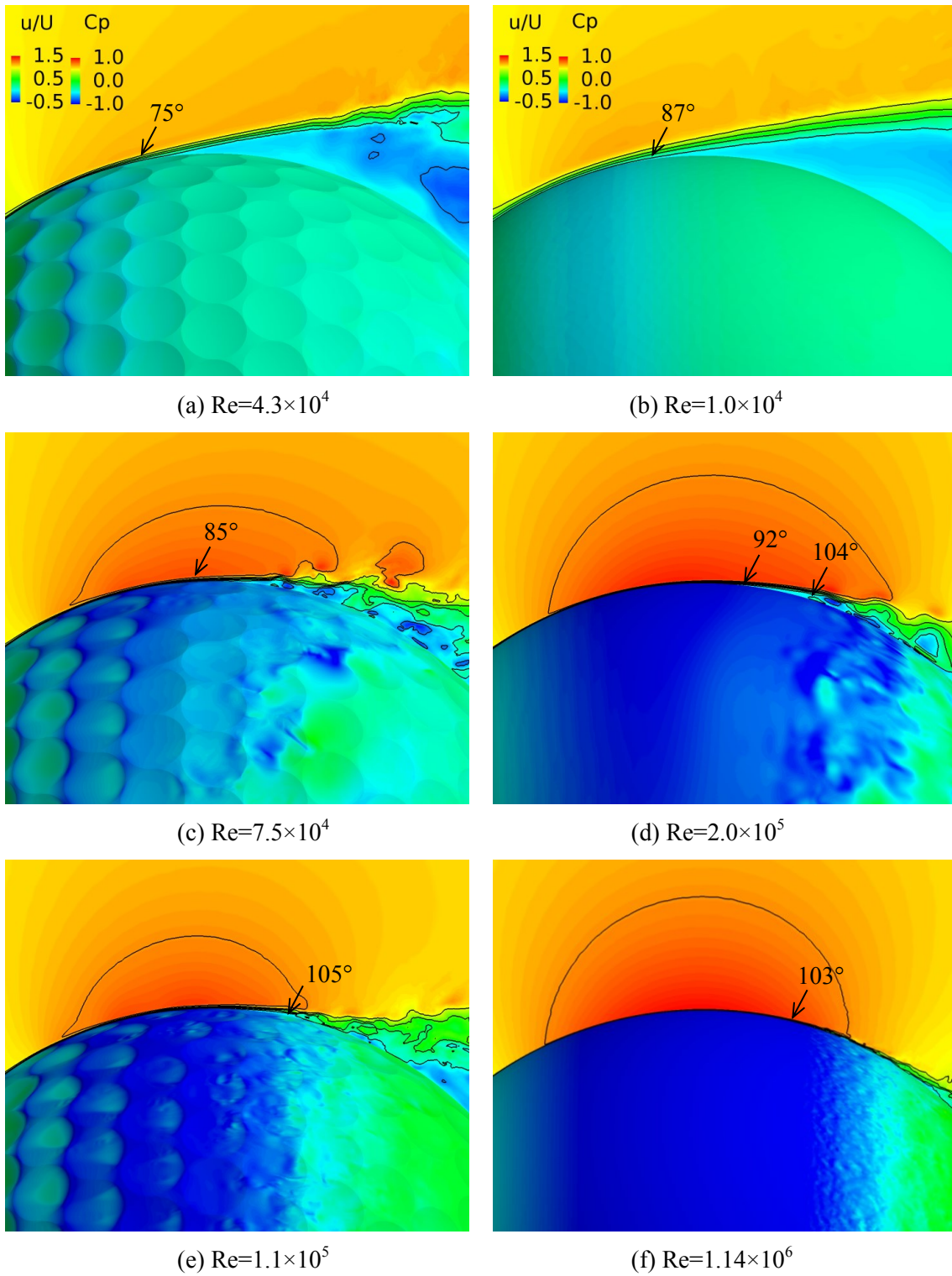


Fig.3-4 Instantaneous surface pressure distribution and contours of the instantaneous non-dimensional streamwise velocity distribution around the separation points of the golf ball and smooth sphere viewed in the plane $y=0$.

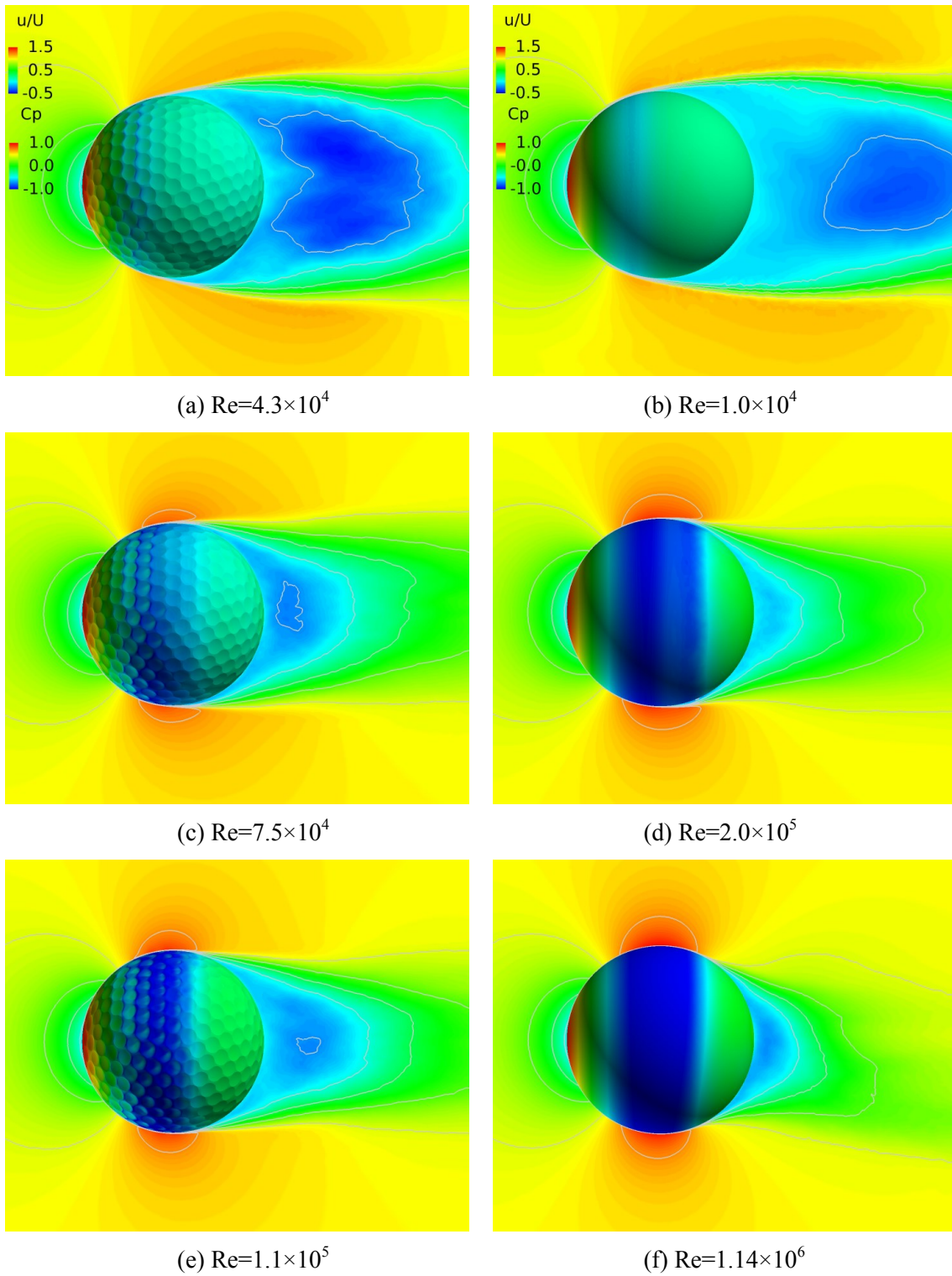


Fig.3-5 Time-averaged surface pressure distribution and time-averaged non-dimensional streamwise velocity distribution in the wake area of the golf ball and smooth sphere viewed in the plane $y=0$.

The shifting of the position of boundary layer separation is strongly affected by the boundary layer transition. As revealed in Fig.3-4, for both the golf ball and the smooth sphere, the boundary layer becomes more turbulent as the Reynolds number increases. The turbulent boundary layer with high momentum could overcome the adverse pressure gradient more, and does not reach full separation until traveling further downstream. It is evident that the dimples lead to the boundary layer transition occurring at a lower Reynolds number when compared to the smooth sphere. The corresponding mechanism is discussed in section 3.3. However, comparing the flow field around the separation point in the subcritical regime, a similarity is observed in the flow behaviors for both the golf ball and the smooth sphere. This suggests the limited effect of the dimples on the laminar boundary layer separation. Additionally, two separation points at different polar angular positions were reported by Muto et al.⁹ for the smooth sphere case at the critical Reynolds number ($Re=2.0\times 10^5$) due to the existence of the global separation bubble. For the golf ball, however, the separation bubbles exist locally inside individual dimples, as presented in section 3.3.

Provided in Fig.3-5 are the time-averaged surface pressure distribution and the corresponding non-dimensional streamwise velocity magnitude in the flow field. It is apparent that, in the subcritical regime, the width of the wake area behind the golf ball stays comparable to the width of the wake area behind the smooth sphere, again indicating the similar flow behaviors between these two cases. As the Reynolds number increases from the subcritical values to the supercritical values, one can clearly observe that the wake regions for both the golf ball and the smooth sphere shrink remarkably as a result of the delay in the complete flow detachment. This shrinkage of the wake area further leads to the decrease of drag coefficient exhibited in the drag crisis phenomenon.

3.3 Mechanism of drag reduction by golf ball dimples

Fig.3-6 depicts the details of the local flow behavior as it traverses the golf ball dimples from 65° to 115° at the supercritical Reynolds number. The time-averaged non-dimensional streamwise velocity obtained in the y_v plane is displayed with the increasing polar angle values. When the flow traverses the dimple located at 70° , as indicated in Fig.3-6, it locally detaches at around 65° while passing the leading edge of the dimple, but reattaches to the geometry boundary again at a position further downstream before exiting this dimple at 75° . A separation bubble consequently forms in the dimple due to the local flow detachment and reattachment. These behaviors repeat again when the flow travels to the next dimple located at 80° . Due to the local reattachment occurring around the trailing edge of the dimple,

the flow stays attached to the golf ball surface from 85° to 95° , and it ultimately reaches complete separation at about 105° . These local separation and reattachment behaviors are also exhibited inside other dimples at different azimuthal positions in the same polar angle range, as depicted by the different colors in Fig.3-6.

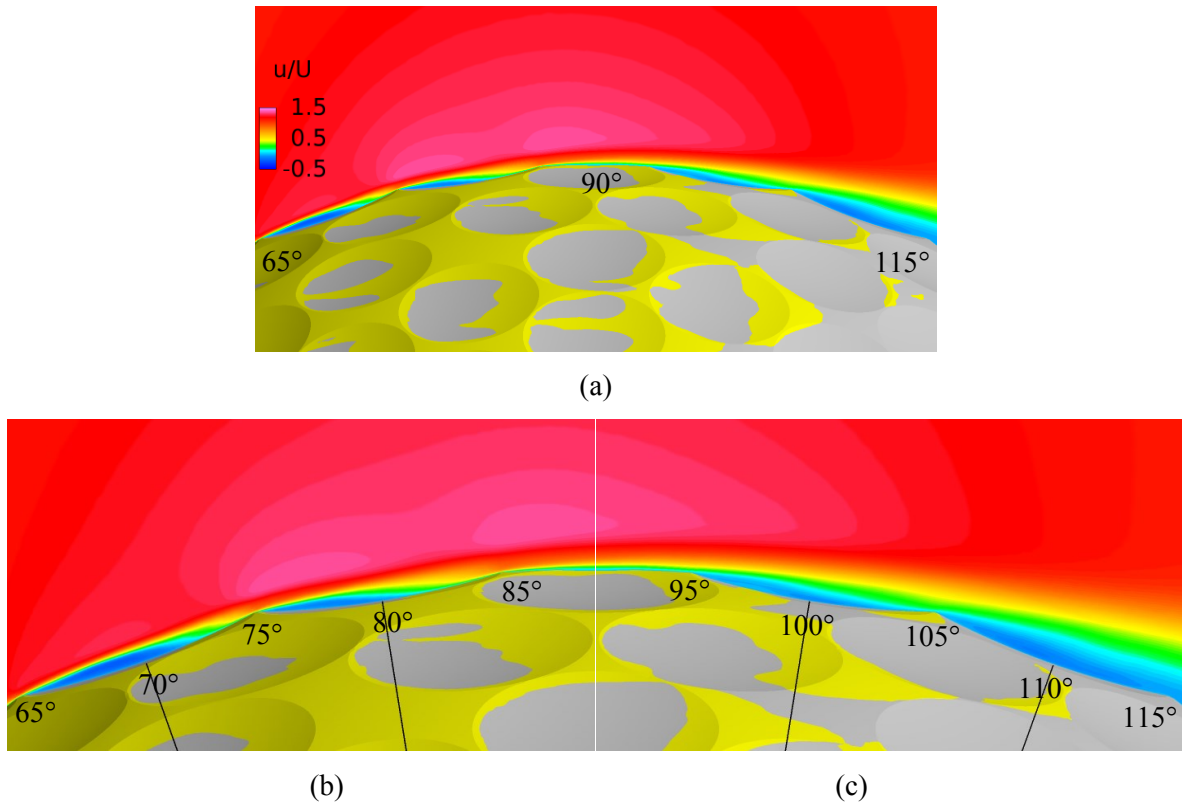


Fig.3-6 Time-averaged non-dimensional streamwise velocity distribution around the golf ball dimples at $Re=1.1 \times 10^5$ viewed on the y_v plane: (a) complete view from 65° to 115° ; (b) detailed view from 65° to 90° ; (c) detailed view from 90° to 115° ; the parts of the golf ball surface colored by ‘yellow’ represent a positive streamwise velocity on the prism layer cell attached on the boundary surface, indicating a flow attachment at corresponding areas; the parts colored by ‘gray’ represent a negative streamwise velocity on the prism layer cell attached on the boundary surface, indicating a flow detachment at corresponding areas.

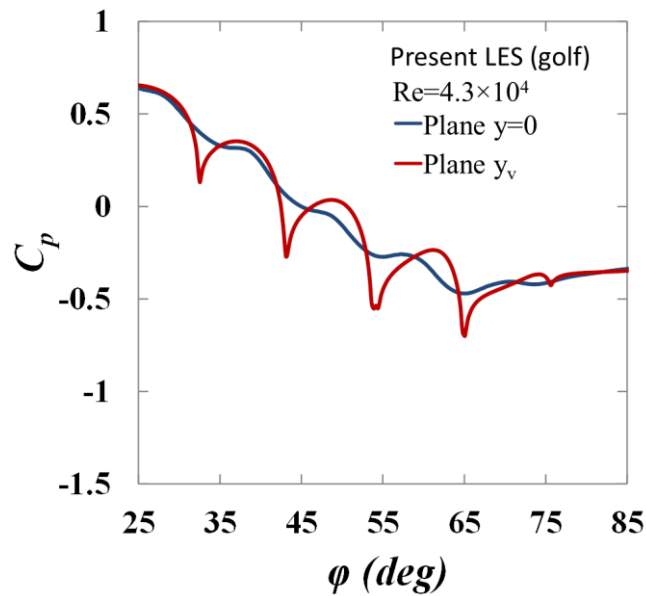
In order to gain deeper insights into the local flow behaviors around the dimples, more details are depicted in Fig.3-7, Fig.3-8 and Fig.3-9. Shown in Fig.3-7 are the corresponding pressure coefficient variations of the subcritical and supercritical cases displayed in Fig.3-3, which are zoomed in the range of polar angle from 25° to 85° . Fig.3-8 and Fig.3-9 indicate the instantaneous velocity vector distributions as the flow respectively

traverses the dimple spanning from 32.5° to 43° and the dimple spanning from 65° to 75° , at both the subcritical and supercritical Reynolds numbers.

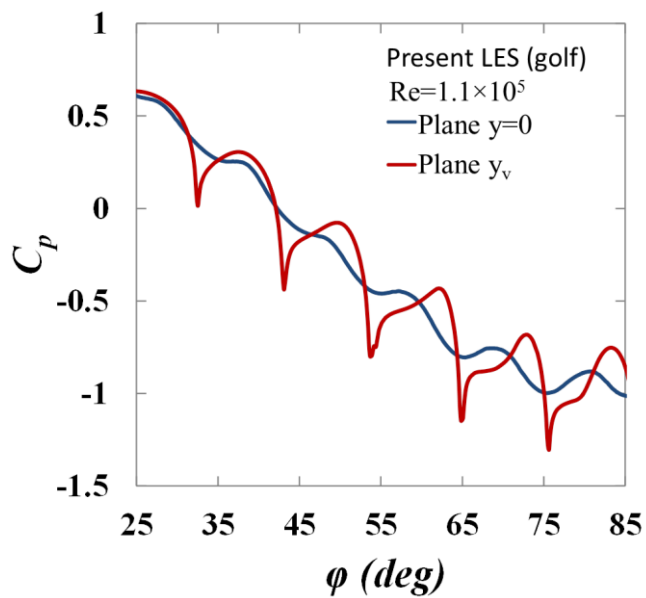
As revealed in Fig.3-8, when the flow passes the dimple spanning from 32.5° to 43° at the subcritical Reynolds number, no separation bubble forms through the whole dimple. Similar behaviors are also exhibited when the flow passes the same dimple at the supercritical Reynolds number, despite a minor local separation in the very front area of the dimple. It can thus be concluded that the forming of a local separation bubble does not immediately occur when the flow traverses the dimples located at a polar angular position considerable upstream. Comparing the surface pressure distributions shown in Fig.3-7, one can clearly observe that the patterns of the C_p curves inside the dimple spanning from 32.5° to 43° are very similar between the subcritical case and the supercritical case, although the C_p values are different due to the different Reynolds numbers. This similarity corresponds to the analogous non-separated flow behaviors between these two cases. The local increase and local decrease of the C_p values are most likely attributed to the variation of velocity due to the change of geometry pattern and the Coandă effect when the flow passes the dimple.

When the flow traverses the dimple located at 70° , however, the flow behaviors show a considerable discrepancy between the subcritical case and the supercritical case, although the local separation bubbles form in both cases, as revealed in Fig.3-9. One can clearly observe that, at the supercritical Reynolds number ($Re=1.1\times 10^5$), the flow locally separates on the leading edge when it passes the dimple, and the detached shear layer quickly becomes unstable and oscillates considerably as it travels further downstream. Meanwhile, small-scale vortices are generated inside the dimple. As a result of the shear layer instability, the momentum in the near-wall flow is increased. With the increased momentum, the reattached flow is able to overcome the adverse pressure gradient more and travel further downstream, which consequently delays the complete flow separation. It is this mechanism that leads to the drag crisis of golf balls occurring at a lower Reynolds number when compared to smooth spheres. However, at the subcritical Reynolds number ($Re=4.3\times 10^4$), the shear layer developed following the local separation does not become greatly unstable, thus the momentum in the near-wall flow is not sufficient enough to overcome the adverse pressure gradient as the reattached flow travels further downstream. Therefore, although a separation bubble forms due to the local flow separation and reattachment, the complete flow separation is not delayed in the subcritical regime. The discrepancies between the subcritical case and the supercritical case are also revealed by the surface pressure variation depicted in Fig.3-7. Different to the situation inside the dimple spanning from 32.5° to 43° , the local maximum C_p

values observed in these two cases between the polar angle of 65° and 75° correspond to the local flow reattachment. As clearly shown in Fig.3-7, the C_p value for the supercritical Reynolds number drops quickly around 75° as the reattached flow continues traveling further downstream, whereas the C_p value for the subcritical Reynolds number does not further decrease due to the complete flow separation.

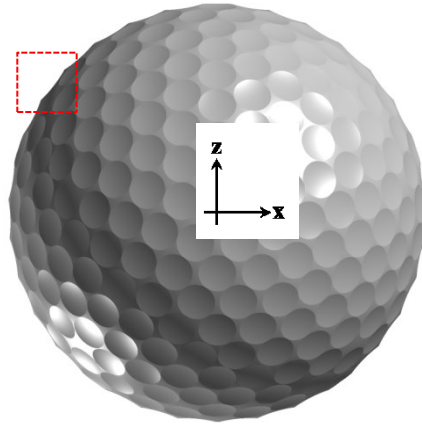


(a)

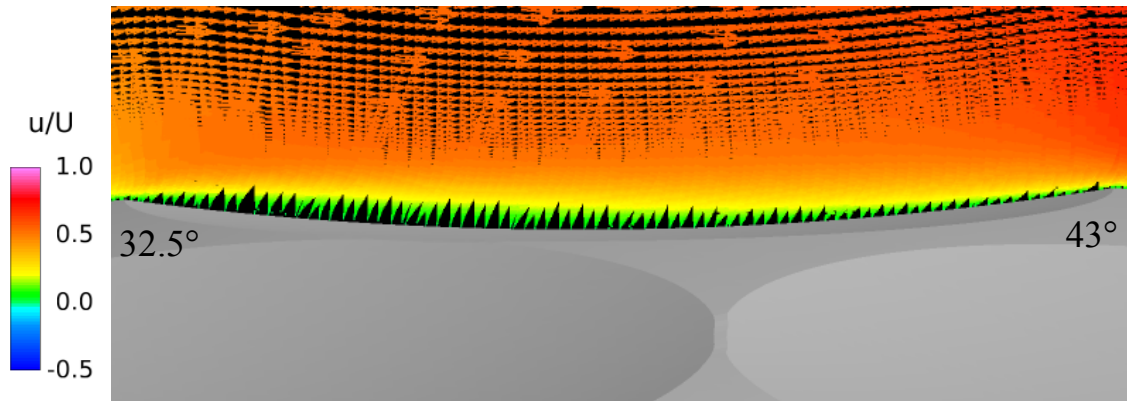


(b)

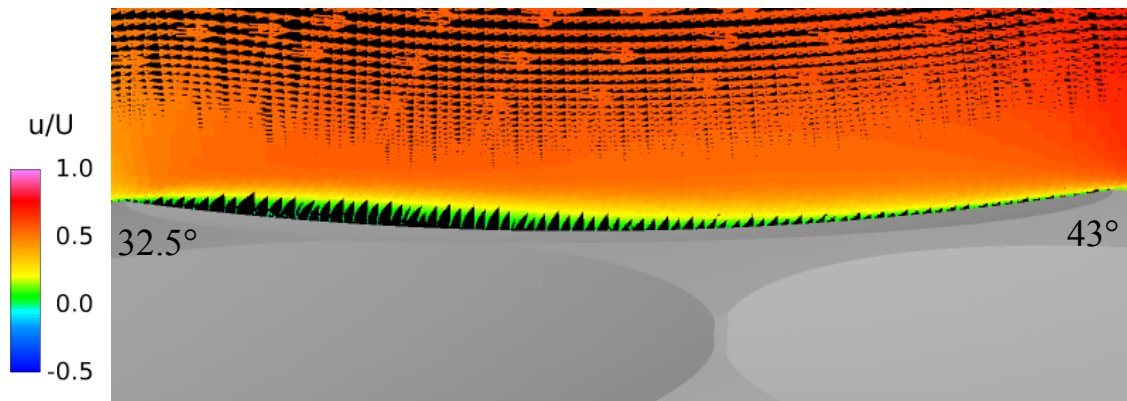
Fig.3-7 Time-averaged surface pressure distribution on the golf ball obtained respectively in the plane $y=0$ and plane y_v (see Fig.2-4 (a) in Chapter 2) along the same polar angular direction from 25° to 85° ; (a) $Re=4.3 \times 10^4$; subcritical regime; (b) $Re=1.1 \times 10^5$; supercritical regime.



(a)

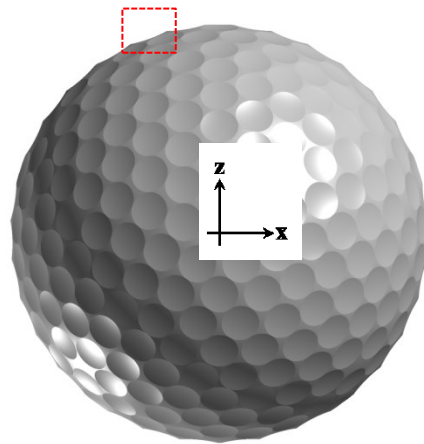


(b)

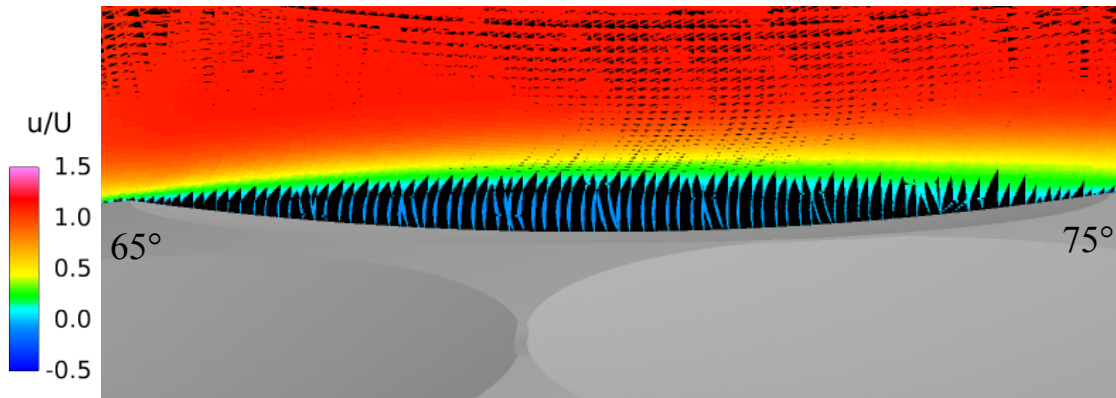


(c)

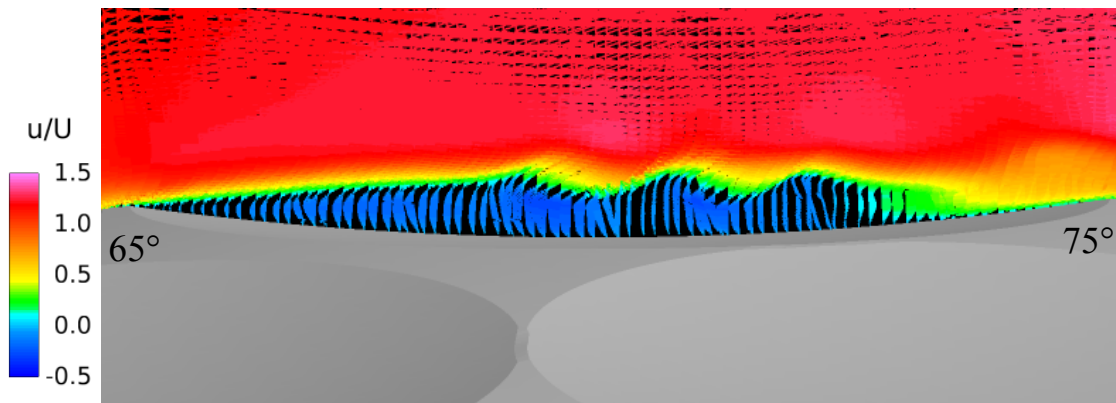
Fig.3-8 The distribution of the instantaneous velocity vectors inside the dimple spanning from 32.5° to 43° ; the incoming flow moves from the left to right; (a) Indication of position of the dimple spanning from 32.5° to 43° ; (b) $Re=4.3 \times 10^4$; subcritical regime; (c) $Re=1.1 \times 10^5$; supercritical regime.



(a)

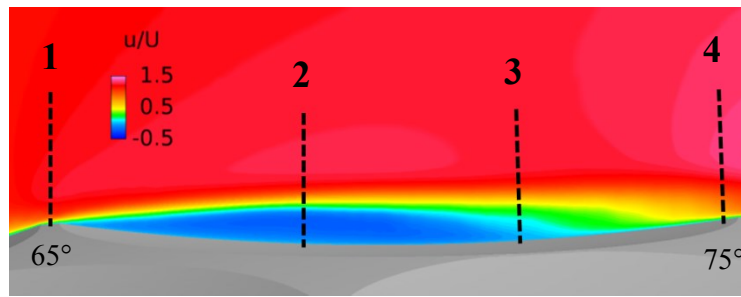


(b)

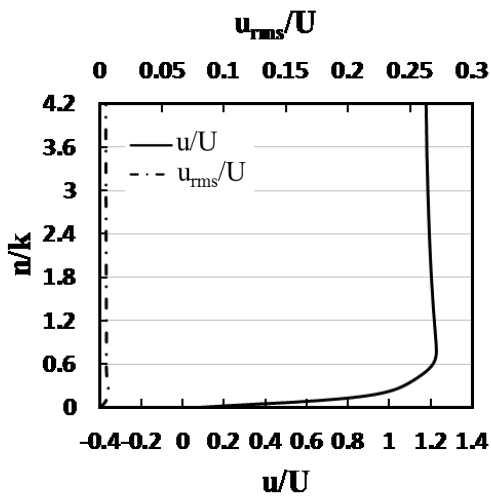


(c)

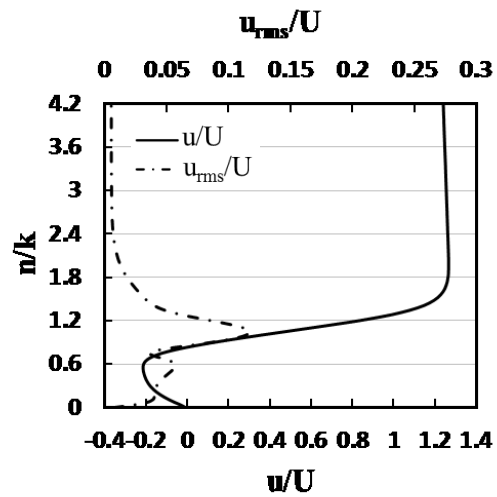
Fig.3-9 The distribution of the instantaneous velocity vectors inside the dimple spanning from 65° to 75°; the incoming flow moves from the left to right; (a) Indication of position of the dimple spanning from 65° to 75°; (b) $Re=4.3 \times 10^4$; subcritical regime; (c) $Re=1.1 \times 10^5$; supercritical regime.



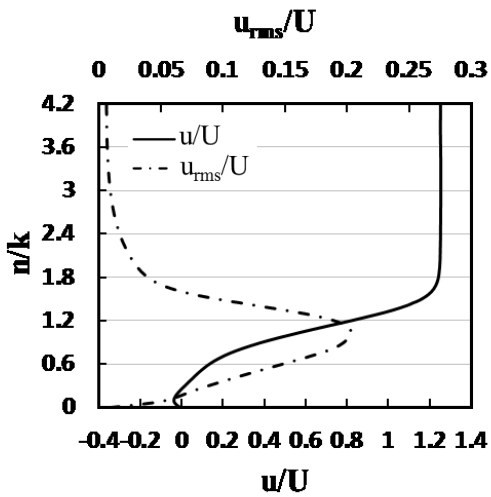
(a)



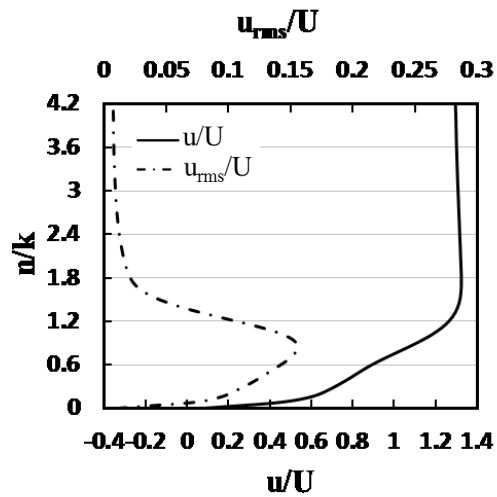
(b)



(c)



(d)

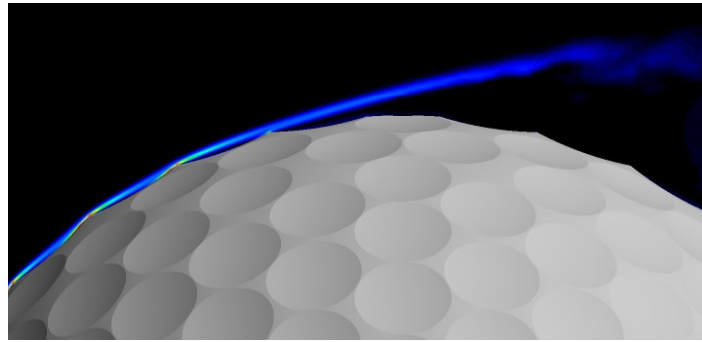


(e)

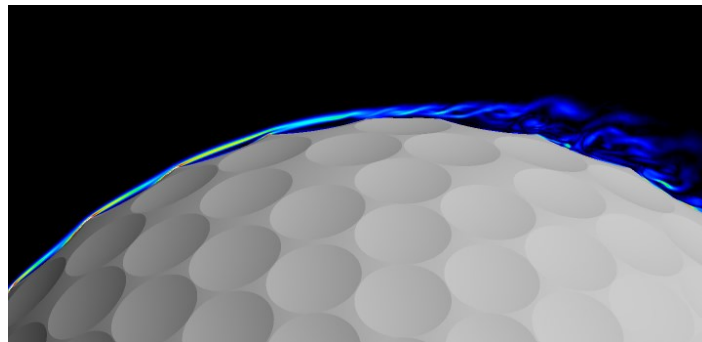
Fig.3-10 Profiles of the time-averaged streamwise velocity and the r.m.s fluctuation of the streamwise velocity measured above the dimple spanning from 65° to 75° at $Re=1.1 \times 10^5$: (a) position 1-4 for profile plotting; (b) profiles obtained at position 1; (c) profiles obtained at position 2; (d) profiles obtained at position 3; (e) profiles obtained at position 4.

A quantitative clarification of the momentum transfer inside the dimples at $Re=1.1\times 10^5$ is plotted in Fig.3-10. The time-averaged streamwise velocity and its root-mean-square fluctuation were measured at the four specific positions inside the dimple located at 70° along the normal-wall direction, as shown in Fig.3-10 (a). A dimensionless normal-wall axis is used for displaying the profile, in which the variable n represents the normal-wall distance away from the geometry surface and k is the dimple depth. As illustrated in the figure, the flow stays attached while passing the leading edge of the dimple at position 1, and the flow velocity barely fluctuates. At position 2, the velocity profile is reversed in a small area close to the boundary surface due to the local flow separation, and the velocity fluctuation significantly increases along the separated shear layer. Owing to the momentum transfer caused by the velocity fluctuation, the flow subsequently reattaches to the boundary surface, and a separation bubble forms around position 3. The reattached flow with high momentum in the near-wall region further travels to position 4 and exits the dimple without any other local detachment. This process and the profiles also qualitatively agree well with the measurements by Choi et al. ⁴ and Smith et al. ⁵.

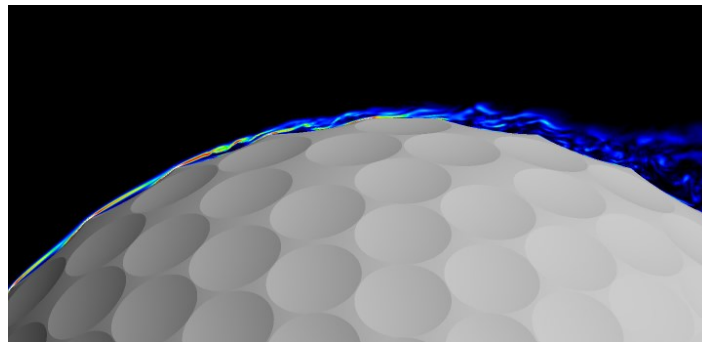
More interpretation of the flow near the dimples is provided in Fig.3-11 by the visualization of the instantaneous azimuthal vorticity which is perpendicular to the visualization plane y_v in different Reynolds number regimes. At the subcritical Reynolds number ($Re=4.3\times 10^4$), the shear layer developed after the full flow separation shows little instability until it travels some distance downstream from the separation point. At the critical Reynolds number ($Re=7.5\times 10^4$), the flow around the golf ball starts to become unstable as it exits the dimple close to the location of the full separation. As the Reynolds number goes into the supercritical regime ($Re=1.1\times 10^5$), the flow experiences some local instabilities inside the dimples before reaching full separation at positions further downstream. As the Reynolds number increases further in the supercritical regime ($Re=1.7\times 10^5$), the position where the flow starts to exhibit local instabilities inside the dimples moves further upstream, whereas the location of the full flow separation does not change remarkably, resulting in little shifting of the drag coefficient. These results agree very well with Choi's ⁴ experimental measurements.



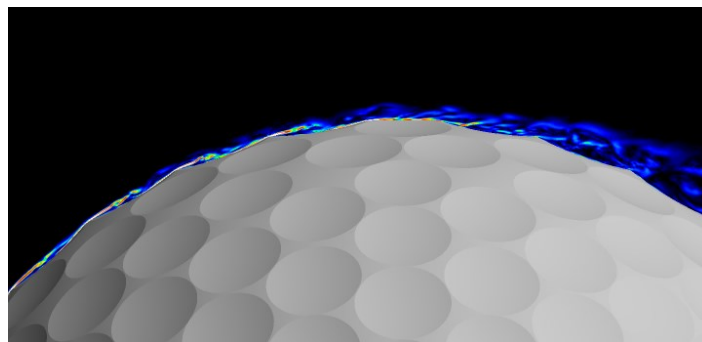
(a)



(b)



(c)



(d)

Fig.3-11 Contours of the instantaneous azimuthal vorticity viewed on the y_v plane at different Reynolds numbers; the vorticity direction is out-of-plane; (a) $Re=4.3 \times 10^4$, subcritical; (b) $Re=7.5 \times 10^4$, critical; (c) $Re=1.1 \times 10^5$, supercritical; (d) $Re=1.7 \times 10^5$, supercritical.

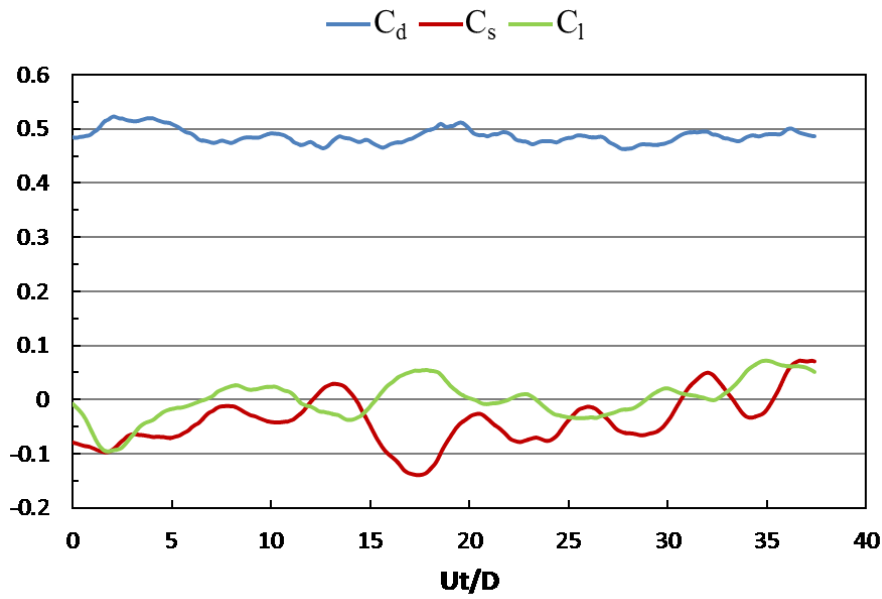
3.4 Development of the unsteady aerodynamic forces and wake flow structure

Table.3-1 Summary of the time-averaged mean value and standard deviation (s.d.) of the side force coefficient C_s and lift force coefficient C_l for the stationary golf ball and smooth sphere at the subcritical, critical and supercritical Reynolds numbers.

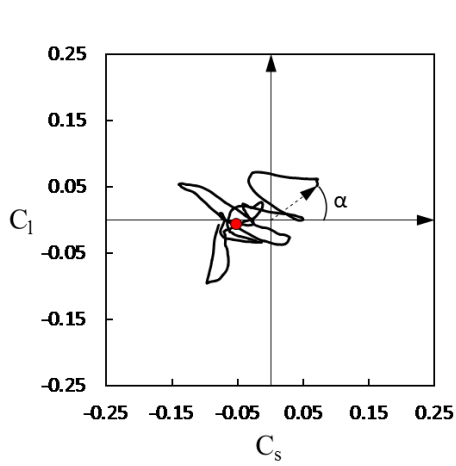
		Golf Ball			Smooth Sphere		
		Re= 4.3×10^4	Re= 7.5×10^4	Re= 1.1×10^5	Re= 1.0×10^4	Re= 2.0×10^5	Re= 1.14×10^6
		(subcritical)	(critical)	(supercritical)	(subcritical)	(critical)	(supercritical)
C_s	mean	-0.0392	0.0100	0.0460	-0.0222	0.0039	-0.0044
	s.d.	0.0461	0.0965	0.0399	0.0300	0.0601	0.0952
C_l	mean	0.0006	-0.0341	-0.0287	-0.0190	0.0137	-0.1425
	s.d.	0.0365	0.0643	0.0451	0.0292	0.0436	0.0549

3.4.1 Transient lateral force and wake flow structure in the subcritical regime

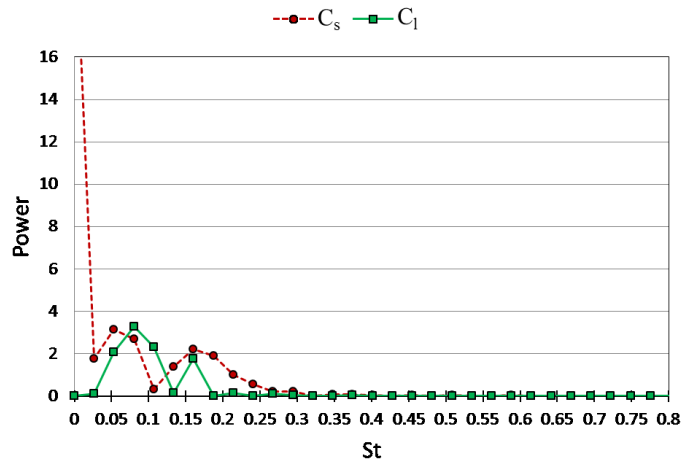
Time histories of the drag and lateral forces acting on the stationary golf ball at $Re=4.3 \times 10^4$ are provided in Fig.3-12. The corresponding force evolution of the stationary smooth sphere at $Re=1.0 \times 10^4$ is shown in Fig.3-13. For a better comparison, the non-dimensional time scale Ut/D is used, where U is the incoming flow velocity, t is the physical time and D is the diameter of the golf ball or smooth sphere. For all the time history data displayed in this dissertation, $Ut/D=0$ indicates a moment when the flow has reached a statistically steady state and a stable drag coefficient C_d . Such a process required calculations for at least tens of D/U time units¹⁵ from the initial conditions depending on different Reynolds numbers. The phase diagram shown in Fig.3-12 (b)/Fig.3-13 (b) illustrates the evolution of the resultant lateral force within the same time interval shown in Fig.3-12 (a)/Fig.3-13 (a). As mentioned before, the side force (C_s) direction denotes the y-axis direction whereas the lift force (C_l) direction denotes the z-axis direction. The distance between the origin in the phase diagram ($C_s=0, C_l=0$) and a point on the curve (e.g. the length of the vector shown in Fig.3-12 (b)) represents the magnitude of the resultant lateral force coefficient (calculated by $\sqrt{C_s^2 + C_l^2}$) at a specific moment. The angle α shown in Fig.3-12 (b) indicates an instantaneous direction of the total lateral force looking from the downstream view of the geometries. Table.3-1 summarizes the time-averaged values and the standard deviations of the side and lift force coefficients for the golf ball and smooth sphere in various Reynolds number regimes.



(a)

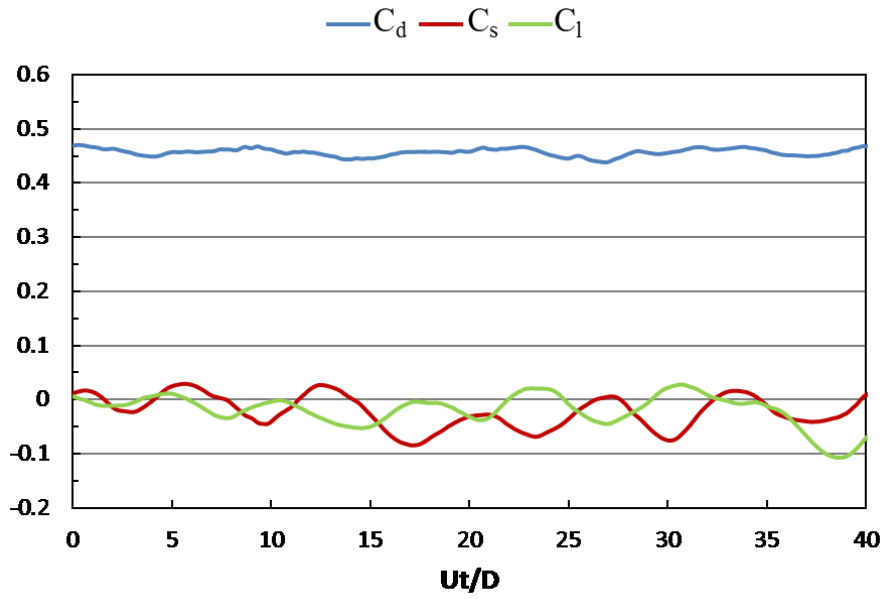


(b)

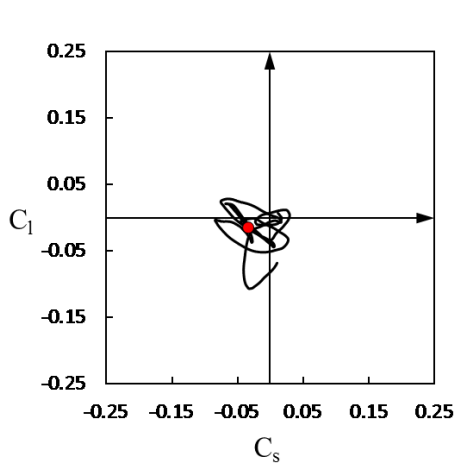


(c)

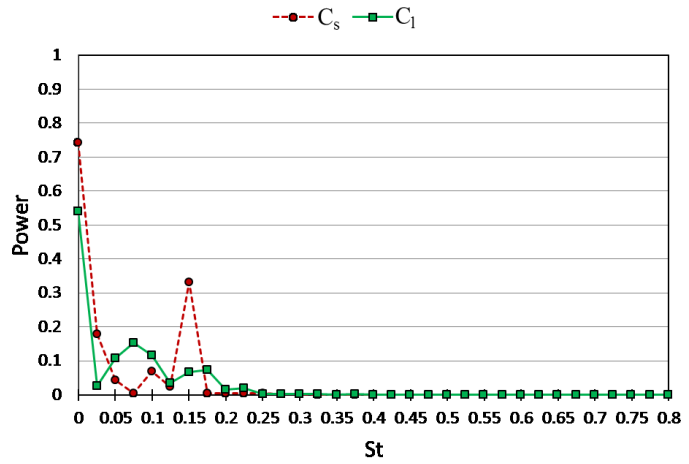
Fig.3-12 Time series of the drag and lateral force coefficients for the stationary golf ball at subcritical $Re=4.3 \times 10^4$ after the flow reached a statistically steady state: (a) temporal evolution of the drag coefficient C_d , side force coefficient C_s and lift coefficient C_l ; (b) phase diagram of C_s and C_l , the red point represents the resultant lateral force at the non-dimensional moment indicated in Fig.3-14; the angle α indicates the instantaneous direction of the resultant lateral force looking from the downstream view of the geometry; (c) power spectrum of the side force coefficient C_s and lift coefficient C_l .



(a)



(b)



(c)

Fig.3-13 Time series of the drag and lateral force coefficients for the stationary smooth sphere at subcritical $Re=1.0 \times 10^4$ after the flow reached a statistically steady state: (a) temporal evolution of the drag coefficient C_d , side force coefficient C_s and lift coefficient C_l ; (b) phase diagram of C_s and C_l , the red point represents the resultant lateral force at the non-dimensional moment indicated in Fig.3-15; (c) power spectrum of the side force coefficient C_s and lift coefficient C_l .

As revealed in Fig.3-12, both the magnitude and the direction of the resultant lateral force vary irregularly with time for the subcritical golf ball case at $Re=4.3 \times 10^4$. Similar features are also evident in Fig.3-13 for the subcritical smooth sphere case at $Re=1.0 \times 10^4$, which agrees very well with the conclusions by Constantinescu et al.¹⁵ and Yun et al.¹⁶

regarding the flow over smooth spheres at the same Reynolds number. For both the golf ball and smooth sphere, the mean values of the lateral force components are close to zero over an adequately long time interval. However, as listed in Table.3-1, the standard deviations of both the side and lift forces acting on the golf ball are slightly larger when compared to the smooth sphere. In addition, one can observe from Fig.3-12 (b) and Fig.3-13 (b) that the curve in the phase diagram representing the golf ball is somewhat less concentrated around the origin. These features indicate that the magnitude and oscillation of the lateral force acting on the golf ball are slightly larger than those of the smooth sphere. This is probably associated with the greater shifting of the flow separation point along the azimuthal direction for the golf ball at the subcritical Reynolds number, as discussed in section 3.2.

Respectively shown in Fig.3-12 (c) and Fig.3-13 (c) are the power spectra of the side force and lift coefficients for the stationary golf ball and smooth sphere in the subcritical regime, where St represents the Strouhal number. As clearly displayed in Fig.3-13 (c), two dominant frequencies exist for the lateral forces acting on the smooth sphere, which agrees very well with the previous conclusions^{15, 16}. It is considered that the higher dominant frequency (around $St=0.15$) corresponds to the large-scale wake instability, whereas the presence of the peak at the lower frequency (around $St=0.075$) is due to a modulation in time^{15, 16}. Interestingly, similar features are also distinct in the subcritical golf ball case. As clearly shown in Fig.3-12 (c), two dominant frequencies appear in the power spectra of the lateral forces acting on the golf ball, and the higher one (around $St=0.16$) which is associated with the large-scale wake instability stays very close to the corresponding frequency of the smooth sphere. This indicates a similar wake flow structure behind the two different models, as presented in Fig.3-14 and Fig.3-15 below.

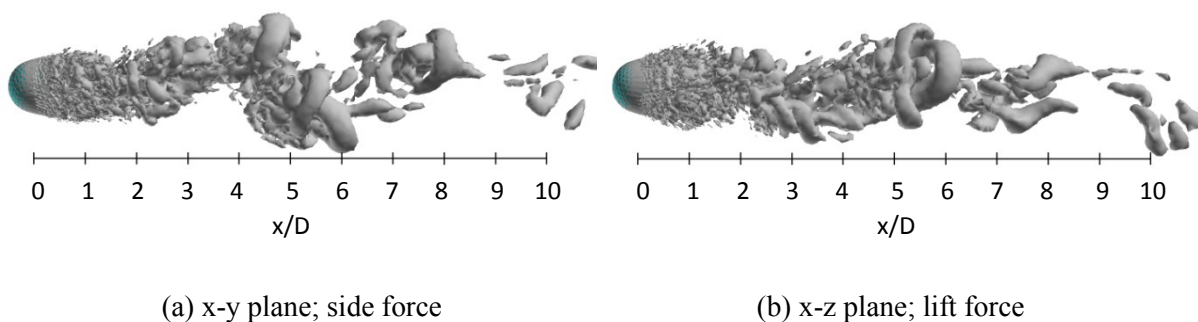


Fig.3-14 Visualization of the instantaneous vortical structures in the wake area of the stationary golf ball at $Re=4.3 \times 10^4$ using ISO surface of Q ($Ut/D=21.5$, the resultant lateral force at this moment is indicated in Fig.3-12 (b) by the red point).

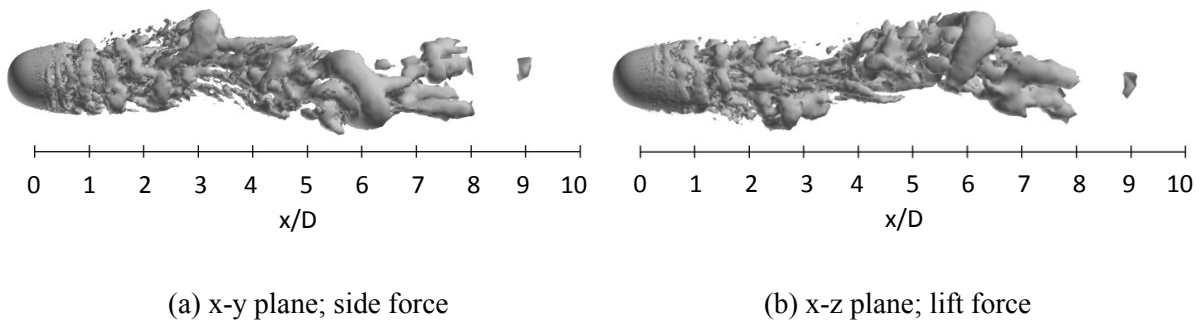


Fig.3-15 Visualization of the instantaneous vortical structures in the wake area of the stationary smooth sphere at $Re=1.0 \times 10^4$ using ISO surface of Q ($Ut/D=21.5$, the resultant lateral force at this moment is indicated in Fig.3-13 (b) by the red point).

Fig.3-14 and Fig.3-15 respectively show the instantaneous vortical structures in the wake areas of the golf ball and smooth sphere using the Q -criterion method³⁵. Visualizations were obtained in two perpendicular planes. For the flow past smooth spheres at subcritical Reynolds numbers, it is well known that the flow in the wake area exhibits a large-scale wave motion^{13, 15, 16}. This feature is successfully reproduced in the present subcritical smooth sphere case, as illustrated in Fig.3-15. Interestingly, as can be clearly observed in Fig.3-14, a progressive waviness is also pronounced in the wake area in the subcritical golf ball case. In addition, for both the golf ball and smooth sphere, the wavelength of the wake flow structure spans about $6 \sim 7D$, as indicated in Fig.3-14 (a) and Fig.3-15 (a). This similarity of wavelength corresponds to the similar dominant frequencies of the lateral force oscillation exhibited in these two cases, as evidenced in Fig.3-12 (c) and Fig.3-13 (c). Around the golf ball surface, the fully separated flow quickly becomes unstable in the shear layers and vortices are generated and shed distinctly. As the flow travels further downstream into the wake area, the hairpin-shape vortical structures become apparent, as is also observed in the wake flow of the smooth sphere.

Another issue of interest regarding the wave motion in the wake flow is whether the azimuthal position of the waviness-containing plane changes. For smooth spheres specifically, it was reported^{13, 15, 16} that such a plane rotates randomly with time. In order to investigate the corresponding feature for the golf ball case, a time-dependent trace of the evolution of instantaneous vortical structures behind the golf ball is provided in Fig.3-16. As revealed in this figure, the azimuthal position at which the wave motion is performed and the vortices are shed varies irregularly in time for the golf ball case as well. These characteristics again

demonstrate that the influence of the surface roughness introduced by the dimples on the flow behaviors is somewhat limited in the subcritical regime.

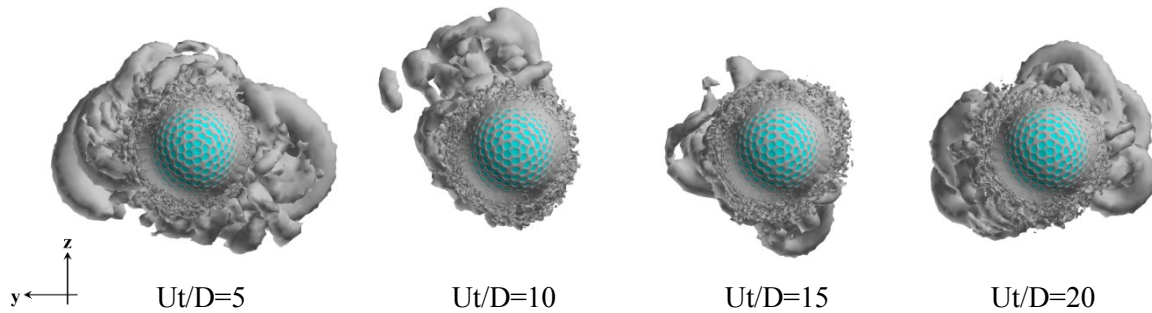


Fig.3-16 Time-dependent trace of the instantaneous vortical structures around the stationary golf ball at $Re=4.3 \times 10^4$ visualized from the upstream view.

3.4.2 Transient lateral force and wake flow structure in the critical regime

Fig.3-17 and Fig.3-18 display the time histories of the development of the drag and lateral force components in the critical Reynolds number regime for the stationary golf ball and smooth sphere respectively. As clearly depicted in Fig.3-17 (b) and Fig.3-12 (b), the resultant lateral force acting on the golf ball experiences a larger oscillation at the critical Reynolds number when compared to the subcritical case. In addition, as listed in Table.3-1, the standard deviations of both the side force and lift coefficients of the golf ball exhibit values approximately twice as large as those in the subcritical case. Similar features are also apparent for the smooth sphere at the critical Reynolds number when compared to the corresponding subcritical case. Concerning the direction of the resultant lateral force, generally, it varies irregularly with time for both models. However, in the case of the golf ball, the variations of the side force and the lift force sometimes follow the opposite trends (i.e. the side force increases while the lift force decreases). This, interestingly, makes the curve of the total lateral force shown in Fig.3-17 (b) somewhat tilted along the direction parallel to the line $C_l/C_s=-1$.

Respectively shown in Fig.3-17 (c) and Fig.3-18 (c) are the power spectra of the side force and lift coefficients for the stationary golf ball and smooth sphere in the critical regime. For the smooth sphere, as revealed in Fig.3-18 (c), the single dominant frequency that appears at the critical Reynolds number remains similar to the Strouhal number exhibited in the subcritical case which is associated with the large-scale wake instability. For the golf ball, as indicated in Fig.3-17 (c), the lift force component exhibits a dominant frequency close to the one that corresponds to the large-scale wake instability at the subcritical Reynolds

number, whereas the side force component exhibits a visibly lower dominant frequency. This leads to a noticeable difference in the wavelengths of the wake flow structures between the golf ball and the smooth sphere, as presented in Fig.3-19 and 3-20.

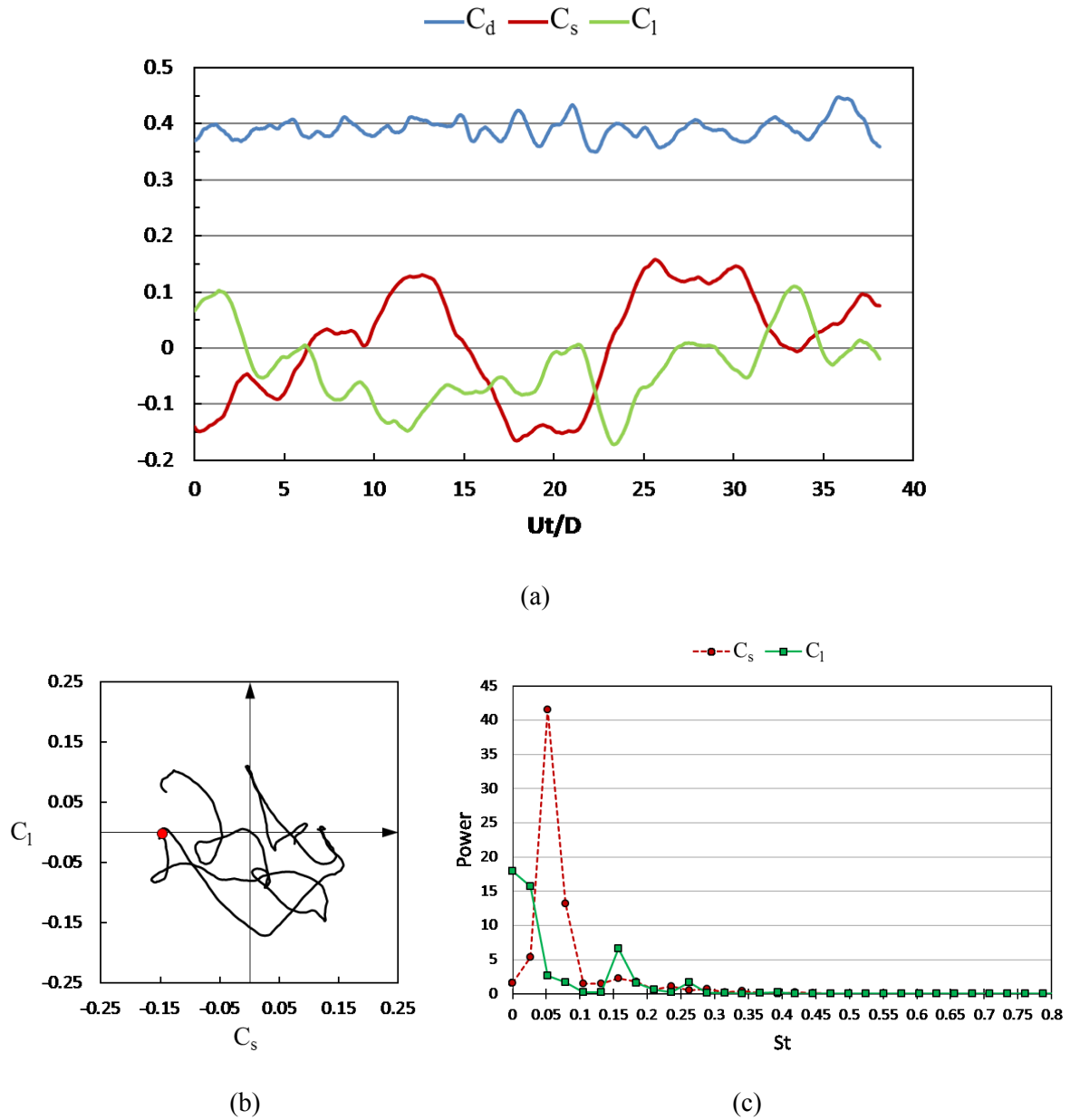
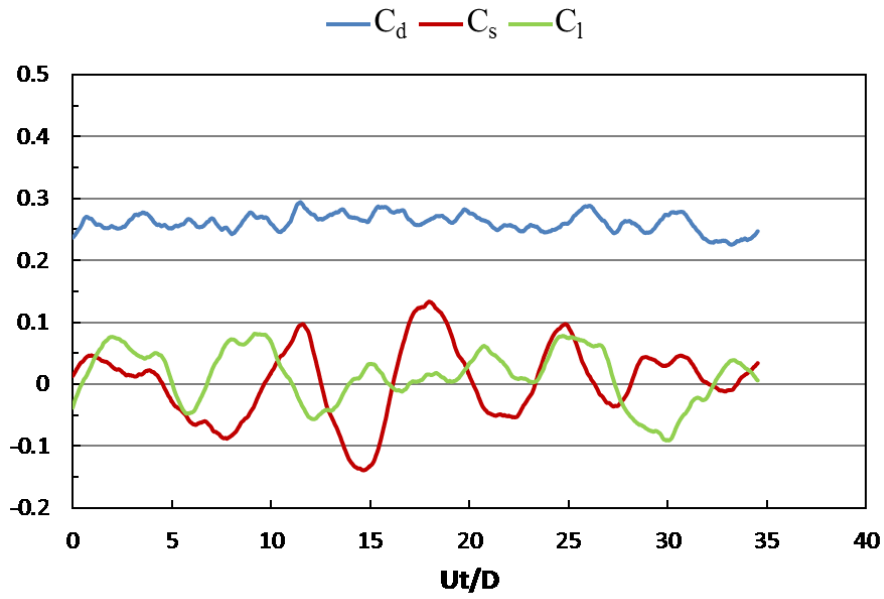
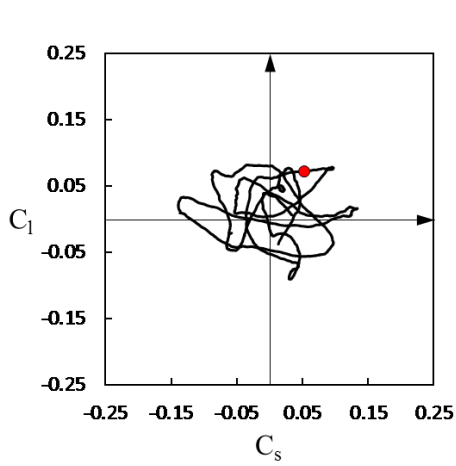


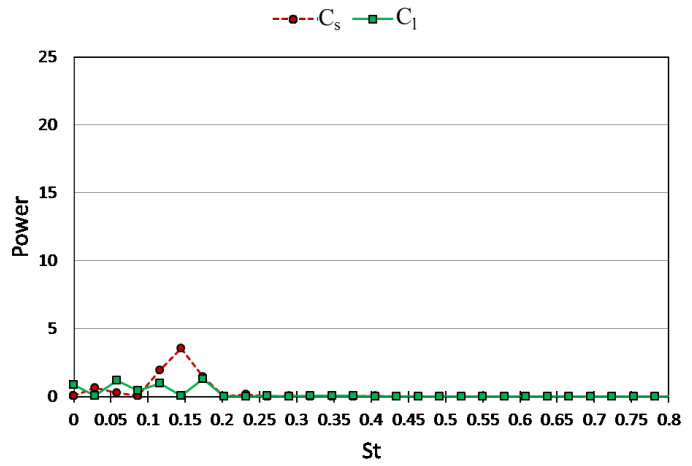
Fig.3-17 Time series of the drag and lateral force coefficients for the stationary golf ball at $Re=7.5 \times 10^4$ after the flow reached a statistically steady state: (a) temporal evolution of the drag coefficient C_d , side force coefficient C_s and lift coefficient C_l ; (b) phase diagram of C_s and C_l , the red point represents the resultant lateral force at the non-dimensional moment indicated in Fig.3-19; (c) power spectrum of the side force coefficient C_s and lift coefficient C_l .



(a)

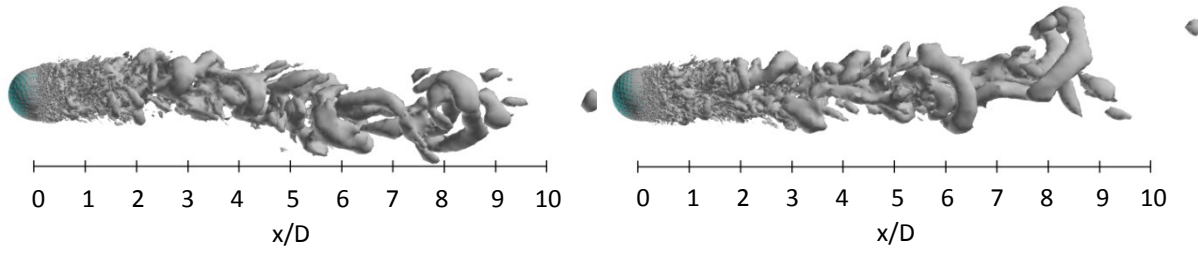


(b)



(c)

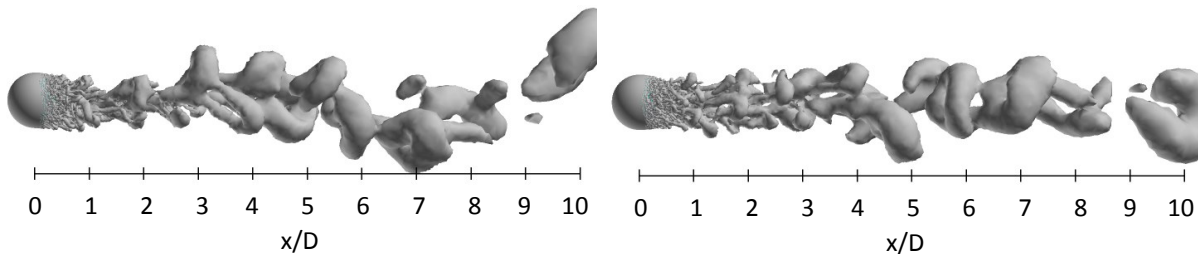
Fig.3-18 Time series of the drag and lateral force coefficients for the stationary smooth sphere at $Re=2.0 \times 10^5$ after the flow reached a statistically steady state: (a) temporal evolution of the drag coefficient C_d , side force coefficient C_s and lift coefficient C_l ; (b) phase diagram of C_s and C_l , the red point represents the resultant lateral force at the non-dimensional moment indicated in Fig.3-20; (c) power spectrum of the side force coefficient C_s and lift coefficient C_l .



(a) x-y plane; side force

(b) x-z plane; lift force

Fig.3-19 Visualization of the instantaneous vortical structures in the wake area of the stationary golf ball at $Re=7.5 \times 10^4$ using ISO surface of Q ($Ut/D=20.8$, the resultant lateral force at this moment is indicated in Fig.3-17 (b) by the red point).



(a) x-y plane; side force

(b) x-z plane; lift force

Fig.3-20 Visualization of the instantaneous vortical structures in the wake area of the stationary smooth sphere at $Re=2.0 \times 10^5$ using ISO surface of Q ($Ut/D=25.5$, the resultant lateral force at this moment is indicated in Fig.3-18 (b) by the red point).

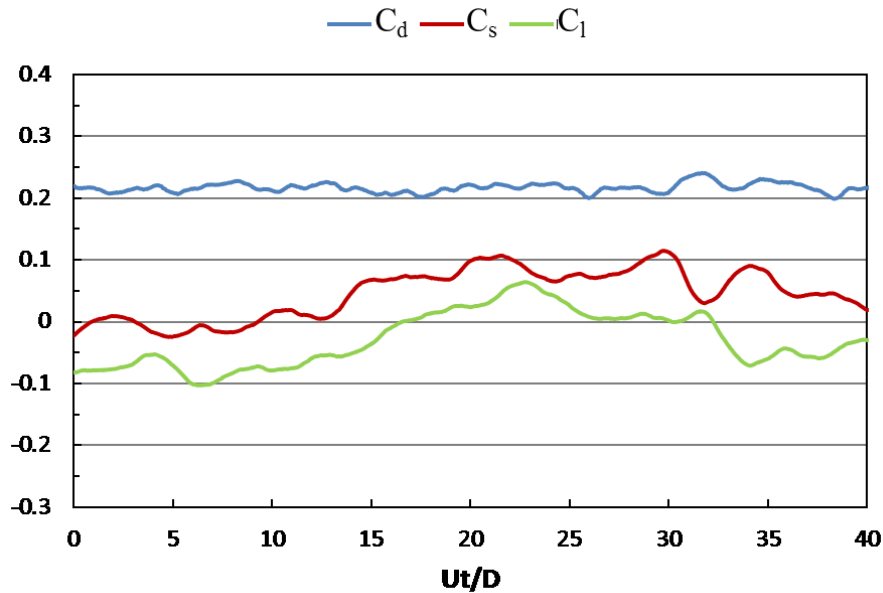
Respectively provided in Fig.3-19 and Fig.3-20 are the instantaneous vortical structures in the wake areas of the golf ball and the smooth sphere at the critical Reynolds numbers. Somewhat apparent for both models is the presence of the large-scale wave motions and the shed hairpin structures in the wake regions. Agreeing well with the experimental data by Taneda¹³, the wavelength of the wake flow structure for the critical smooth sphere case remains about $6 \sim 7D$, as indicated in Fig.3-20 (a), which is similar to that observed in the corresponding subcritical case. This corresponds to the similar frequencies of the variations of the lateral force components exhibited in these two different Reynolds number regimes. For the golf ball, however, a larger wavelength of the wake flow structure which spans about $13D$ is pronounced in the critical case, as indicated in Fig.3-19 (a). This relates to the lower dominant frequency of the variation of the lateral force components exhibited in the critical case when compared to the corresponding subcritical case.

3.4.3 Transient lateral force and wake flow structure in the supercritical regime

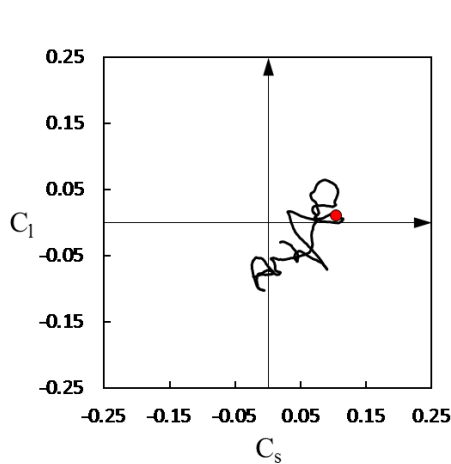
Displayed in Fig.3-21 and Fig.3-22 are the time histories of the development of the drag and the lateral force components in the supercritical Reynolds number regime for the stationary golf ball and smooth sphere respectively. One can clearly observe from Fig.3-21 (b) and Fig.3-22(b) that the oscillation of the lateral force acting on the golf ball exhibits a considerably smaller magnitude when compared to the smooth sphere. Meanwhile, as listed in Table.3-1, compared with the respective critical cases, the standard deviations of both the side force and lift coefficients of the golf ball decrease in the supercritical regime, whereas the corresponding statistics vary following an opposite trend in the smooth sphere case. Concerning how the lateral force direction varies in the supercritical regime, unlike the corresponding behaviors observed at the subcritical and critical Reynolds numbers, the curves respectively representing the time evolution of the side force and lift force barely intersect each other, at least within a long time interval, in both the golf ball and smooth sphere cases. These features, interestingly, result in a somewhat less random variation of the direction of the resultant lateral force for both models. It can be clearly observed in Fig.3-22 (b) that the stationary smooth sphere placed in the supercritical flow is subjected to a nonzero lateral force during the whole time period, and the lateral force exhibits a rotation trend with time around the origin in the phase diagram, which represents the streamwise axis that goes across the center of the sphere (x axis). These phenomena agree very well with those observed by Taneda¹³ and Constantinescu et al.¹⁵. Qualitatively similar features are also evident in the supercritical golf ball case, as clearly shown in Fig.3-21 (b). However, it can be suggested from the differences between the variations of the lateral forces shown in Fig.3-21 (b) and Fig.3-22 (b) that the total lateral force is to some extent suppressed for the golf ball when compared to the smooth sphere. This is assumed to be affected by the generation of the small-scale vortices on the golf ball surface. It is likely that the small-scale vortices which are prematurely induced by the dimples diffuse the momentum of the large-scale eddies and consequently weaken the large-scale vortex structures in the near-wall region behind the golf ball's rear surface, which is actually beneficial in the reduction of the lateral force oscillation.

Respectively shown in Fig.3-21 (c) and Fig.3-22 (c) are the power spectra of the side force and lift coefficients for the stationary golf ball and smooth sphere in the supercritical regime. It is interesting to note that both models have broadband power spectra at the supercritical Reynolds numbers. However, the dominant frequency which stays around the Strouhal number that is associated with the large-scale wake instability in the subcritical and critical cases appears in the supercritical golf ball case as well. Similar features are also

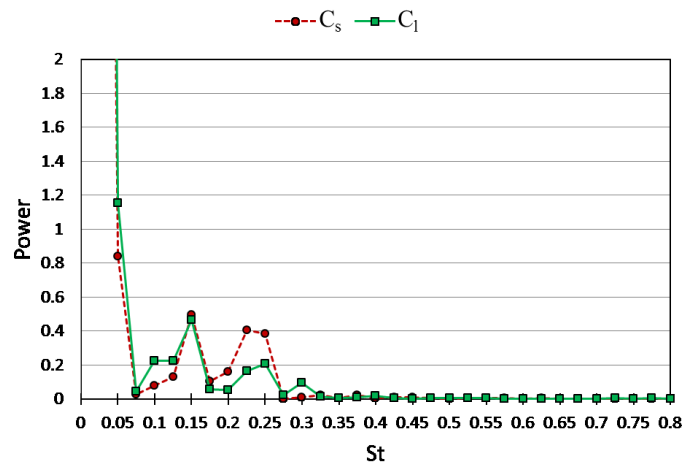
evident in the supercritical smooth sphere case. The higher frequencies that appear in the power spectra of both models are probably associated with the small-scale vortex shedding around the geometry surfaces and the corresponding shear-layer instabilities in the supercritical regime.



(a)

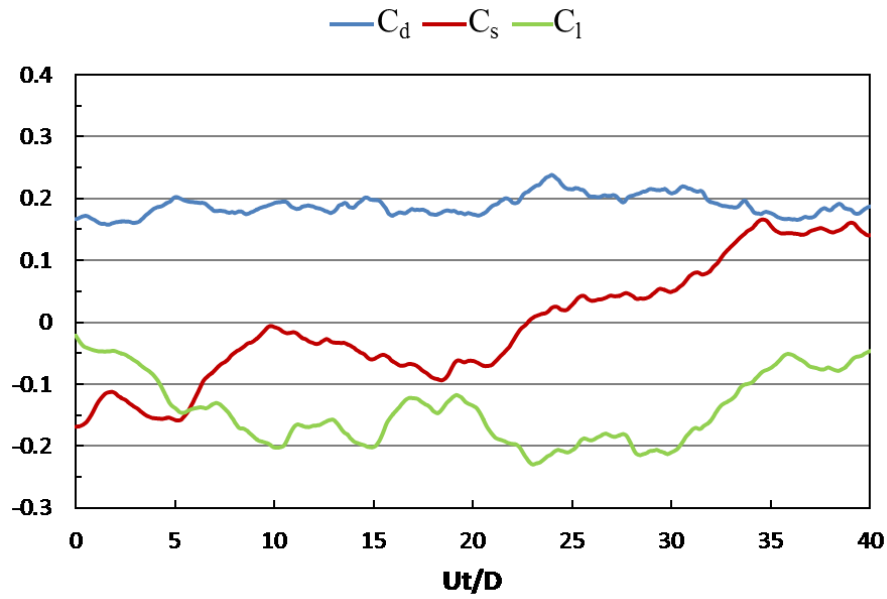


(b)

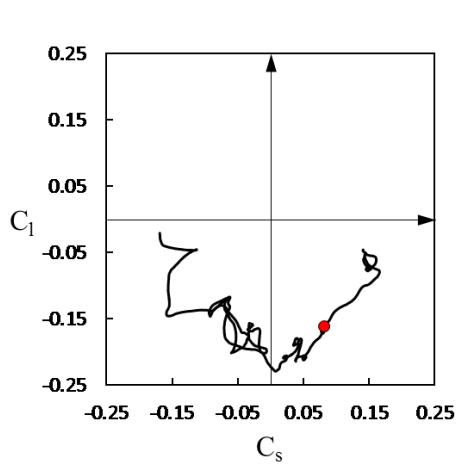


(c)

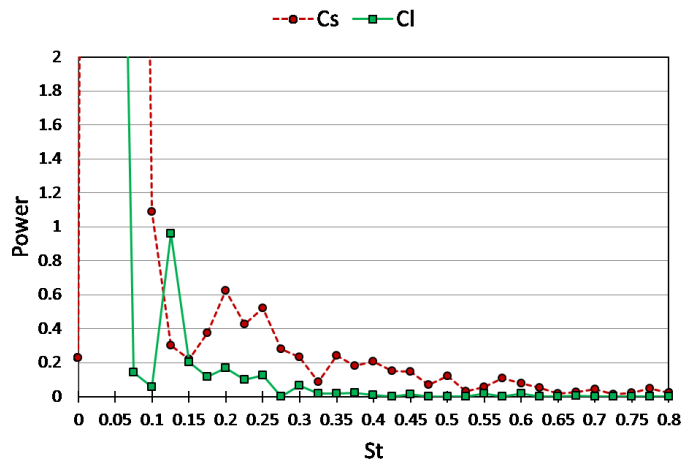
Fig.3-21 Time series of the drag and lateral force coefficients for the stationary golf ball at $Re=1.1 \times 10^5$ after the flow reached a statistically steady state: (a) temporal evolution of the drag coefficient C_d , side force coefficient C_s and lift coefficient C_l ; (b) phase diagram of C_s and C_l , the red point represents the resultant lateral force at the non-dimensional moment indicated in Fig.3-23; (c) power spectrum of the side force coefficient C_s and lift coefficient C_l .



(a)

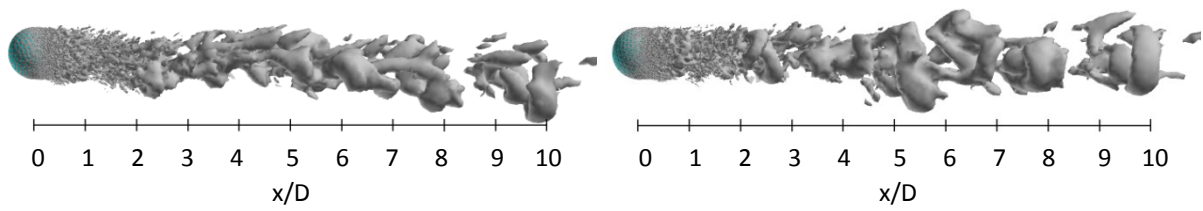


(b)



(c)

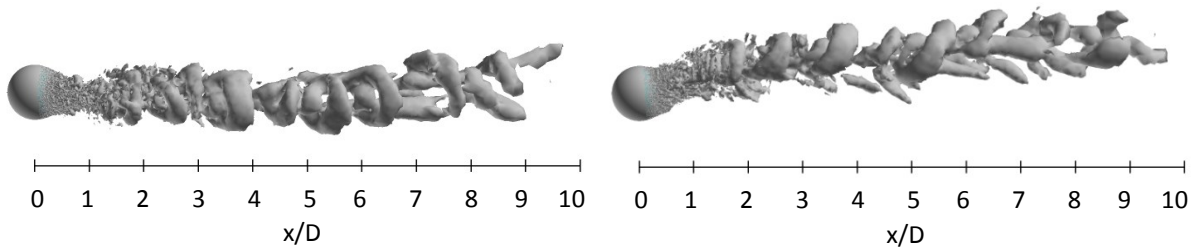
Fig.3-22 Time series of the drag and lateral force coefficients for the stationary smooth sphere at $Re=1.14 \times 10^6$ after the flow reached a statistically steady state: (a) temporal evolution of the drag coefficient C_d , side force coefficient C_s and lift coefficient C_l ; (b) phase diagram of C_s and C_l , the red point represents the resultant lateral force at the non-dimensional moment indicated in Fig.3-24; (c) power spectrum of the side force coefficient C_s and lift coefficient C_l .



(a) x-y plane; side force

(b) x-z plane; lift force

Fig.3-23 Visualization of the instantaneous vortical structures in the wake area of the stationary golf ball at $Re=1.1\times 10^5$ using ISO surface of Q ($Ut/D=28.9$, the resultant lateral force at this moment is indicated in Fig.3-21 (b) by the red point).



(a) x-y plane; side force

(b) x-z plane; lift force

Fig.3-24 Visualization of the instantaneous vortical structures in the wake area of the stationary smooth sphere at $Re=1.14\times 10^6$ using ISO surface of Q ($Ut/D=31.9$, the resultant lateral force at this moment is indicated in Fig.3-22 (b) by the red point).

Respectively shown in Fig.3-23 and Fig.3-24 are the instantaneous vortical structures in the wake areas of the golf ball and smooth sphere at the supercritical Reynolds numbers. As indicated in the figures, a large-scale vortex shedding appears in both the wake flow of the smooth sphere, which agrees well with Constantinescu et al. ¹⁵, and the wake flow of the golf ball. In the near-wall region behind the smooth sphere, the flow is severely deflected due to a strong oscillation, and a considerable lateral force is generated on the geometry, as indicated in Fig.3-22. As the flow travels further downstream, the completely asymmetric wake structures are formed, which significantly deviate from the streamwise axis that goes across the center of the sphere (x axis). The orientation of the asymmetry of the wake flow corresponds to the direction of the instantaneous resultant lateral force acting on the sphere. In contrast, the flow in the near-wall region behind the golf ball exhibits a visibly weaker oscillation and a less tilted pattern, as illustrated in Fig.3-23, and a visibly smaller lateral

force is acting on the golf ball when compared to the smooth sphere, as indicated in Fig.3-21. The shed vortical structures travel into the further downstream area approximately following the direction which is parallel to the streamwise axis that goes across the center of the golf ball (x axis), despite a slight deflection corresponding to the small instantaneous lateral force acting on the golf ball, as can be observed in Fig.3-23 (a).

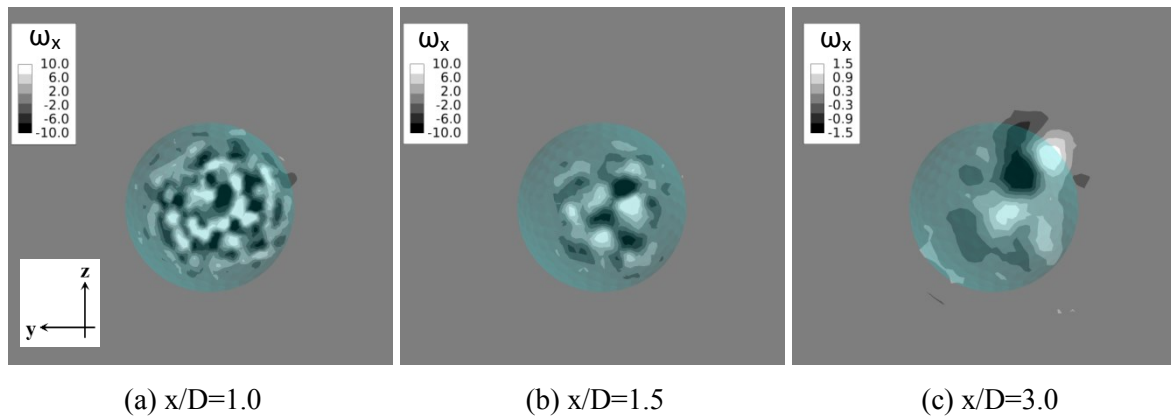


Fig.3-25 Streamwise vorticity component in the wake flow of the stationary golf ball viewed in the crossflow plane at: (a) $x/D=1.0$; (b) $x/D=1.5$; (c) $x/D=3.0$; $Re=1.1 \times 10^5$ ($Ut/D=28.9$).

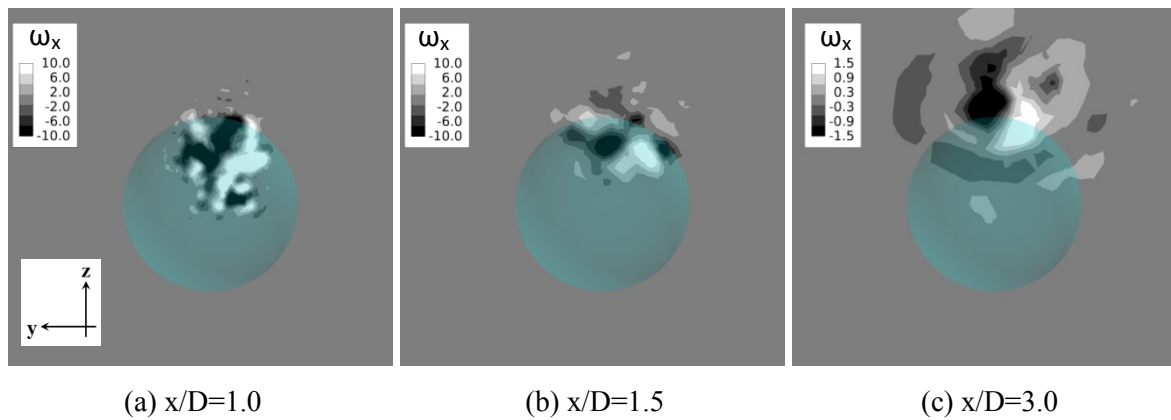
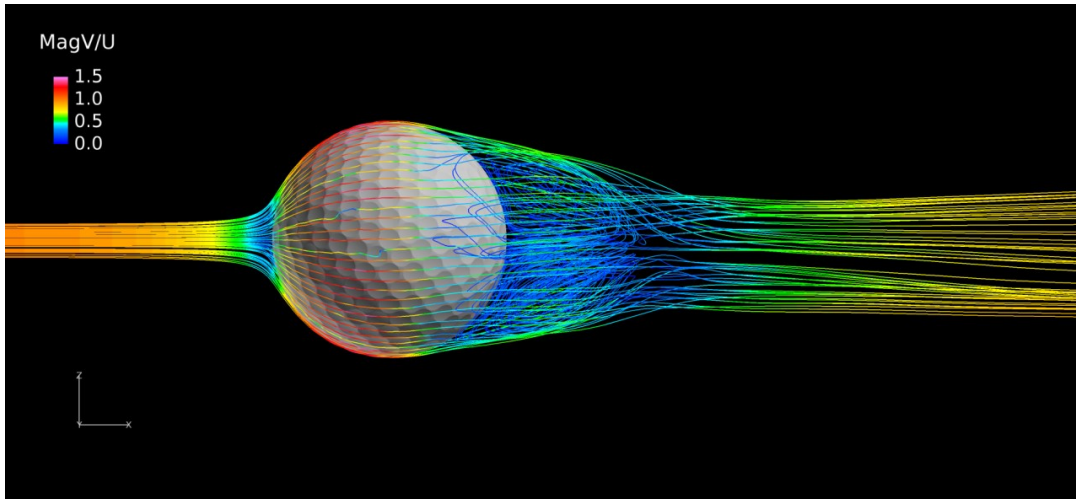


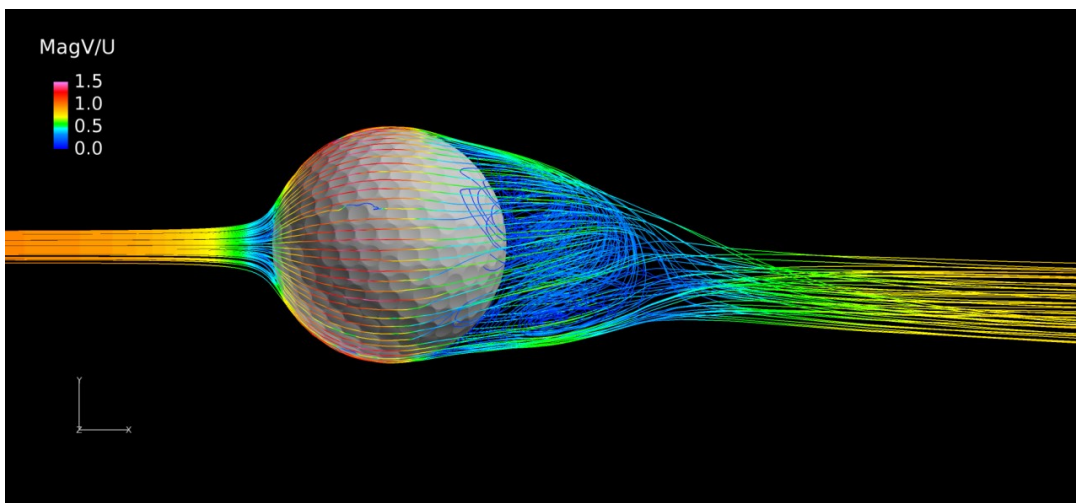
Fig.3-26 Streamwise vorticity component in the wake flow of the stationary smooth sphere viewed in the crossflow plane at: (a) $x/D=1.0$; (b) $x/D=1.5$; (c) $x/D=3.0$; $Re=1.14 \times 10^6$ ($Ut/D=31.9$).

Further insights into the differences in the wake structures between the two supercritical stationary cases are provided in Fig.3-25 and Fig.3-26 by the investigation of the streamwise vorticity component ω_x (normalized by multiplying D/U) visualized in the crossflow planes (normal to the freestream direction) located at $1.0D$, $1.5D$ and $3.0D$ from the center of the golf ball and the smooth sphere. As indicated in Fig.3-26, a pair of counter-rotating vortices (twin vortices) is clearly shown behind the smooth sphere at each of the

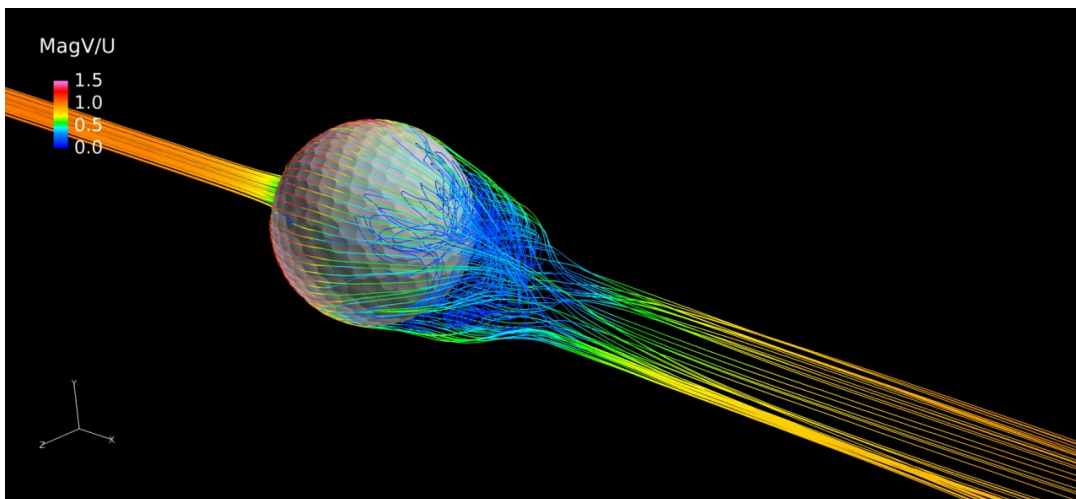
three different locations, and it deviates further away from the streamwise axis that goes across the geometry center (x axis) as the flow travels downstream. It is considered that momentum is generated between the twin vortices along the direction normal to a line connecting the center of each vortex, which gives rise to the lateral force acting on the sphere in the opposite direction. In contrast, the vortices behind the golf ball show more random patterns and a more concentrated distribution around the geometry center at $x/D=1.0$ and $x/D=1.5$, as indicated in Fig.3-25 (a) and Fig.3-25 (b), while the twin vortices are observed at a location further downstream ($x/D=3.0$), as indicated in Fig.3-25 (c). Compared with the smooth sphere, the twin vortices behind the golf ball remain less deviated from the x axis. Further visualization of the different twin vortices behind the golf ball and the smooth sphere is provided in Fig.3-27 and Fig.3-28.



(a)

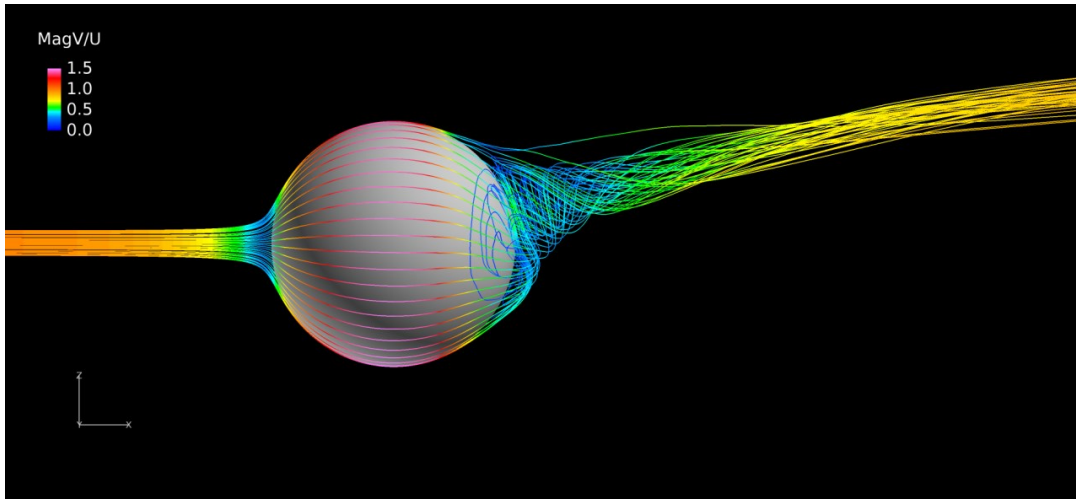


(b)

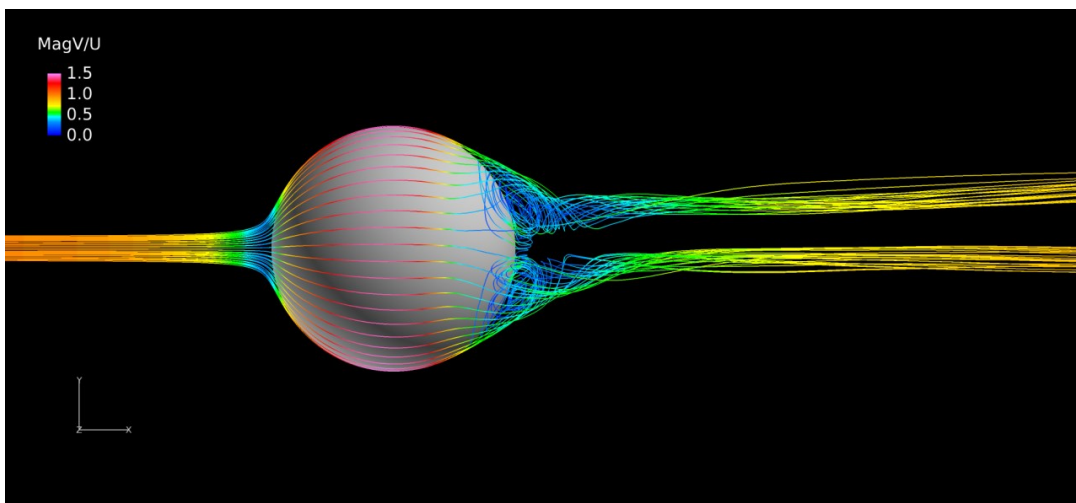


(c)

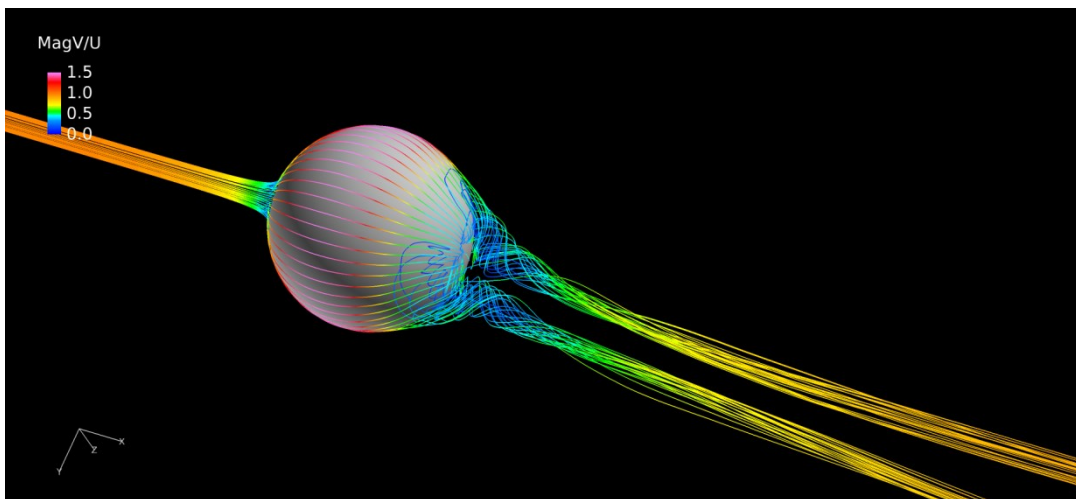
Fig.3-27 Streamlines around the stationary golf ball at $Re=1.1 \times 10^5$ viewed from: (a) -y view; (b) +z view; (c) an isometric view; MagV represents the magnitude of velocity.



(a)



(b)



(c)

Fig.3-28 Streamlines around the stationary smooth sphere at $Re=1.14 \times 10^6$ viewed from: (a) -y view; (b) +z view; (c) an isometric view; $MagV$ represents the magnitude of velocity.

Chapter 4: Flow past the self-spinning golf ball and smooth sphere

This chapter presents the investigation of flow past the self-spinning golf ball and smooth sphere. First, the variations of the drag and lift coefficients are presented. The underlying mechanisms of the ordinary Magnus effect and negative Magnus effect are discussed. Finally, the transient features of the aerodynamic forces and wake flow structure are presented.

4.1 Variation of the drag and lift coefficients

Fig.4-1 displays the drag coefficients of the self-spinning golf ball and smooth sphere at the subcritical, critical and supercritical Reynolds numbers. The results for the corresponding non-rotating cases are also plotted for comparison. For the golf ball, the self-spinning cases were calculated at $Re=4.3\times 10^4$, 7.5×10^4 and 1.1×10^5 . For the smooth sphere, the self-spinning cases were calculated at $Re=1.0\times 10^4$, 2.0×10^5 and 1.14×10^6 . As mentioned in Chapter 2, for all the spinning cases considered in the present study, a backspin motion is imposed on the geometries which rotate about the 'y' axis with the spin parameter being set as $\Gamma=0.1$. Fig.4-2 plots the results of the lift coefficient as a function of the Reynolds number for all the corresponding self-spinning cases shown in Fig.4-1.

As clearly displayed in Fig.4-2, for both the self-spinning golf ball and smooth sphere, the lift forces exhibit a negative value (the negative Magnus effect) in the critical Reynolds number regime with current spin parameter ($\Gamma=0.1$), although the magnitude of the lift force acting on the golf ball is visibly smaller when compared to the smooth sphere. In contrast, for both rotating models, positive lift forces (the ordinary Magnus effect) are generated in the subcritical and supercritical Reynolds number regimes. However, the dependence of the change of the positive lift force on Reynolds number is different for each of the models. As can be observed in Fig.4-2, the lift force acting on the golf ball at the supercritical Reynolds number is slightly smaller than that at the subcritical Reynolds number, whereas for the smooth sphere, the supercritical lift force is approximately twice as large as the subcritical one. The generation of the positive and negative lift forces reproduced by the present simulations qualitatively agrees well with the conclusions obtained in the previous literatures 3, 9-11.

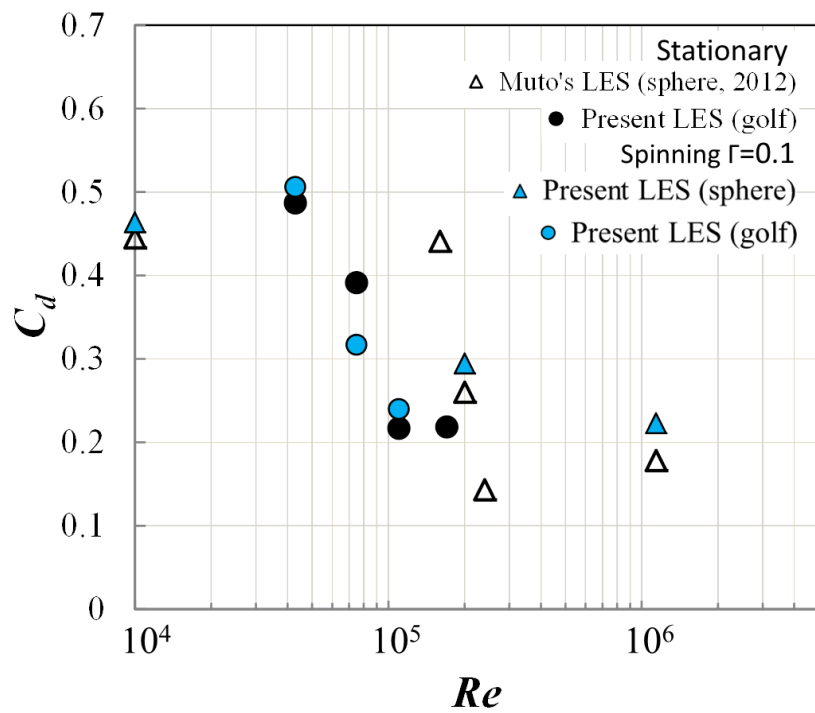


Fig.4-1 Comparison of the drag coefficients between the self-spinning and stationary cases for the golf ball and smooth sphere.

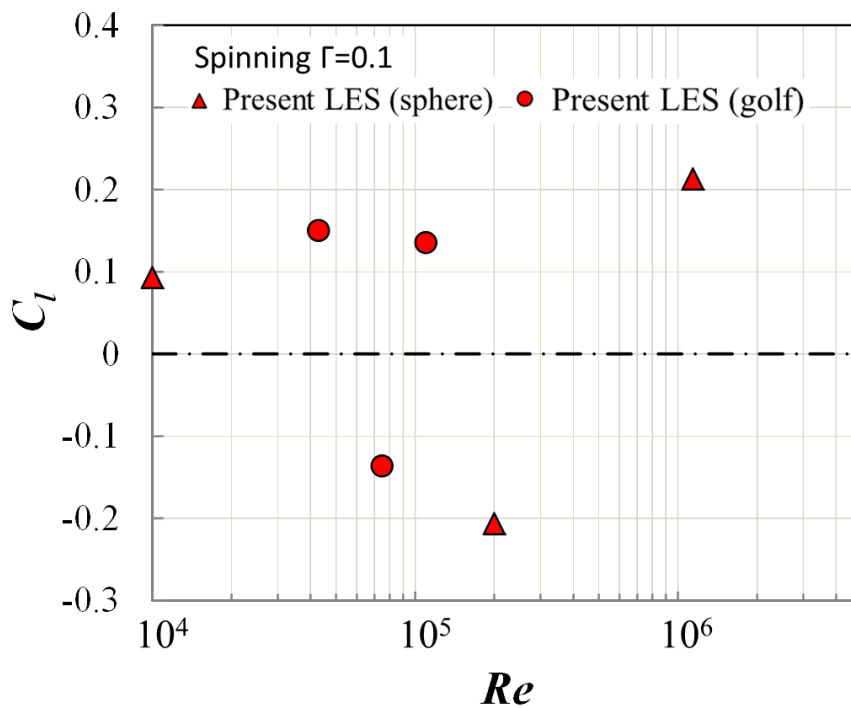


Fig.4-2 Lift coefficients of the corresponding self-spinning golf ball and smooth sphere cases shown in Fig.4-1.

The shifting of the drag coefficients as a result of the self-spinning motion is displayed in Fig.4-1 for both the golf ball and smooth sphere cases. As clearly shown in this figure, for the smooth sphere, the drag coefficients increase at each of the three different Reynolds numbers when the self-spinning motion is imposed on the geometry. For the golf ball, the drag coefficients increase slightly while the ball is rotating at the subcritical and supercritical Reynolds numbers. This is similar to the variations for the rotating smooth sphere in the same Reynolds number regimes. At the critical Reynolds number, however, the drag force acting on the rotating golf ball exhibits a considerable drop compared with the corresponding non-rotating golf ball. This trend is apparently opposite to the drag variation of the rotating smooth sphere at the critical Reynolds number. More quantitative discussions of the drag and lift force variations in the self-spinning cases are presented in detail in section 4.4.

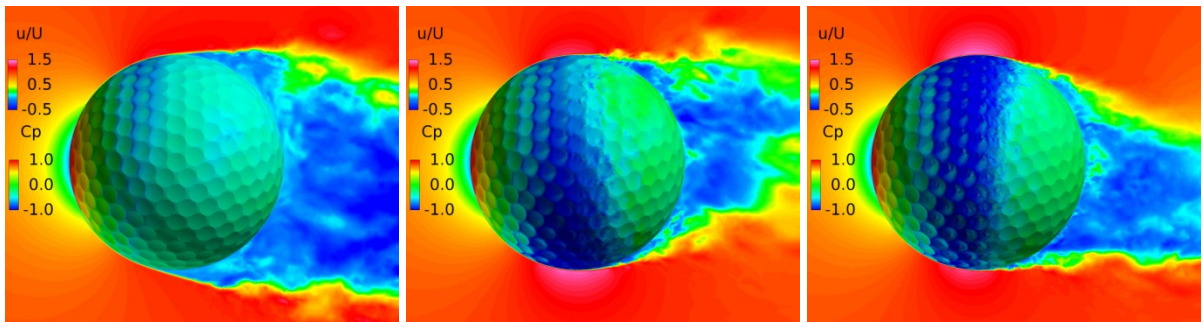
4.2 Flow visualizations around the self-spinning golf ball and smooth sphere

Fig.4-3 and Fig.4-6 respectively show the instantaneous surface pressure distribution and the non-dimensional streamwise velocity distribution in the flow field of the rotating golf ball and smooth sphere. Fig.4-4 and Fig.4-5 respectively display the instantaneous azimuthal vorticity around the flow separation points on the top side and bottom side of the rotating golf ball. Fig.4-7 and Fig.4-8 respectively display the instantaneous azimuthal vorticity around the flow separation points on the top side and bottom side of the rotating smooth sphere. For both the golf ball and smooth sphere, the top side of the geometry spins in the direction moving with the approaching flow, whereas the bottom side of the geometry spins in the direction moving against the approaching flow.

In the subcritical regime, as shown in the figures, the boundary layers on both the top and bottom sides of each of the rotating models remain laminar. The shear layers developed after the full flow separation becomes unstable as they travel further downstream. These features are very similar to those exhibited in the stationary cases in the same Reynolds number regime. However, the self-spinning motion results in an apparent difference in the position of flow separation between the two sides of the geometries. For the golf ball, the flow detaches around 85° on the top side, and detaches around 75° on the bottom side. For the smooth sphere, similarly, the flow separates at a position more downstream on the top side (around 85°) than on the bottom side (around 78°). As a result of these asymmetries, the wake flow behind the rear surface of each of the models is tilted downwards for both the golf ball and smooth sphere.

In the supercritical regime, the boundary layers on both the top and bottom sides of each of the rotating models become turbulent, although for the golf ball it is mainly induced by the perturbation caused by the dimples, whereas for the smooth sphere it is induced mainly due to the increase in Reynolds number. As shown in the figures, one can observe that the boundary layers exhibit noticeable instability before the full flow separation and shed small-scale vortices. Additionally, the shear layers become thinner as a result of the increase in Reynolds number. However, despite the fact that the boundary layers are of characteristics totally different from each other, the patterns of the flow separation in the supercritical regime are qualitatively similar to those exhibited in the subcritical regime. For both the golf ball and smooth sphere, the flow stays attached on the geometry for a longer distance on the top side than on the bottom side at the supercritical Reynolds numbers, which likewise leads to a downward-deflected wake flow behind the rear surface of the geometry.

In the critical regime, where the negative lift force is generated, the boundary layers on the top side and the bottom side are in different states. In particular, on the top sides of both the golf ball and smooth sphere, the boundary layers do not become noticeably unstable and shed vortices that are experiencing Kelvin-Helmholtz instability until they travel some distance downstream from the separation points. These features are very similar to those exhibited in the subcritical regime, although the positions where the shear layers start to become unstable are generally closer to the separation points at the critical Reynolds numbers. On the bottom sides, however, the boundary layers exhibit clearly different features. For the smooth sphere, the boundary layer first separates after it passes the equator but reattaches to the solid wall at a position further downstream. For the golf ball, similarly, the near-wall flow shows the features typical of the turbulent boundary layer as exhibited in the corresponding supercritical case. As a result, the flow passing over both models in the critical regime detaches at a position more downstream on the bottom side than on the top side, which leads to an upward-deflected wake flow behind the rear surface of the geometry.

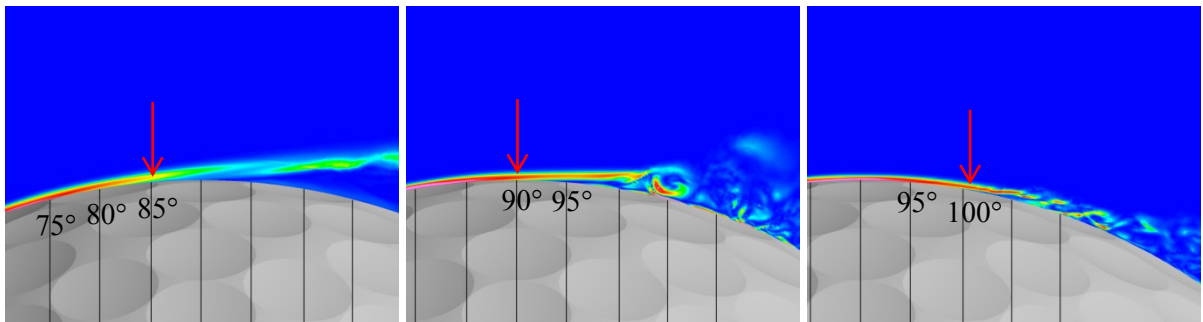


(a) $Re=4.3 \times 10^4$

(b) $Re=7.5 \times 10^4$

(c) $Re=1.1 \times 10^5$

Fig.4-3 Instantaneous surface pressure distribution and non-dimensional streamwise velocity distribution in the wake area of the self-spinning golf ball at the: (a) subcritical, (b) critical, (c) supercritical Reynolds numbers; incoming flow is from $-x$ to $+x$; backspin motion is imposed around 'y' axis; the velocity distribution is viewed in section $y=0$.

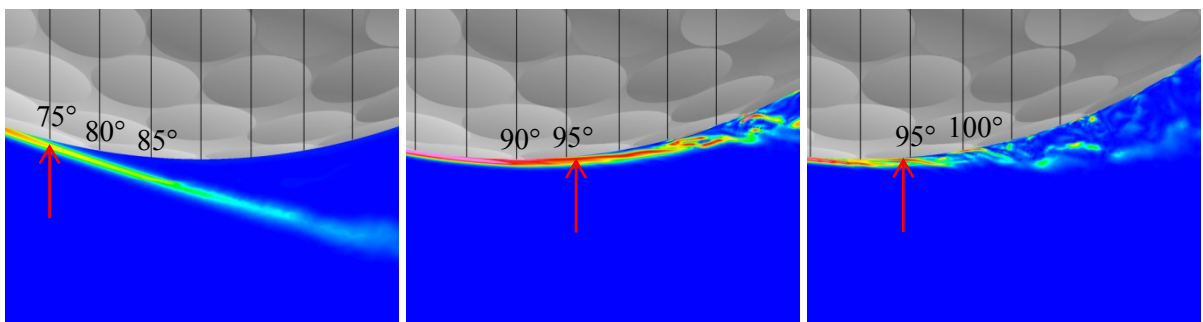


(a) $Re=4.3 \times 10^4$

(b) $Re=7.5 \times 10^4$

(c) $Re=1.1 \times 10^5$

Fig.4-4 Contours of the instantaneous azimuthal vorticity viewed in section $y=0$ around the separation point on the top side of the corresponding rotating golf balls shown in Fig.4-3; the red arrows indicate the positions of flow separation.

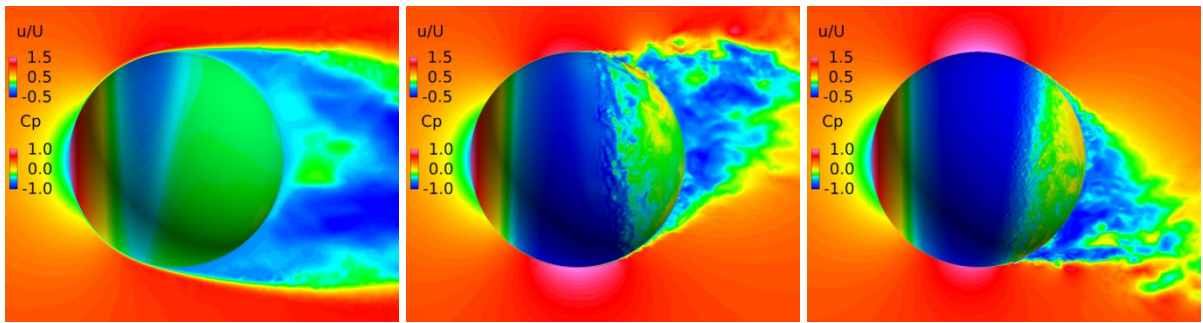


(a) $Re=4.3 \times 10^4$

(b) $Re=7.5 \times 10^4$

(c) $Re=1.1 \times 10^5$

Fig.4-5 Contours of the instantaneous azimuthal vorticity viewed in section $y=0$ around the separation point on the bottom side of the corresponding rotating golf balls shown in Fig.4-3; the red arrows indicate the positions of flow separation.

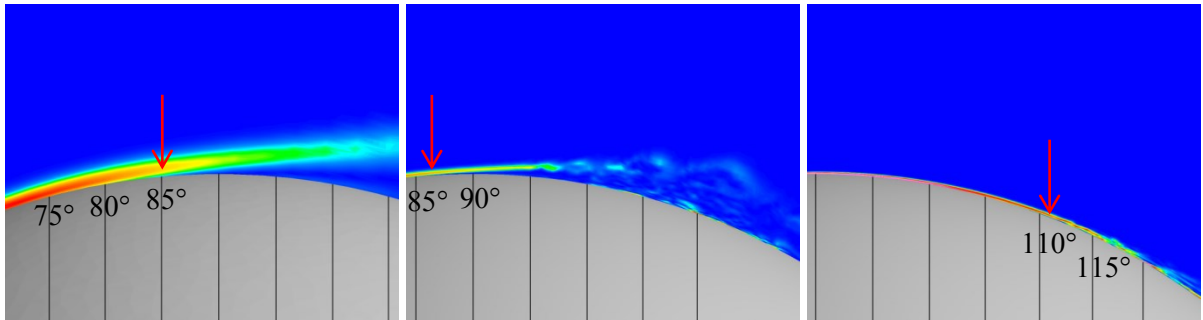


(a) $Re=1.0 \times 10^4$

(b) $Re=2.0 \times 10^5$

(c) $Re=1.14 \times 10^6$

Fig.4-6 Instantaneous surface pressure distribution and non-dimensional streamwise velocity distribution in the wake area of the self-spinning smooth sphere at the: (a) subcritical, (b) critical, (c) supercritical Reynolds numbers; incoming flow is from $-x$ to $+x$; backspin motion is imposed around 'y' axis; the velocity distribution is viewed in section $y=0$.

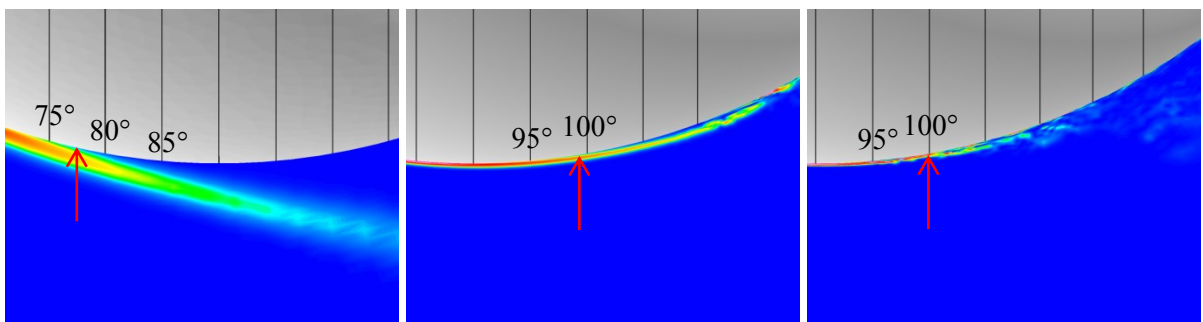


(a) $Re=1.0 \times 10^4$

(b) $Re=2.0 \times 10^5$

(c) $Re=1.14 \times 10^6$

Fig.4-7 Contours of the instantaneous azimuthal vorticity viewed in section $y=0$ around the separation point on the top side of the corresponding rotating smooth spheres shown in Fig.4-6; the red arrows indicate the positions of flow separation.



(a) $Re=1.0 \times 10^4$

(b) $Re=2.0 \times 10^5$

(c) $Re=1.14 \times 10^6$

Fig.4-8 Contours of the instantaneous azimuthal vorticity viewed in section $y=0$ around the separation point on the bottom side of the corresponding rotating smooth spheres shown in Fig.4-6; the red arrows indicate the positions of flow separation.

4.3 Mechanism of the ordinary and negative Magnus effect

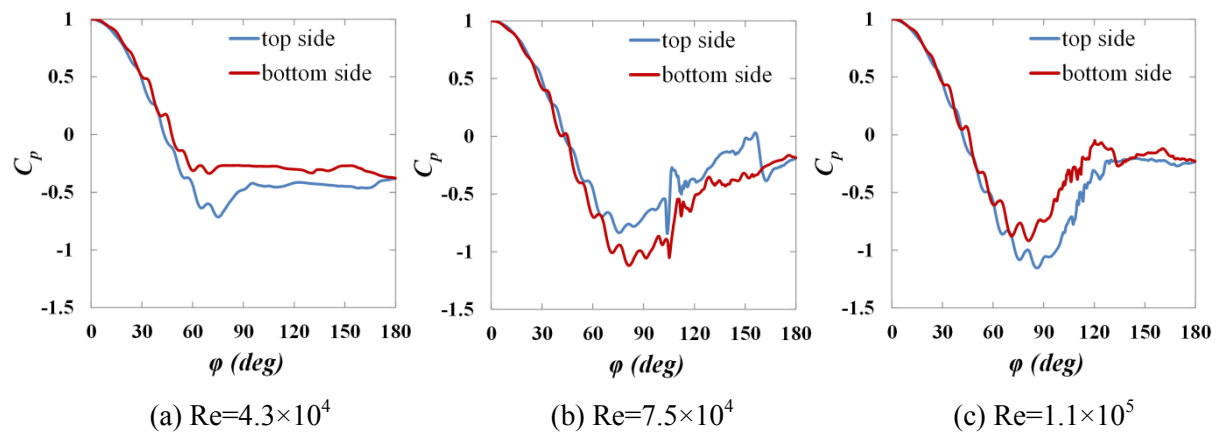


Fig.4-9 Instantaneous surface pressure distribution obtained in section $y=0$ respectively along the top side and bottom side of the golf balls displayed in Fig.4-3.

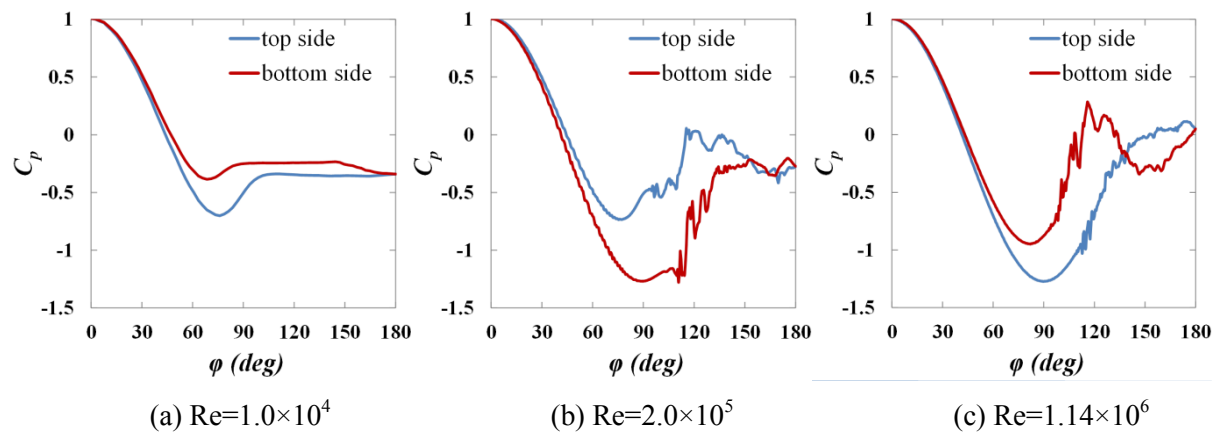


Fig.4-10 Instantaneous surface pressure distribution obtained in section $y=0$ respectively along the top side and bottom side of the smooth spheres displayed in Fig.4-6.

Fig.4-9 and Fig.4-10 respectively show the instantaneous pressure coefficient distributions obtained in section $y=0$ along the top side and bottom side of the rotating golf ball and smooth sphere.

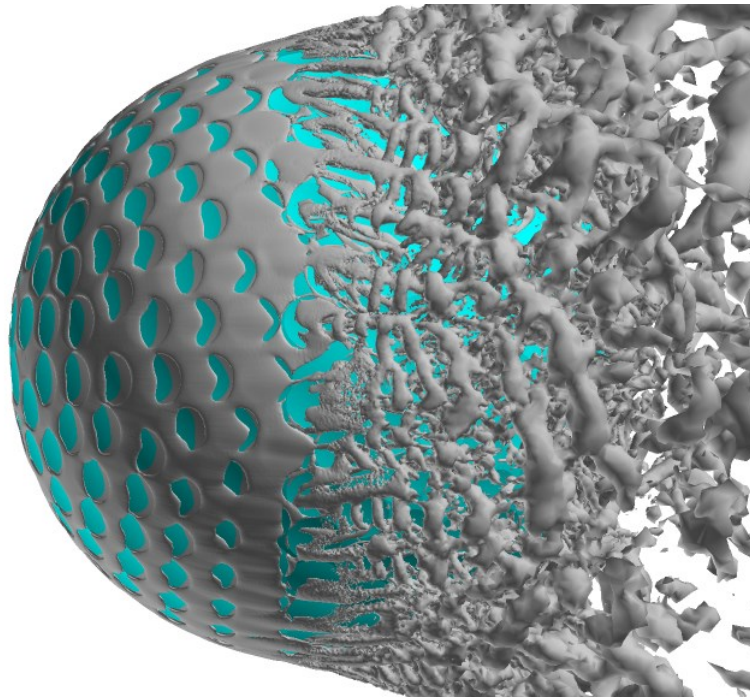
As presented before in section 4.2, for both models in the subcritical and supercritical regimes, the boundary layers on the top side and the bottom side exist in the same state, but the flow on the top side travels a longer distance before full separation. This is attributed to the difference between the effects of the self-spinning motion on the flow passing over the two different sides. In particular, on the top side, the near-wall flow gains momentum as the geometries rotate with the approaching flow, whereas on the bottom side, the near-wall flow loses momentum as the geometries rotate against the approaching flow. With the increased

momentum, the near-wall flow on the top side is able to overcome the adverse pressure gradient more and separate at a position further downstream than on the bottom side. This consequently results in the pressure on the top side experiencing a steeper drop and a lower minimum value than that on the bottom side, as shown in Fig.4-9 (a), (c) and Fig.4-10 (a), (c), which consequently gives rise to a positive lift force acting on the geometries, i.e. the ordinary Magnus effect.

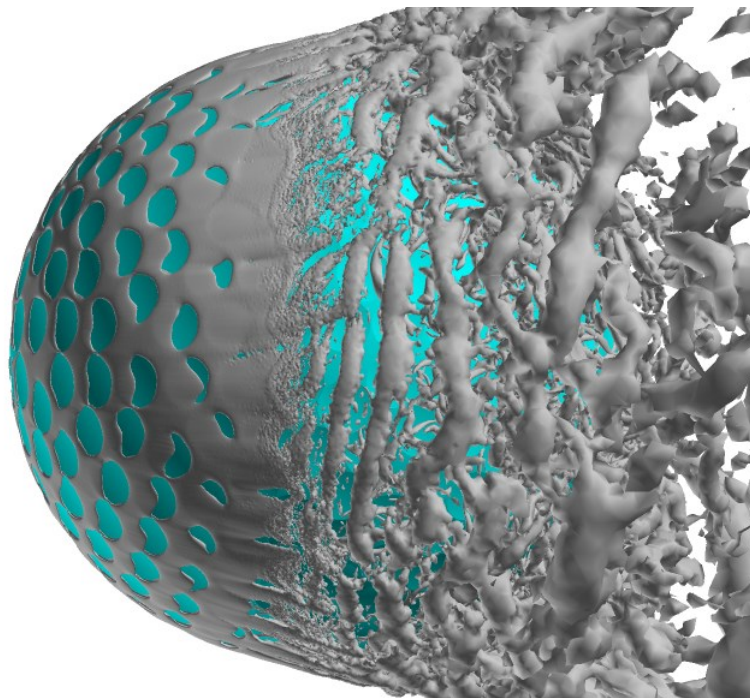
In contrast, as presented before in section 4.2, for both models in the critical regime, the boundary layer on the top side stays laminar, whereas on the bottom side it becomes turbulent. This is attributed to the difference in the relative Reynolds number between the two different sides. In particular, the relative Reynolds number, which is calculated based on the free stream velocity with respect to the geometry surface, is locally higher on the bottom side than on the top side due to the backspin motion. This makes the flow passing over the bottom side more sensitive to perturbations, and thus promotes the laminar-turbulent boundary layer transition on this side, whereas on the top side the transition is accordingly suppressed due to the lower relative Reynolds number. As a result of the turbulent state, the flow on the bottom side has higher momentum in the near-wall region, and thus separates at a position further downstream than on the top side. This consequently leads to a lower pressure on the bottom side than on the top side in the majority of angular positions, as shown in Fig.4-9 (b) and Fig.4-10 (b), which consequently produces a negative lift force acting on the geometries, i.e. the negative Magnus effect.

Further insights into the boundary layer separations on the two different sides of the golf ball are provided in Fig.4-11, 4-12 and 4-13 by visualizing the three-dimensional flow structures around the golf ball respectively from the top view and bottom view at different Reynolds numbers. As clearly shown in Fig.4-11, in the subcritical regime, on both sides of the golf ball, the flow barely experiences any local oscillations as it traverses the dimples before full separation. In the supercritical regime, however, on both sides of the golf ball, there are visible local oscillations and small-scale vortices forming inside the dimples before the flow fully separates from the geometry surface. These behaviors are typical of the turbulent boundary layers for the supercritical golf ball case, as presented in Chapter 3. In addition, as shown in Fig.4-13, the higher relative Reynolds number on the bottom side gives rise to the local shear layer instability inside the dimples at positions further upstream than on the top side. In the critical regime, as shown in Fig.4-12, the flow behaviors on the top side are very similar to those of the subcritical boundary layer, while on the bottom side the local oscillations inside the dimples are clearly identified, as exhibited in the case of supercritical

boundary layer. These features further demonstrate the mechanism responsible for the negative Magnus effect.

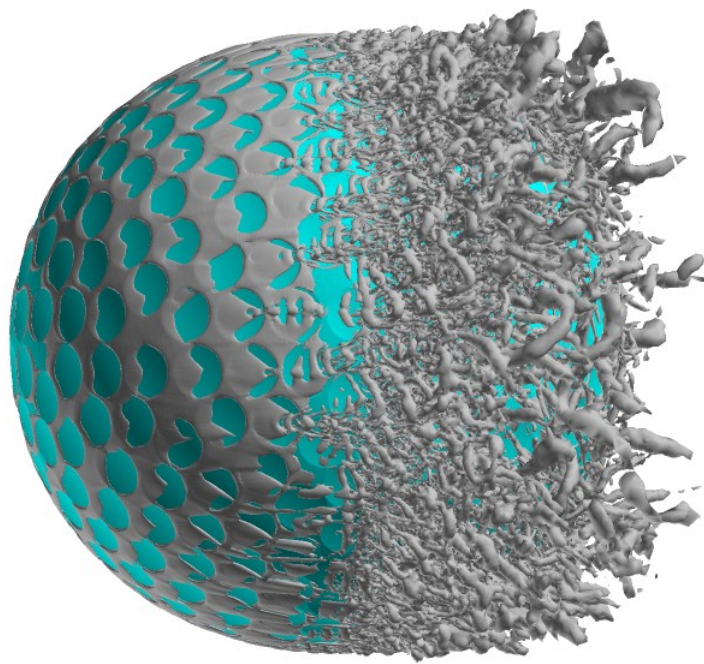


(a)

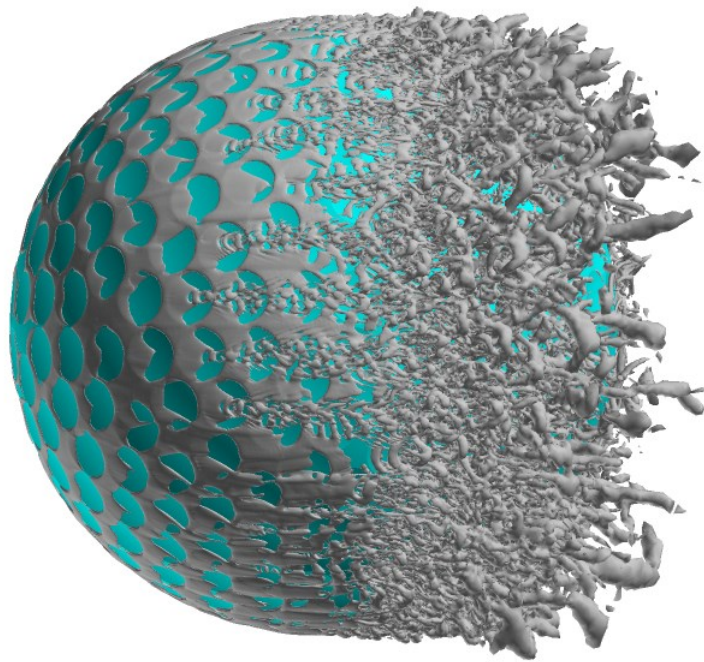


(b)

Fig.4-11 Visualization of the instantaneous vortical structures around the golf ball using ISO surface of Q respectively viewed from the: (a) top view; (b) bottom view; $Re=4.3 \times 10^4$, subcritical.

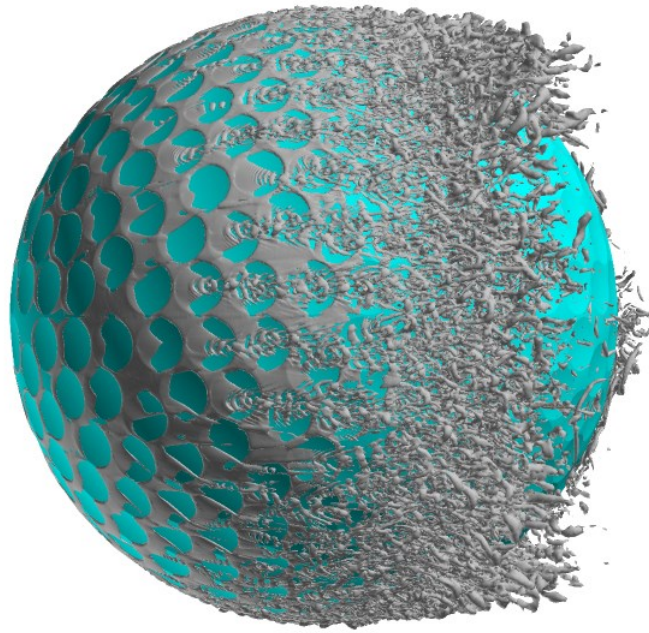


(a)

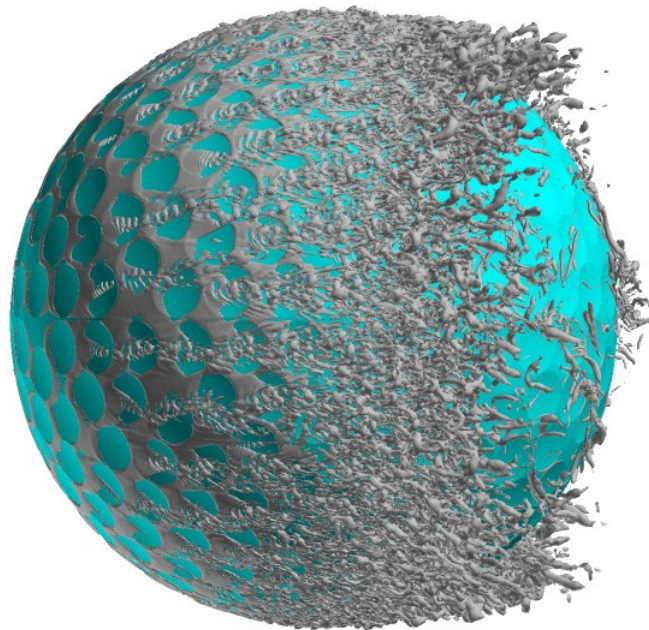


(b)

Fig.4-12 Visualization of the instantaneous vortical structures around the golf ball using ISO surface of Q respectively viewed from the: (a) top view; (b) bottom view; $Re=7.5 \times 10^4$, critical.



(a)



(b)

Fig.4-13 Visualization of the instantaneous vortical structures around the golf ball using ISO surface of Q respectively viewed from the: (a) top view; (b) bottom view; $Re=1.1 \times 10^5$, supercritical.

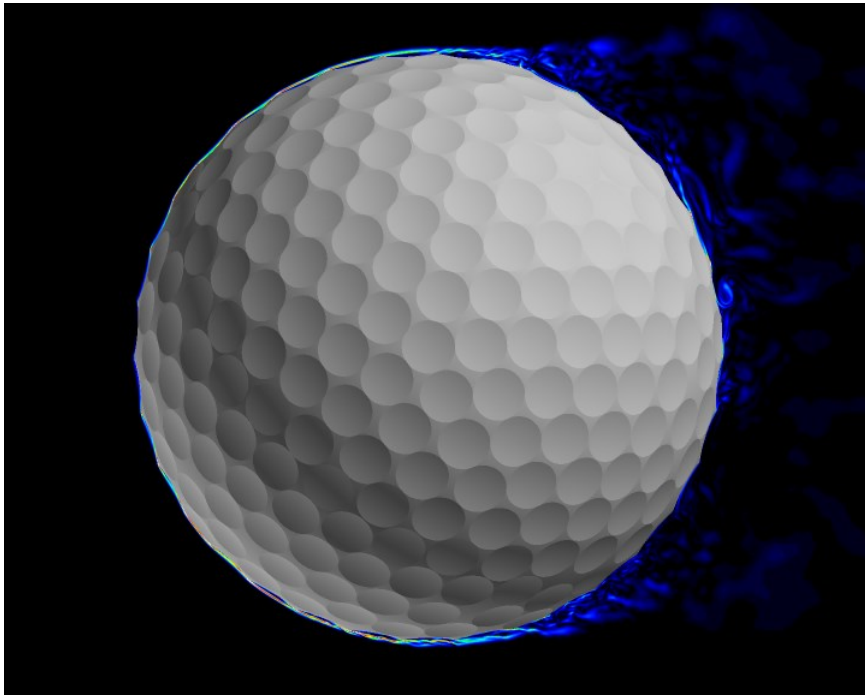


Fig.4-14 Contours of the instantaneous azimuthal vorticity viewed on the y_v plane at $Re=7.5\times 10^4$; $Ut/D=6.8$; the vorticity direction is out-of-plane.

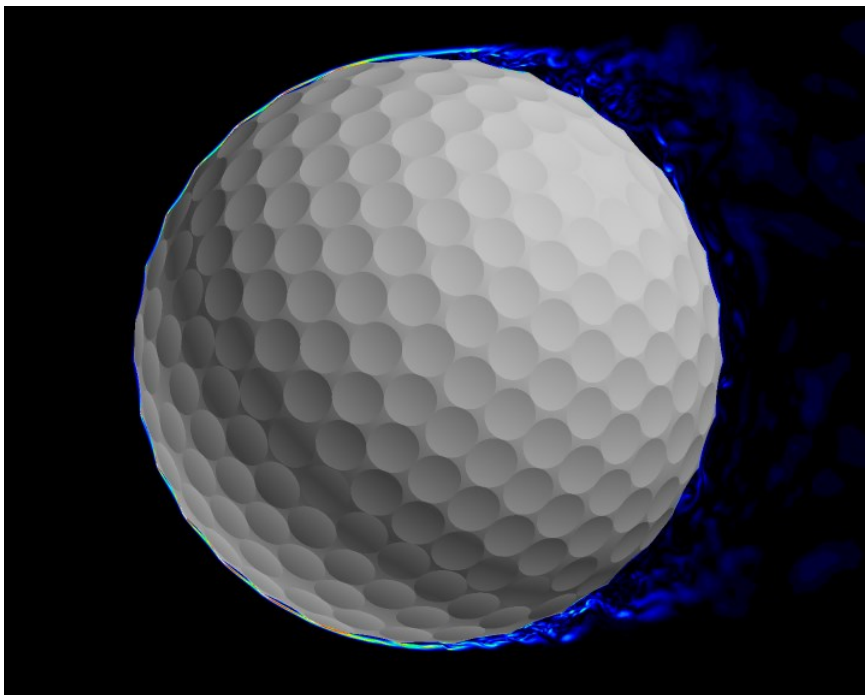


Fig.4-15 Contours of the instantaneous azimuthal vorticity viewed on the y_v plane at $Re=7.5\times 10^4$; $Ut/D=10.3$; the vorticity direction is out-of-plane.

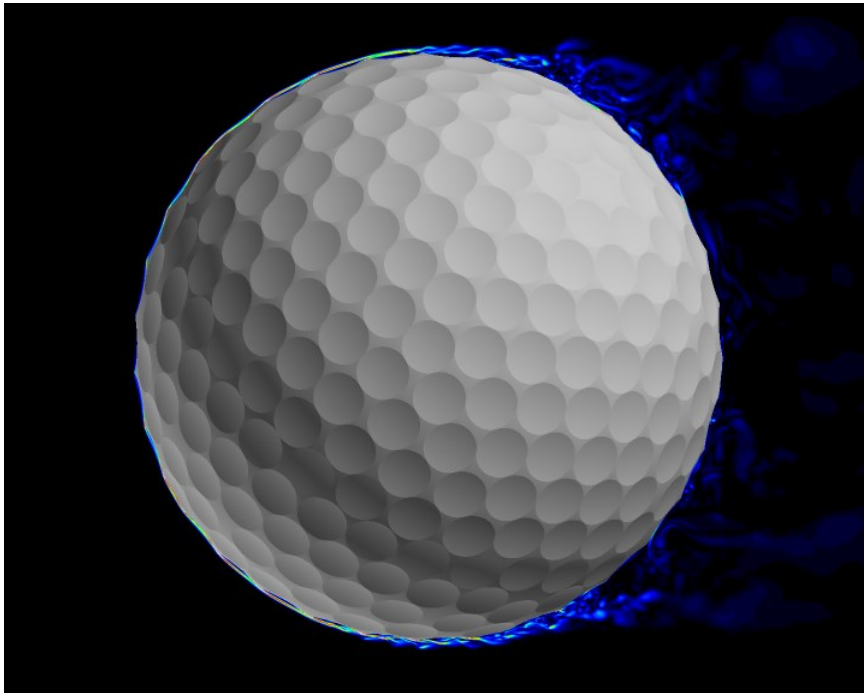


Fig.4-16 Contours of the instantaneous azimuthal vorticity viewed on the y_v plane at $Re=7.5 \times 10^4$; $Ut/D=13.8$; the vorticity direction is out-of-plane.

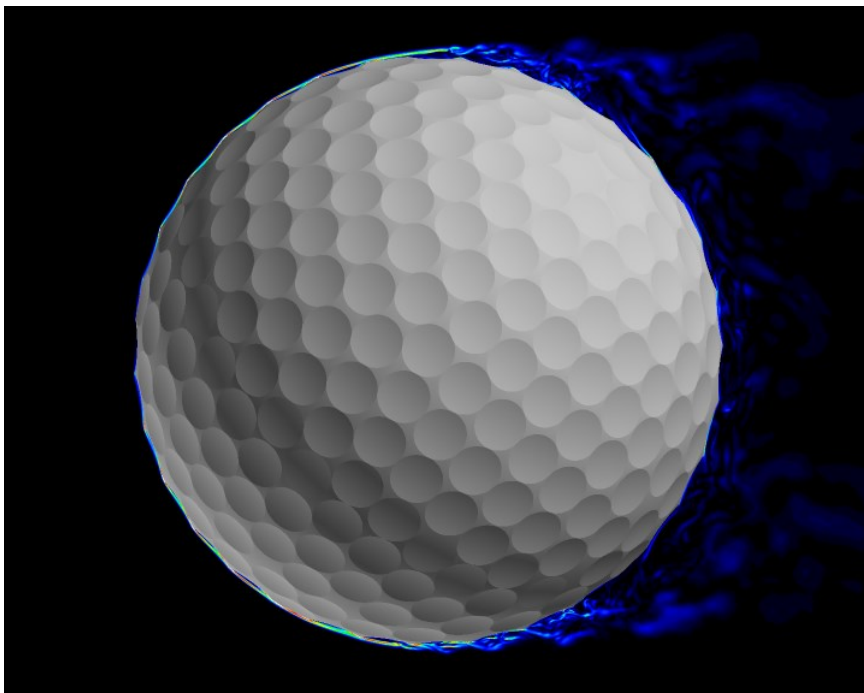


Fig.4-17 Contours of the instantaneous azimuthal vorticity viewed on the y_v plane at $Re=7.5 \times 10^4$; $Ut/D=17.3$; the vorticity direction is out-of-plane.

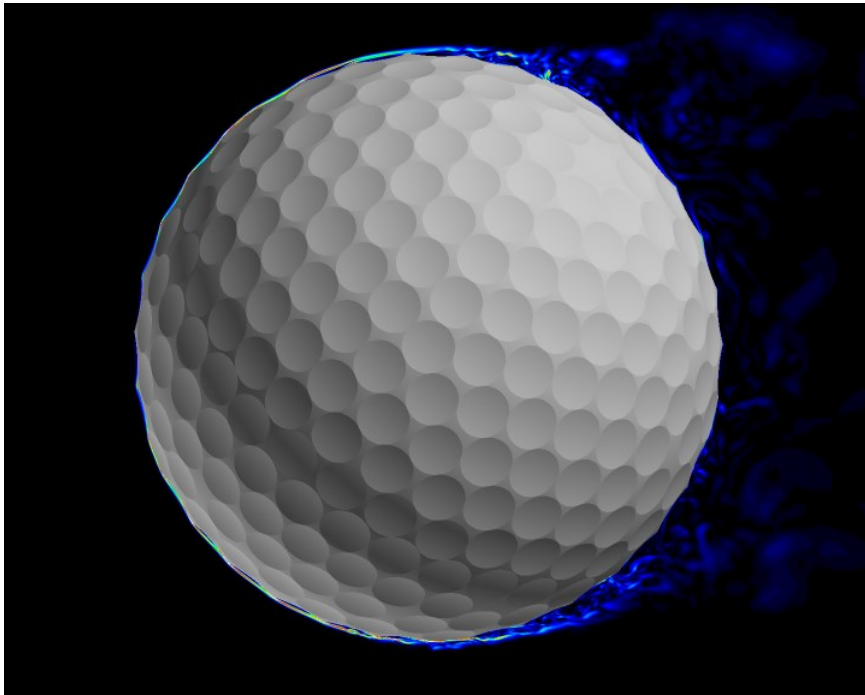


Fig.4-18 Contours of the instantaneous azimuthal vorticity viewed on the y_v plane at $Re=7.5\times 10^4$; $Ut/D=20.8$; the vorticity direction is out-of-plane.

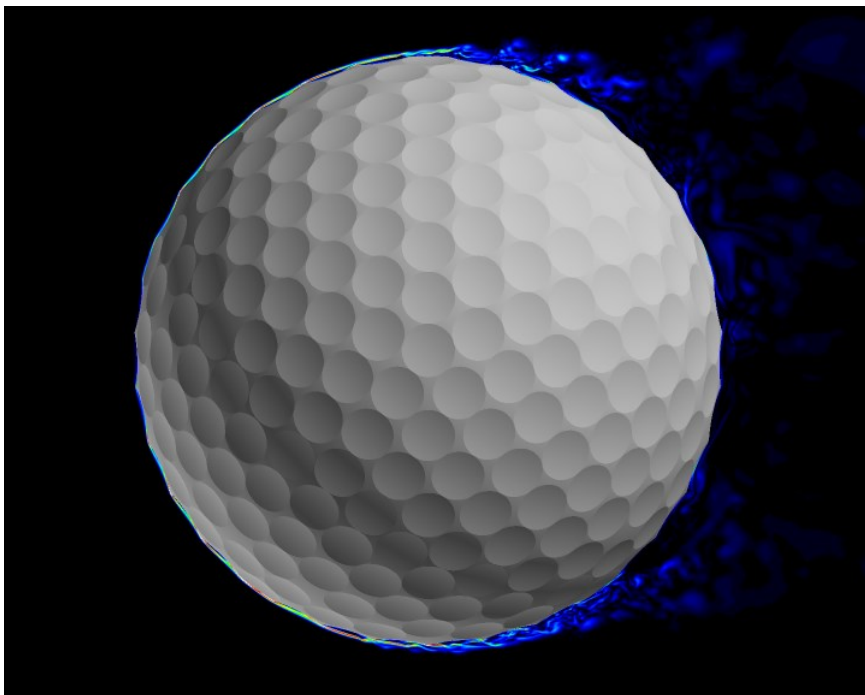


Fig.4-19 Contours of the instantaneous azimuthal vorticity viewed on the y_v plane at $Re=7.5\times 10^4$; $Ut/D=24.3$; the vorticity direction is out-of-plane.

Another issue of importance is that the separation points on both sides of the golf ball more or less shift as the dimple pattern changes with respect to the incoming flow direction due to the self-spinning motion. To identify these features, a time-dependent trace of the flow behaviors around the separation points on both sides of the golf ball in the critical regime is provided in Fig.4-14 to 4-19. As clearly shown in these figures, the separation points on both sides alter upstream/downstream with time, although not significantly. However, despite the shifting of the exact separation points, the boundary layers on the bottom side always become turbulent and separate at positions further downstream than on the top side. Actually, as shown in the time histories of the force evolution presented later in section 4.4, the lift forces are consistently positive/negative in the corresponding cases regardless of the dynamic change of the dimple patterns.

4.4 Development of the unsteady aerodynamic forces and wake flow structure

Table.4-1 Summary of the time-averaged mean value and standard deviation (s.d.) of the drag coefficient C_d , side force coefficient C_s , lift coefficient C_l , and the ratio of lift/drag for the self-spinning golf ball and smooth sphere, and the change of the drag coefficients in the rotating cases (C_d) relative to the stationary cases (C_{d_sta}).

		Golf Ball			Smooth Sphere		
		Re= 4.3×10^4 (subcritical)	Re= 7.5×10^4 (critical)	Re= 1.1×10^5 (supercritical)	Re= 1.0×10^4 (subcritical)	Re= 2.0×10^5 (critical)	Re= 1.14×10^6 (supercritical)
C_d	mean	0.5059	0.3168	0.2397	0.4635	0.2944	0.2229
	s.d.	0.0215	0.0116	0.0058	0.0107	0.0474	0.0176
C_s	mean	-0.0304	0.0386	-0.0211	0.0040	0.0524	0.0145
	s.d.	0.0243	0.0426	0.0262	0.0186	0.0352	0.0255
C_l	mean	0.1498	-0.1367	0.1353	0.0929	-0.2067	0.2128
	s.d.	0.0392	0.0414	0.0178	0.0266	0.0907	0.0220
C_l / C_d		0.2961	-0.4315	0.5646	0.2005	-0.7023	0.9549
$(C_d - C_{d_sta}) / C_{d_sta} [\%]$		3.8962	-18.9972	10.5440	4.1526	13.2262	25.2017

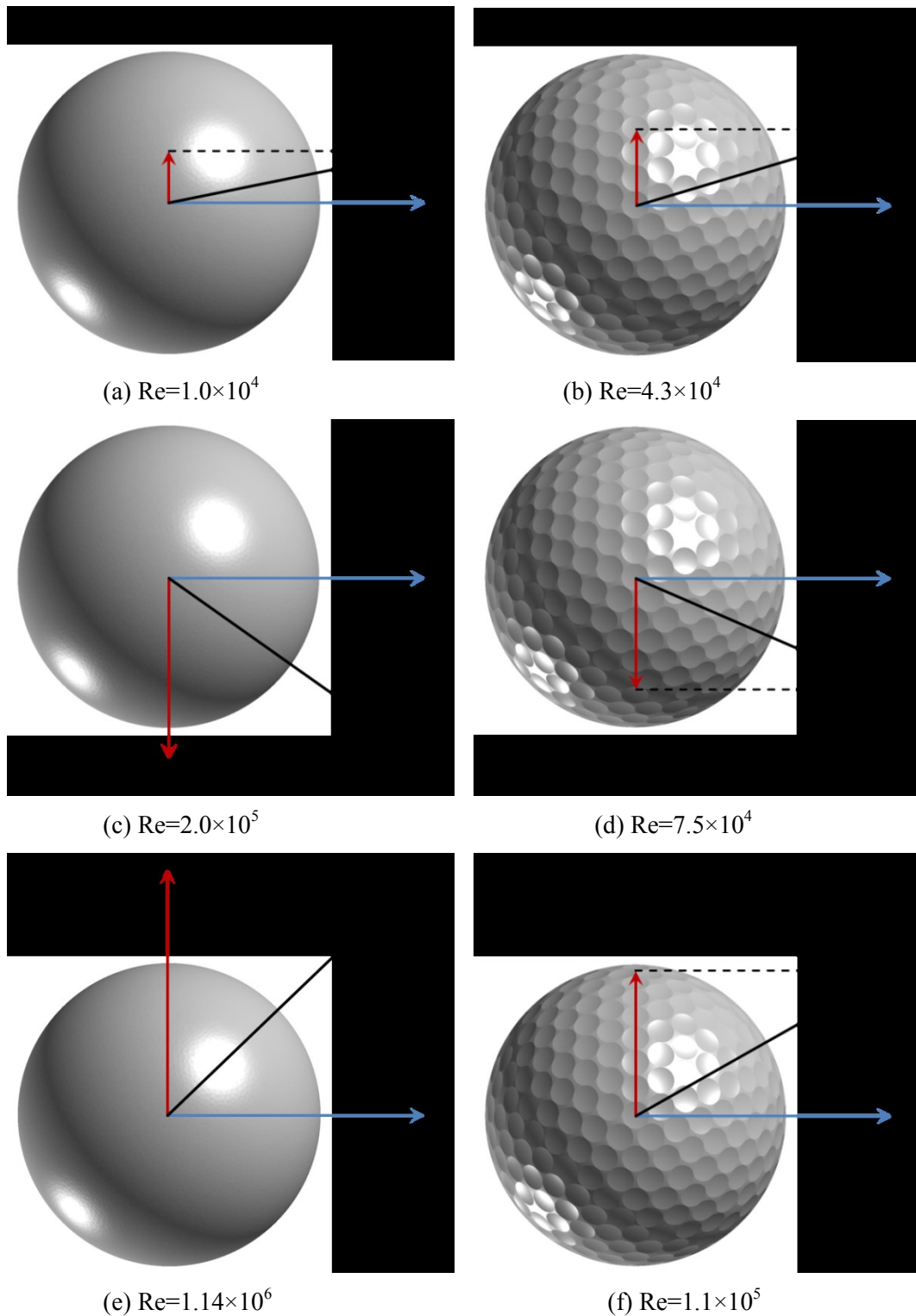


Fig.4-20 Schematic diagram of the time-averaged drag force, lift force and the corresponding resultant force in the drag-lift plane acting on the golf ball and smooth sphere; blue vector: drag force normalized by its magnitude, with unit length for all the cases; red vector: lift force normalized by the magnitude of drag force, with the length equaling C_l/C_d ; black vector: the resultant force of the drag and lift forces.

Table.4-1 summarizes the time-averaged values and the standard deviations of the drag, side force and lift force coefficients for the rotating golf ball and smooth sphere. The ratios of lift/drag in different rotating cases and the variations of the drag coefficients in the rotating cases relative to the corresponding stationary cases are also provided in this table. Fig.4-20 schematically illustrates the ratios of the time-averaged lift/drag and the corresponding resultant forces in the drag-lift plane acting on the golf ball and smooth sphere at different Reynolds numbers.

One thing interesting is, although the drag coefficients for both models decrease as the Reynolds number increases from the subcritical to supercritical regime, the magnitude of the lift coefficient decreases for the golf ball, whereas it increases for the smooth sphere. This further leads to some differences in the variation of C_l/C_d between these two models. As listed in Table.4-1, under the condition of the current spin parameter, the lift forces acting on both models in the subcritical regime are more than 70% smaller than the drag forces. As the Reynolds number increases to the critical and supercritical values, the ratio of C_l/C_d increases in terms of the magnitude for both models. However, compared to the smooth sphere, the increase in the ratio of C_l/C_d for the golf ball is less significant. In the supercritical regime, particularly, where the drag coefficients of both models stay close to each other, the lift force imposed on the smooth sphere has reached a value almost the same as the drag force, whereas the lift force acting on the golf ball remains at only about 56% of the drag force.

Another interesting issue is that, for both models, the standard deviations of the side force decrease in all the rotating cases when compared to the corresponding non-rotating cases, as revealed in Table.4-1 and Table.3-1. This indicates that the self-spinning motion generally makes the side force, which is in the direction perpendicular to the Magnus force, somewhat more stable.

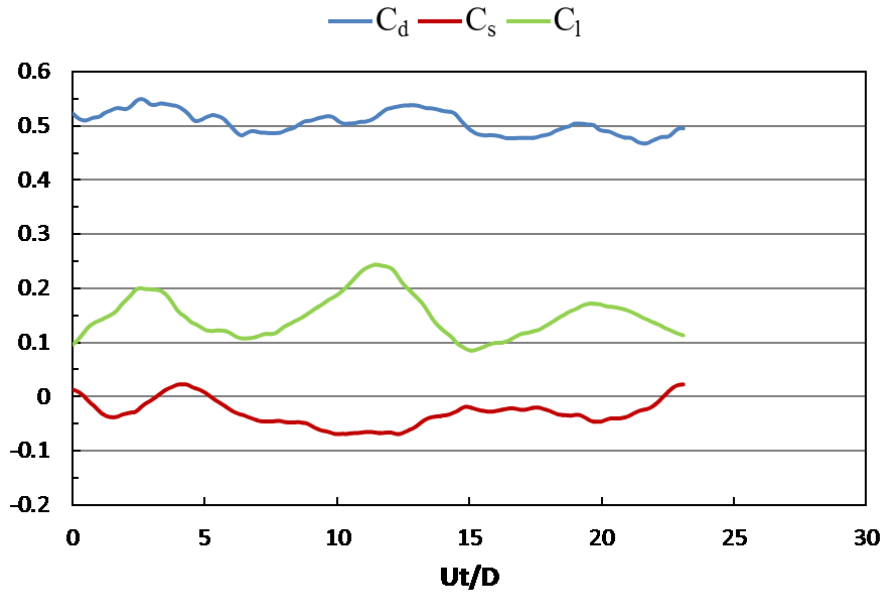
4.4.1 Transient lateral force and wake flow structure in the subcritical regime

Fig.4-21 and Fig.4-22 show the time histories of the development of the drag, side force and lift coefficients in the subcritical Reynolds number regime for the self-spinning golf ball and smooth sphere respectively. As revealed in the figures of the temporal evolution, the positive lift forces are continuously imposed on both models as a consequence of the rotating motion during the whole time intervals. This makes the variation of the resultant lateral force somewhat more regular in the rotating cases when compared to the stationary cases. As indicated in Fig.4-21 (b) and Fig.4-22 (b), the curves representing the rotating cases are more concentrated, and the main areas of the lateral force oscillation shift slightly upwards. In

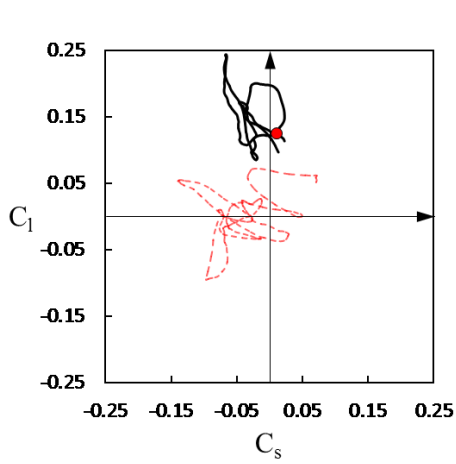
addition, one can observe from the phase diagrams that, for both rotating models, the oscillation of the resultant lateral force is more dominant in the lift force direction than in the side force direction. This feature is also quantitatively evidenced by the larger standard deviations of the lift forces of both models, when compared to the side forces, as listed in Table.4-1.

Compared with the rotating smooth sphere, the lift force acting on the rotating golf ball exhibits a larger magnitude and oscillation, as evidenced by the corresponding statistics listed in Table.4-1, and the obviously less concentrated curve shown in Fig.4-21 (b). This is similar to the stationary cases in the same regime. Additionally, it is interesting to note that a somewhat visible side force is acting on the rotating golf ball even in the sense of the time-averaged value, which is one order of magnitude smaller than the lift force acting on the golf ball, whereas the side force acting on the rotating smooth sphere is much closer to zero. This is probably due to the asymmetric dimple distribution with respect to the x-z plane of the golf ball, as presented in section 2.6, Chapter 2.

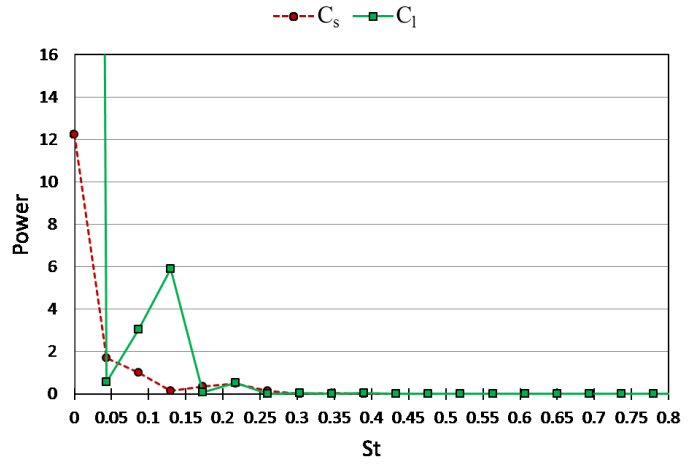
Respectively shown in Fig.4-21 (c) and Fig.4-22 (c) are the power spectra of the side force and lift coefficients for the rotating golf ball and smooth sphere at the subcritical Reynolds numbers. As clearly indicated in Fig.4-22 (c), under the condition of the present spin parameter, two peaks appear at different Strouhal numbers for the rotating smooth sphere, which is qualitatively the same as for the stationary smooth sphere. However, the second Strouhal number corresponding to the large-scale wake instability is shifted to a slightly higher value in the self-spinning case when compared to the stationary case. This might suggest a somewhat enhanced lift force oscillation for the smooth sphere due to the rotating motion. In contrast, as revealed in Fig.4-21 (c), only one dominant frequency appears in the power spectra for the rotating golf ball, which is visibly different from the case of the stationary golf ball. In addition, the Strouhal number corresponding to the lift force oscillation is somewhat shifted to a lower value in the self-spinning case when compared to the stationary case. This probably is associated with the periodic change of the dimple pattern with respect to the incoming flow direction while the golf ball is rotating.



(a)

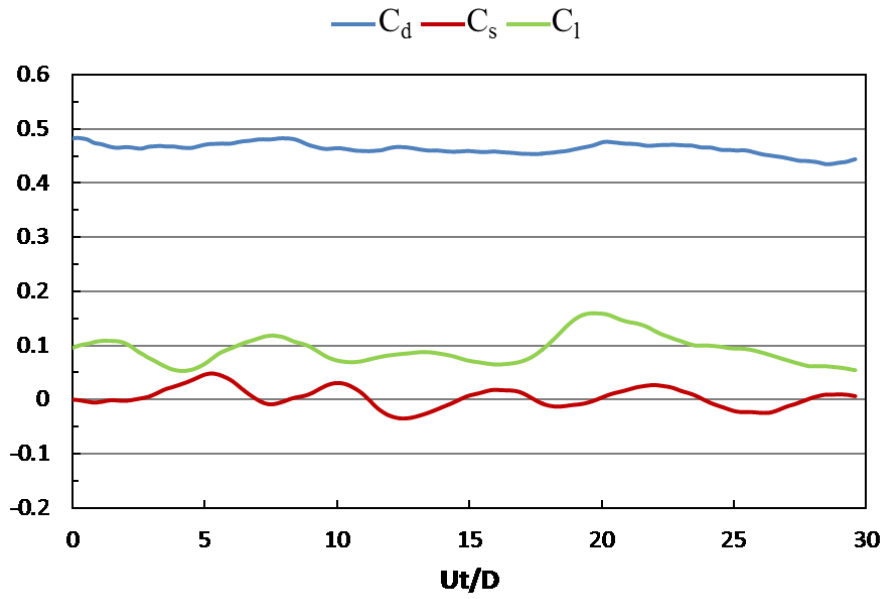


(b)

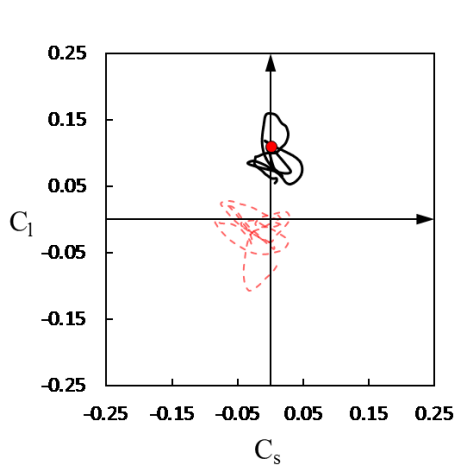


(c)

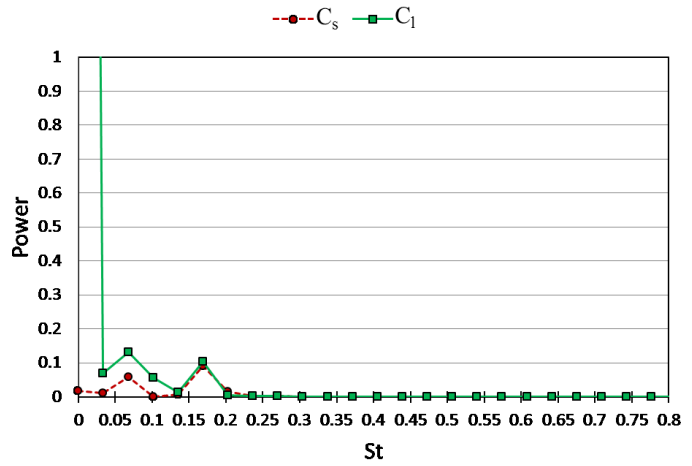
Fig.4-21 Time series of the drag, side force and lift coefficients for the self-spinning golf ball at subcritical $Re=4.3 \times 10^4$ after the flow reached a statistically steady state: (a) temporal evolution of the drag coefficient C_d , side force coefficient C_s and lift coefficient C_l ; (b) phase diagram of C_s and C_l , the red point represents the resultant lateral force at the non-dimensional moment indicated in Fig.4-23; the red dash line represents the corresponding variation in the stationary golf ball case at the same Reynolds number; (c) power spectrum of the side force coefficient C_s and lift coefficient C_l .



(a)



(b)



(c)

Fig.4-22 Time series of the drag, side force and lift coefficients for the self-spinning smooth sphere at subcritical $Re=1.0 \times 10^4$ after the flow reached a statistically steady state: (a) temporal evolution of the drag coefficient C_d , side force coefficient C_s and lift coefficient C_l ; (b) phase diagram of C_s and C_l , the red point represents the resultant lateral force at the non-dimensional moment indicated in Fig.4-24; the red dash line represents the corresponding variation in the stationary smooth sphere case at the same Reynolds number; (c) power spectrum of the side force coefficient C_s and lift coefficient C_l .

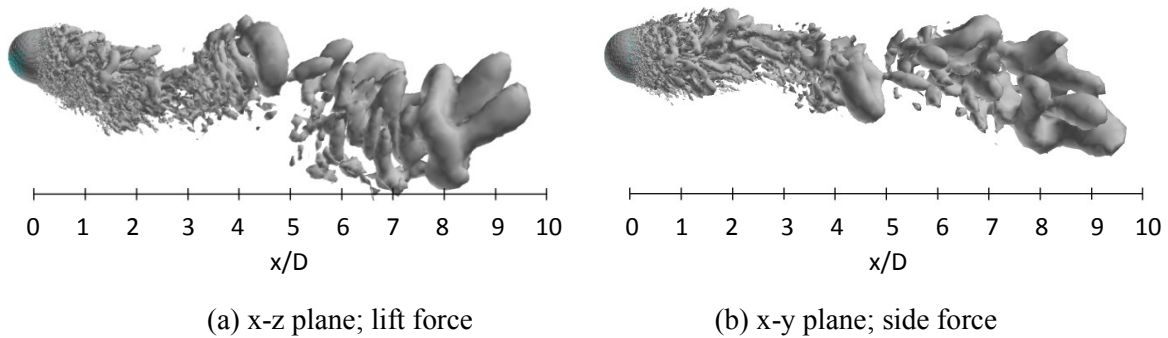


Fig.4-23 Visualization of the instantaneous vortical structures in the wake area of the self-spinning golf ball at $Re=4.3\times 10^4$ using ISO surface of Q ($Ut/D=4.9$, the resultant lateral force at this moment is indicated in Fig.4-21 (b) by the red point).

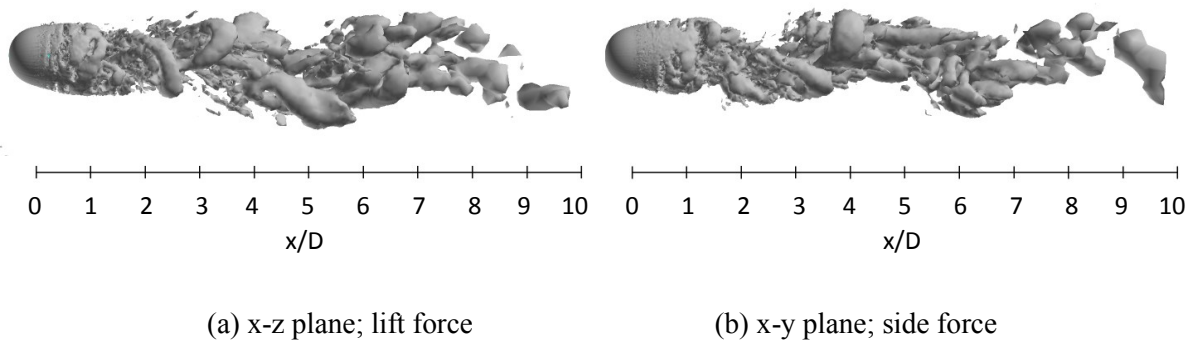


Fig.4-24 Visualization of the instantaneous vortical structures in the wake area of the self-spinning smooth sphere at $Re=1.0\times 10^4$ using ISO surface of Q ($Ut/D=21.5$, the resultant lateral force at this moment is indicated in Fig.4-22 (b) by the red point).

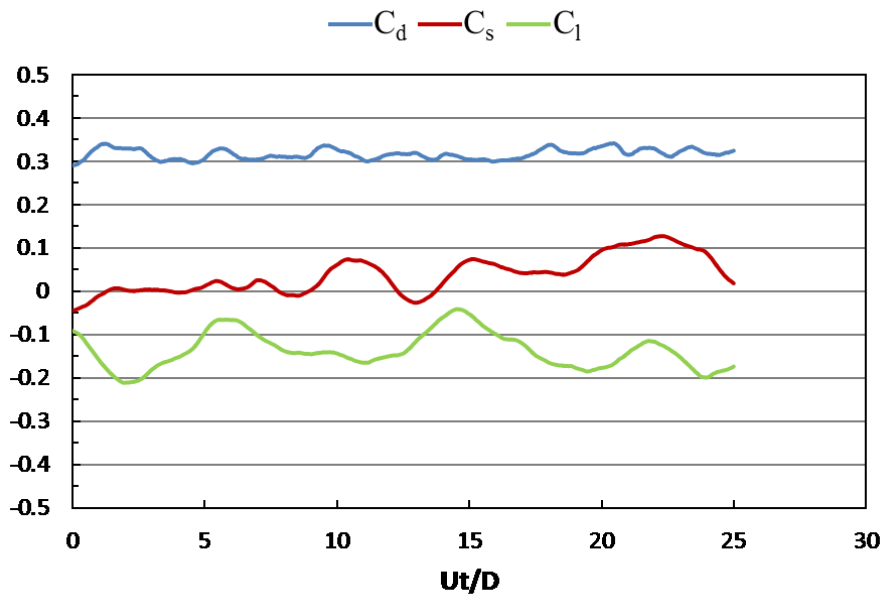
Fig.4-23 and Fig.4-24 respectively show the instantaneous vortical structures in the wake areas of the rotating golf ball and smooth sphere at the subcritical Reynolds numbers. Visualizations were obtained in both the lift force plane and side force plane. As also evidenced in section 4.2, the flow structures in the near-wall wake areas of both rotating models are deflected downwards in their lift force planes, especially for the golf ball, which has the lift force with a larger magnitude. It is also interesting to note that the wake flow structure behind the golf ball is also somewhat tilted in the side force plane, whereas the one behind the smooth sphere is much less deflected in the corresponding plane. This relates to the difference in the oscillation of the side forces acting on the two models, as mentioned above. Similar to the stationary cases in the subcritical regime, a large-scale wave motion is also pronounced in the wake areas of both rotating models, and the hairpin structures become distinct as the flow travels some distance further downstream after the full separation.

Relating to the dominant Strouhal numbers, the wavelength of the wake flow structure behind the golf ball spans about 7~8D, as indicated in Fig.4-23 (a), whereas the wavelength of the wake flow structure behind the smooth sphere stays around 6D, as indicated in Fig.4-24 (a).

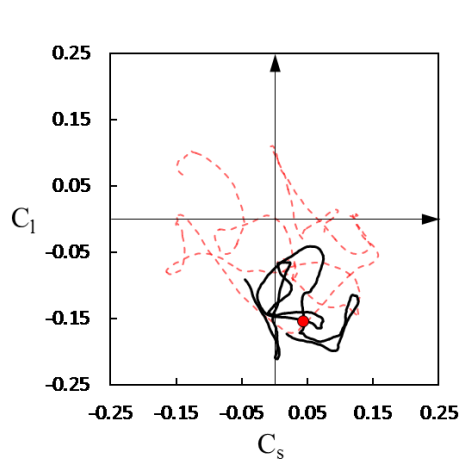
4.4.2 Transient lateral force and wake flow structure in the critical regime

Fig.4-25 and Fig.4-26 show the time histories of the development of the drag, side force and lift coefficients in the critical Reynolds number regime for the self-spinning golf ball and smooth sphere respectively. As revealed in the figures of the temporal evolution, the negative lift forces are continuously imposed on both rotating models during the whole time intervals. This leads to a visible downward-shifting of the mean positions of the lateral force oscillation in the phase diagrams of both models. Compared with the corresponding stationary case in the same regime, the oscillation of the lateral force acting on the rotating golf ball is remarkably smaller in both the lift and side force directions, as evidenced by its reduced standard deviations of both the lift and side force coefficients, as presented in Table.4-1 and Table.3-1, and the obviously more restricted area of the lateral force oscillation shown in Fig.4-25 (b). In contrast, the lateral force acting on the rotating smooth sphere, interestingly, experiences a considerably larger oscillation in the lift force direction when compared to the stationary sphere, as shown in Fig.4-26 (b). In addition, the standard deviation of the lift force in the rotating case is more than twice as large as that in the stationary case, as presented in Table.4-1 and Table.3-1. However, the lateral force indeed becomes more stable in the side force direction for the rotating smooth sphere. The different lateral force variations may further explain the difference in the shifting of the drag coefficient between the rotating golf ball and the rotating smooth sphere in the critical regime. As provided in Table.4-1 and Fig.4-1, the drag force acting on the rotating golf ball decreases by about 19% when compared to the stationary golf ball, whereas the drag force acting on the rotating smooth sphere is more than 13% larger than the stationary sphere, and has the largest standard deviation of drag coefficient among all the self-spinning cases.

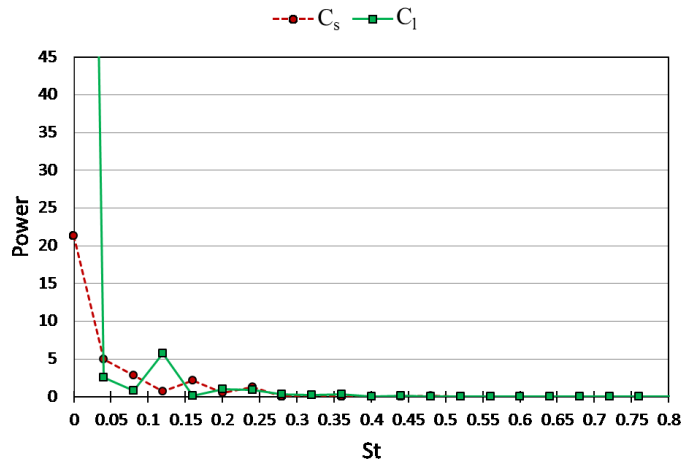
In addition, as presented in Table.4-1, there are visible side forces acting on both models in the critical regime even in the sense of the time-averaged value. Similar features were also obtained in the experimental measurements of the flow past rotating smooth spheres by Kray et al.¹⁹. This may imply that the negative Magnus effect exhibits somewhat three-dimensional characteristics. For the golf ball, particularly, the side force may result from an integrated effect of the negative Magnus effect and asymmetric dimple distribution.



(a)



(b)



(c)

Fig.4-25 Time series of the drag, side force and lift coefficients for the self-spinning golf ball at critical $Re=7.5 \times 10^4$ after the flow reached a statistically steady state: (a) temporal evolution of the drag coefficient C_d , side force coefficient C_s and lift coefficient C_l ; (b) phase diagram of C_s and C_l , the red point represents the resultant lateral force at the non-dimensional moment indicated in Fig.4-27; the red dash line represents the corresponding variation in the stationary golf ball case at the same Reynolds number; (c) power spectrum of the side force coefficient C_s and lift coefficient C_l .

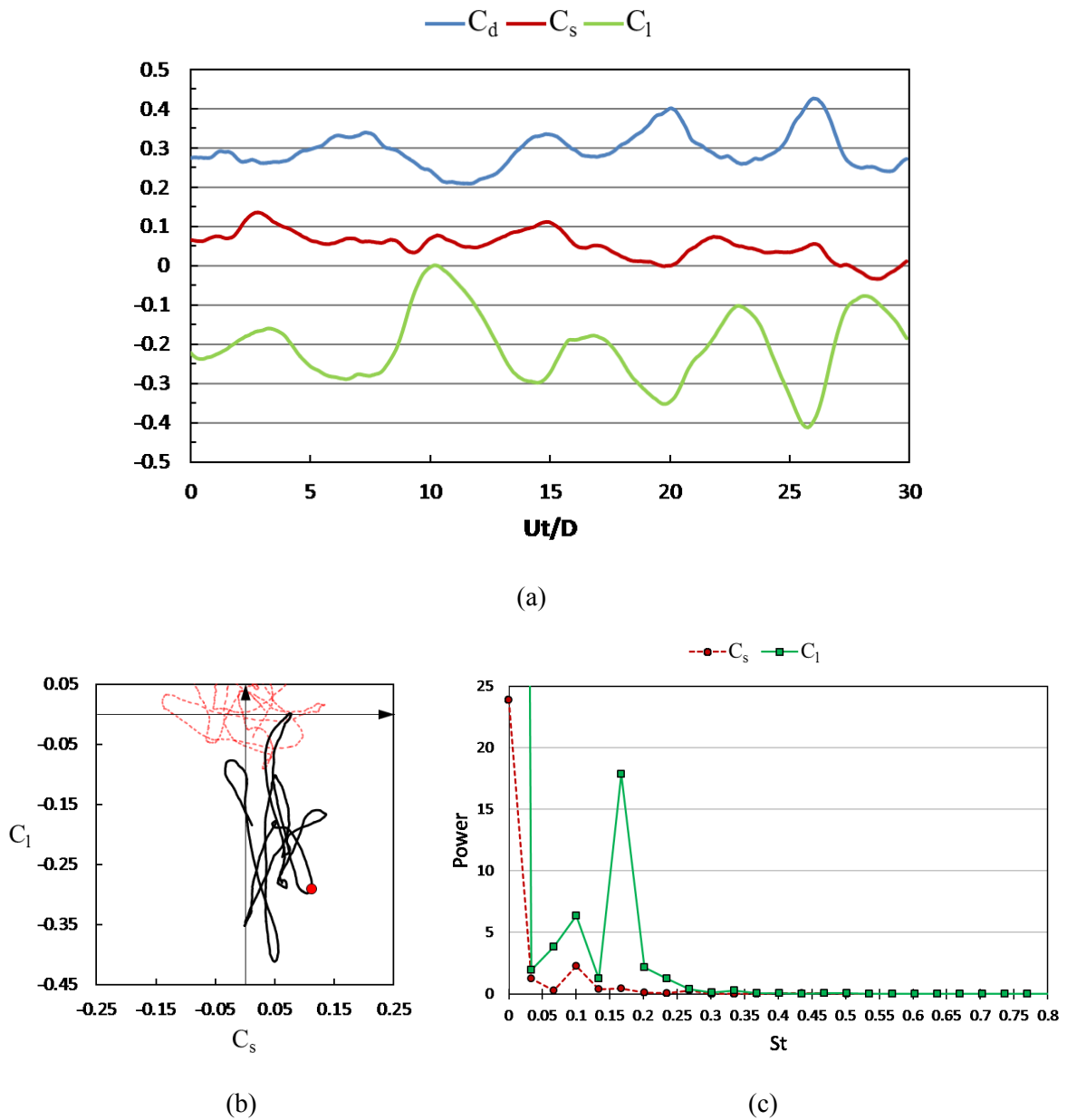


Fig.4-26 Time series of the drag, side force and lift coefficients for the self-spinning smooth sphere at critical $Re=2.0 \times 10^5$ after the flow reached a statistically steady state: (a) temporal evolution of the drag coefficient C_d , side force coefficient C_s and lift coefficient C_l ; (b) phase diagram of C_s and C_l , the red point represents the resultant lateral force at the non-dimensional moment indicated in Fig.4-28; the red dash line represents the corresponding variation in the stationary smooth sphere case at the same Reynolds number; (c) power spectrum of the side force coefficient C_s and lift coefficient C_l .

Respectively shown in Fig.4-25 (c) and Fig.4-26 (c) are the power spectra of the side force and lift coefficients for the rotating golf ball and smooth sphere at the critical Reynolds numbers. It is interesting to note that for both rotating models in the critical regime, the shifting of the dominant frequency shows a trend very similar to that exhibited in the subcritical regime. For the smooth sphere, as revealed in Fig.4-26 (c), the dominant frequency that corresponds to the large-scale wake instability is slightly shifted to a higher value in the rotating case when compared to the stationary case in the same regime, and the shifted Strouhal number stays very close to the one obtained in the subcritical rotating sphere case. For the golf ball, as revealed in Fig.4-25 (c), the dominant frequency of the lift force is shifted to a lower value in the rotating case when compared to the stationary case in the same regime, and the shifted Strouhal number is similar to the one obtained in the subcritical rotating golf ball case. However, the low dominant frequency of the side force exhibited in the stationary golf ball case disappears in the rotating case. This may be because the side force is in the direction perpendicular to the Magnus force so that its oscillation has less power.

Fig.4-27 and Fig.4-28 respectively show the instantaneous vortical structures in the wake areas of the rotating golf ball and smooth sphere at the critical Reynolds numbers. Visualizations were obtained in both the lift force plane and side force plane. As clearly shown in the figures, the flow structures in the near-wall wake areas of both rotating models are tilted upwards in their lift force planes, especially for the smooth sphere, which has the negative lift force with a larger magnitude. In addition, one can observe that the wake flow structures behind both models are somewhat deflected in their side force planes, corresponding to the visible side forces acting on the geometries. Similar to the stationary cases in the critical regime, a large-scale wave motion and the shedding of hairpin structures are also pronounced in the wake areas of both rotating models, although the waviness behind the smooth sphere is more aggressive due to its larger oscillation of the lift force. Relating to the dominant Strouhal number, the wavelength of the wake flow structure behind the golf ball spans around $8D$, as indicated in Fig.4-27 (a), whereas the wavelength of the wake flow structure behind the smooth sphere remains about $6D$, as indicated in Fig.4-28 (a).

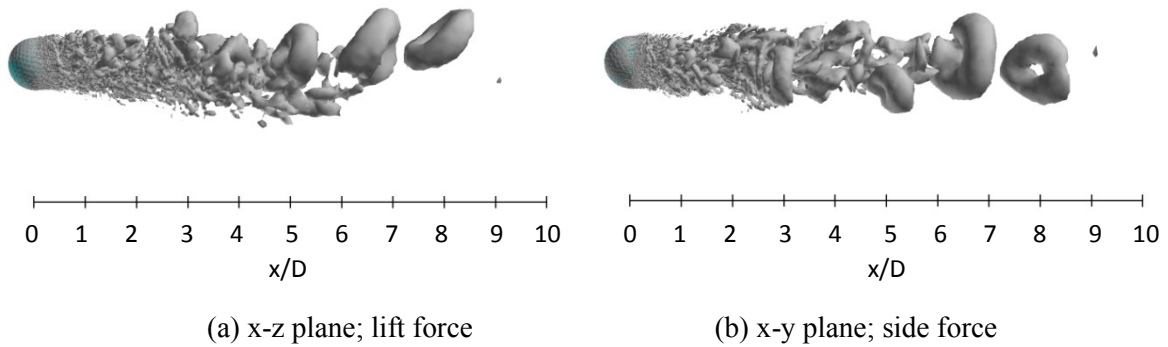


Fig.4-27 Visualization of the instantaneous vortical structures in the wake area of the self-spinning golf ball at $Re=7.5 \times 10^4$ using ISO surface of Q ($Ut/D=11.7$, the resultant lateral force at this moment is indicated in Fig.4-25 (b) by the red point).

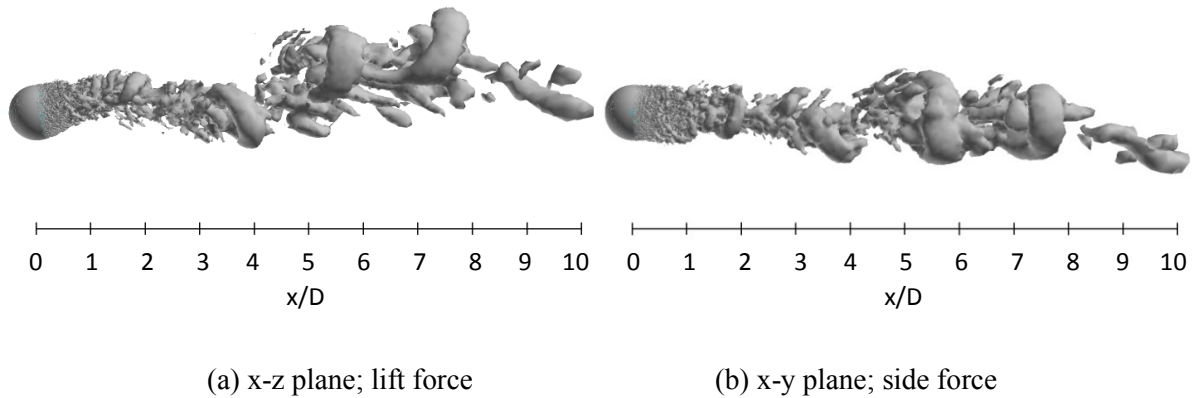


Fig.4-28 Visualization of the instantaneous vortical structures in the wake area of the self-spinning smooth sphere at $Re=2.0 \times 10^5$ using ISO surface of Q ($Ut/D=14.7$, the resultant lateral force at this moment is indicated in Fig.4-26 (b) by the red point).

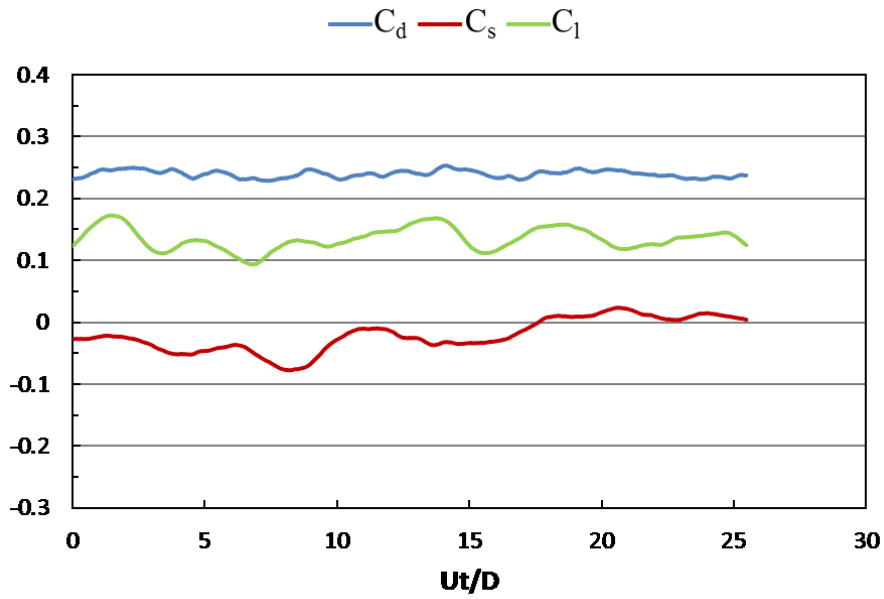
4.4.3 Transient lateral force and wake flow structure in the supercritical regime

Fig.4-29 and Fig.4-30 show the time histories of the development of the drag, side force and lift coefficients in the supercritical Reynolds number regime for the self-spinning golf ball and smooth sphere respectively. As revealed in the figures of the temporal evolution, the positive lift forces are continuously imposed on both rotating models during the whole time intervals. This, similar to the subcritical cases, makes the main areas of the lateral force oscillation shift upwards and become more concentrated in the phase diagrams of both models. Compared with the stationary cases in the same regime, the standard deviations of both the lift and side forces are considerably smaller in the rotating cases for both models, as presented in Table.4-1 and Table.3-1. In addition, as clearly shown in Fig.4-29 (b) and Fig.4-30 (b), the rotation trend of the shifting of lateral force direction that is clearly observed in the

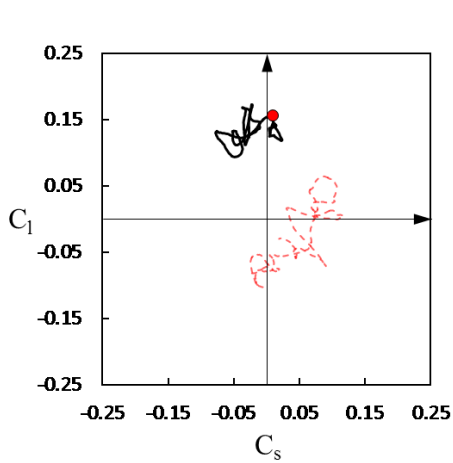
stationary cases disappears in both rotating cases. These features clearly reveal that the self-spinning motion helps to stabilize the lateral forces in terms of both the oscillation and the direction for both models in the supercritical regime. This is probably because the self-spinning motion results in a smaller fluctuation of the momentum in the turbulent boundary layers and consequently leads to less shifting of the positions of flow separation.

It is also interesting to note that the lift force acting on the rotating golf ball is about 40% smaller in terms of the magnitude and about 20% smaller in terms of the standard deviation when compared to the rotating smooth sphere, while the drag forces acting on these two models are similar to each other. These discrepancies further reveal the suppression of the lift force acting on the rotating golf ball when compared to the rotating smooth sphere, which is analogous to the stationary cases in the supercritical regime. In addition, as revealed by the more biased curve pattern shown in Fig.4-29 (b) and the corresponding statistics listed in Table.4-1, a larger mean side force is acting on the rotating golf ball when compared to the rotating smooth sphere, which is one order of magnitude smaller than the lift force. This is most likely due to the asymmetric dimple distribution on the golf ball surface, as also evidenced in the rotating golf ball case at the subcritical Reynolds number.

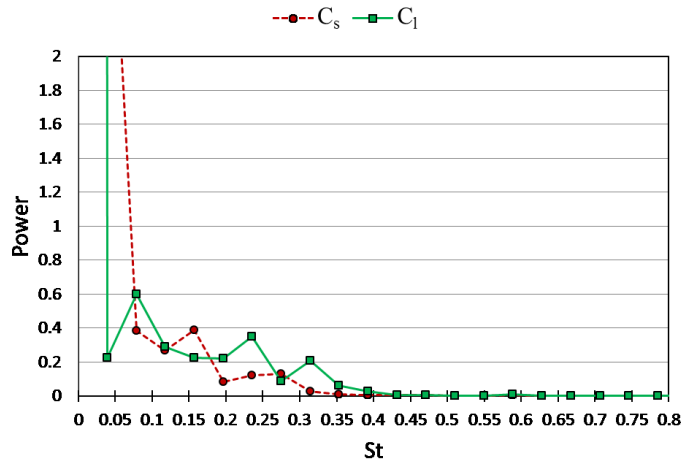
Respectively shown in Fig.4-29 (c) and Fig.4-30 (c) are the power spectra of the side force and lift coefficients for the rotating golf ball and smooth sphere at the supercritical Reynolds numbers. As indicated in the figures, the power spectra of both models remain broadband in the self-spinning cases. For the smooth sphere, the dominant frequency that is associated with the large-scale wake instability is shifted to a higher value in the rotating case when compared to the stationary case in the same regime. This change is similar to those obtained in the rotating cases at the subcritical and critical Reynolds numbers. For the golf ball, however, the dominant frequency that appears in the stationary case is no longer distinct when the self-spinning motion is imposed on the geometry. This is probably associated with the suppression of the lift force acting on the rotating golf ball.



(a)

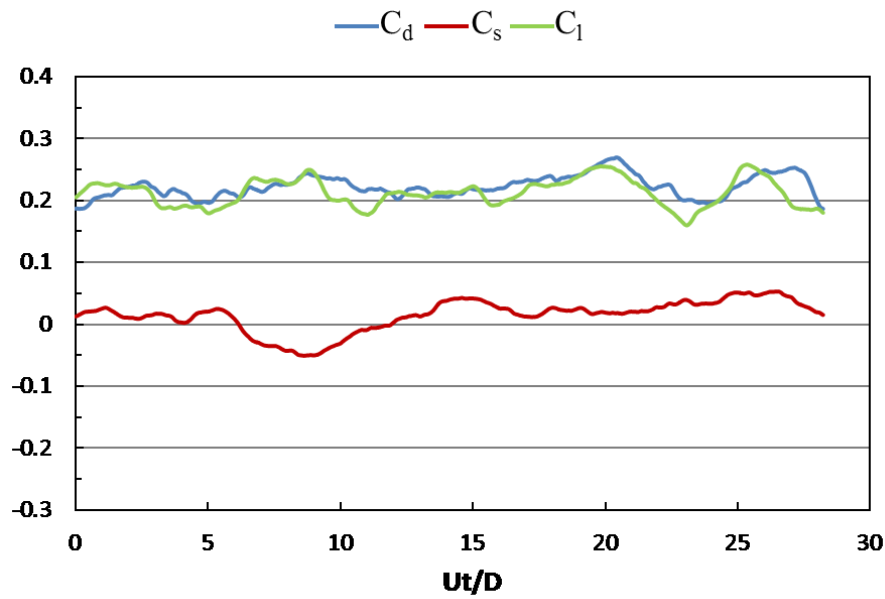


(b)

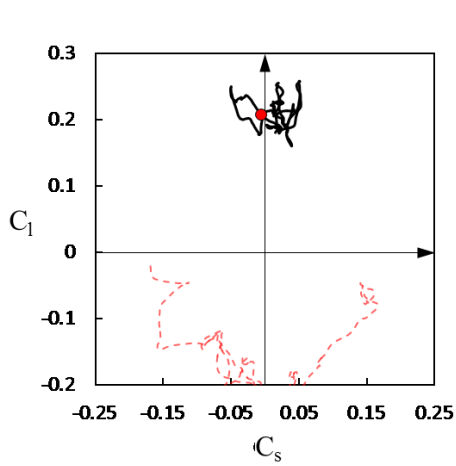


(c)

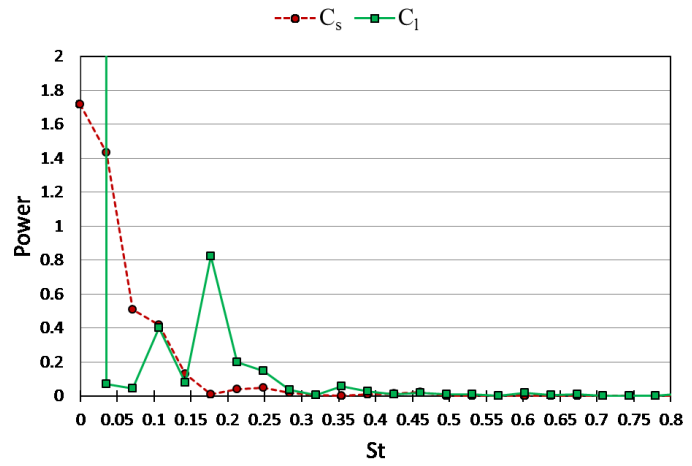
Fig.4-29 Time series of the drag, side force and lift coefficients for the self-spinning golf ball at supercritical $Re=1.1 \times 10^5$ after the flow reached a statistically steady state: (a) temporal evolution of the drag coefficient C_d , side force coefficient C_s and lift coefficient C_l ; (b) phase diagram of C_s and C_l , the red point represents the resultant lateral force at the non-dimensional moment indicated in Fig.4-31; the red dash line represents the corresponding variation in the stationary golf ball case at the same Reynolds number; (c) power spectrum of the side force coefficient C_s and lift coefficient C_l .



(a)



(b)



(c)

Fig.4-30 Time series of the drag, side force and lift coefficients for the self-spinning smooth sphere at supercritical $Re=1.14 \times 10^6$ after the flow reached a statistically steady state: (a) temporal evolution of the drag coefficient C_d , side force coefficient C_s and lift coefficient C_l ; (b) phase diagram of C_s and C_l , the red point represents the resultant lateral force at the non-dimensional moment indicated in Fig.4-32; the red dash line represents the corresponding variation in the stationary smooth sphere case at the same Reynolds number; (c) power spectrum of the side force coefficient C_s and lift coefficient C_l .

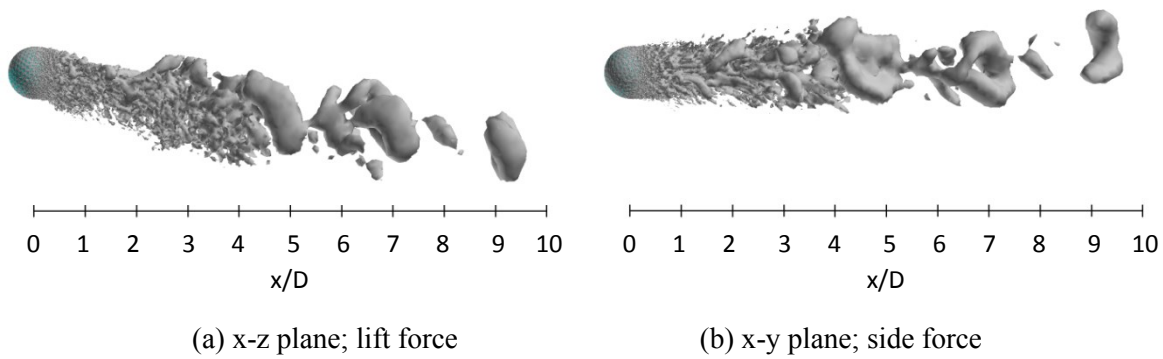


Fig.4-31 Visualization of the instantaneous vortical structures in the wake area of the self-spinning golf ball at $Re=1.1\times 10^5$ using ISO surface of Q ($Ut/D=18.8$, the resultant lateral force at this moment is indicated in Fig.4-29 (b) by the red point).

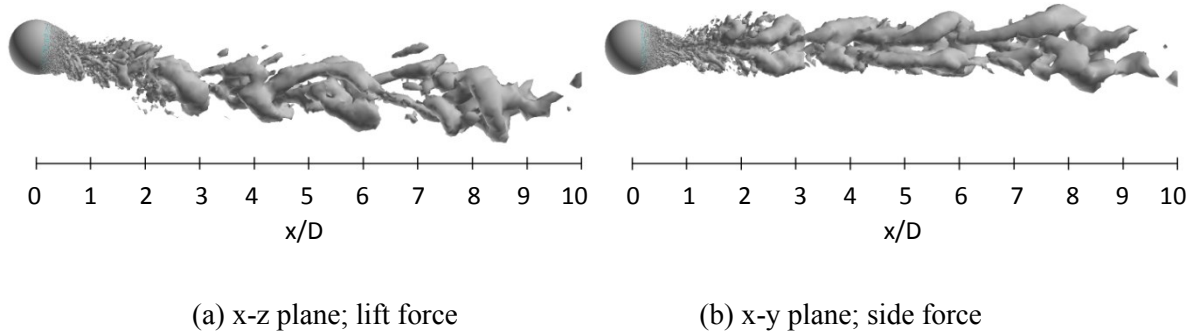


Fig.4-32 Visualization of the instantaneous vortical structures in the wake area of the self-spinning smooth sphere at $Re=1.14\times 10^6$ using ISO surface of Q ($Ut/D=6.2$, the resultant lateral force at this moment is indicated in Fig.4-30 (b) by the red point).

Fig.4-31 and Fig.4-32 respectively show the instantaneous vortical structures in the wake areas of the rotating golf ball and smooth sphere at the supercritical Reynolds numbers. Visualizations were obtained in both the lift force plane and side force plane. Analogous to the stationary cases in the same regime, a large-scale vortex shedding is pronounced in the wake flow of both rotating models. However, the progressive wave motion that is distinctly exhibited in the subcritical and critical cases is no longer clearly observed in the supercritical regime. As shown in Fig.4-31 (a) and Fig.4-32 (a), the wake structures behind both rotating models are remarkably deflected downwards in their lift force planes, corresponding to the positive lift forces generated in this regime. In the side force plane, however, the wake structure behind the golf ball is tilted slightly upwards, whereas the one behind the smooth sphere stays almost parallel to the streamwise axis that goes across the center of the sphere (x

axis), as indicated in Fig.4-31 (b) and Fig.4-32 (b), which directly relates to the difference in the side forces acting on these two models.

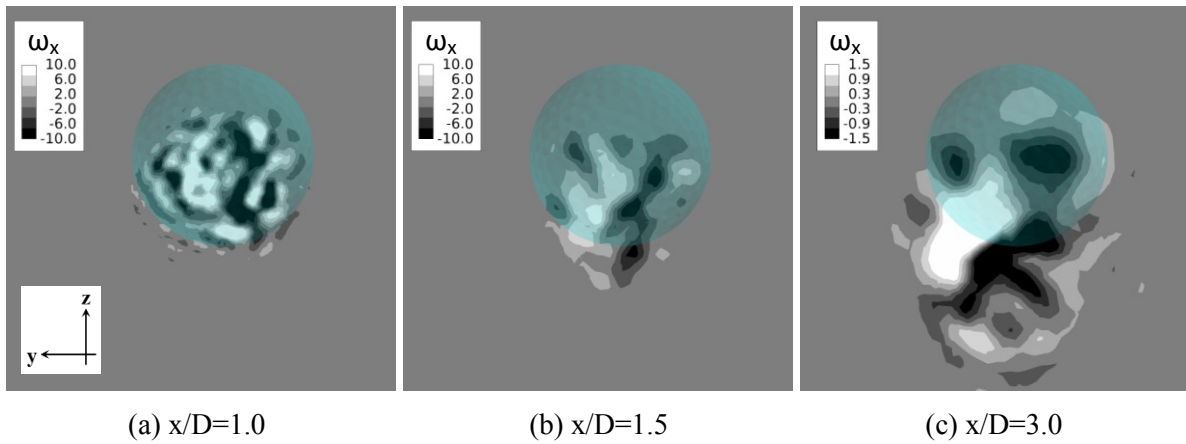


Fig.4-33 Streamwise vorticity component in the wake flow of the self-spinning golf ball viewed in the crossflow plane at: (a) $x/D=1.0$; (b) $x/D=1.5$; (c) $x/D=3.0$; $Re=1.1 \times 10^5$ ($Ut/D=18.8$).

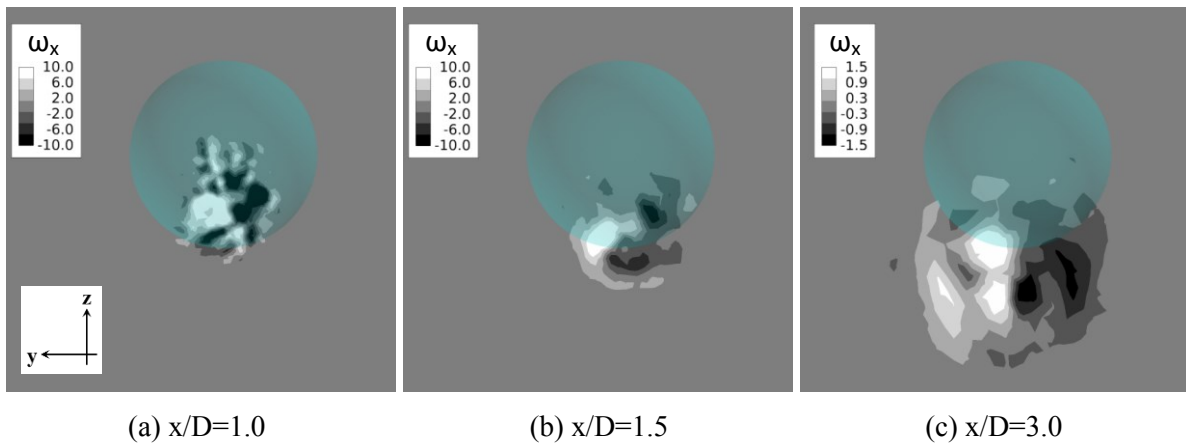


Fig.4-34 Streamwise vorticity component in the wake flow of the self-spinning smooth sphere viewed in the crossflow plane at: (a) $x/D=1.0$; (b) $x/D=1.5$; (c) $x/D=3.0$; $Re=1.14 \times 10^6$ ($Ut/D=6.2$).

Further insights into the differences in the wake structures between the two supercritical self-spinning cases are provided in Fig.4-33 and Fig.4-34 by the investigation of the streamwise vorticity component ω_x (normalized by multiplying D/U) visualized in the crossflow planes (normal to the freestream direction) located at $1.0D$, $1.5D$ and $3.0D$ from the center of the golf ball and the smooth sphere. As indicated in Fig.4-34, the twin vortices are clearly shown behind the smooth sphere at each of the three different locations, and they deviate further away from the x axis along the $-z$ direction due to the positive lift force as the flow travels downstream. In contrast, the vortices behind the golf ball show more random patterns and a more concentrated distribution around the geometry center at $x/D=1.0$, as

indicated in Fig.4-33 (a), while the twin vortices are detected at locations further downstream ($x/D=1.5$ and $x/D=3.0$), as indicated in Fig.4-33 (b) and Fig.4-33 (c). Similar to the smooth sphere, the twin vortices behind the golf ball deviate further away from the x axis along the -z direction due to the positive lift force as the flow travels downstream. Compared with the corresponding stationary case, one can observe that the twin vortices behind the self-spinning golf ball appear at a location further upstream, as indicated in Fig.3-25 (b) and Fig.4-33 (b).

Chapter 5: Conclusions

This chapter summarizes the main conclusions obtained in the present study and recommends the probable future work.

5.1 General conclusions

The present study has numerically investigated the aerodynamics of a golf ball around the drag crisis region by using large-eddy simulation method, and a direct comparison with a smooth sphere was made. Particular attention was focused towards investigating the underlying mechanism of drag reduction by golf ball dimples, the ordinary and negative Magnus effects on self-spinning golf balls, the lateral force variation on both stationary and self-spinning golf balls, and the transient features of golf ball aerodynamics.

For all the large-eddy simulations conducted in the present study, the dynamic Smagorinsky model was adopted for properly resolving the boundary layer flow. The arbitrary Lagrangian-Eulerian method was applied to impose the self-spinning motion on the golf ball, whereas for the smooth sphere, the self-spinning motion was imposed by adding an angular velocity on the geometry surface as a boundary condition. Triangular meshes were generated on the surfaces of both models, while prism layers were allocated along the normal-wall direction of the surfaces. The required grid resolution was estimated based on the laminar boundary layer thickness δ_B .

The drag crisis of the stationary golf ball was successfully reproduced in the present simulations. The results show that the drag crisis of the golf ball occurs in a visibly lower Reynolds number range when compared to the smooth sphere, which agrees very well with the previous experimental data^{3,4}. The detailed analysis on the local flow behaviors inside individual dimples reveals the mechanism responsible for the corresponding drag reduction of the golf ball. It is shown that the flow locally separates on the leading edges of some dimples when it passes over the golf ball surface in the supercritical regime. The locally detached shear layers quickly become unstable and oscillate considerably as they travel further downstream. Meanwhile, small-scale vortices are generated inside the individual dimples. As a result of the shear layer instability, the momentum in the near-wall flow increases, and with the increased momentum, the flow that reattaches on the trailing edges of the dimples is able to overcome the adverse pressure gradient more and travel further downstream, which consequently delays the full flow separation. A schematic diagram of the

local detachment and reattachment of the flow inside a dimple is provided in Fig.5-1. This mechanism is considered as the key factor that helps to reduce the drag coefficient of the golf ball at a lower Reynolds number when compared to the smooth sphere.

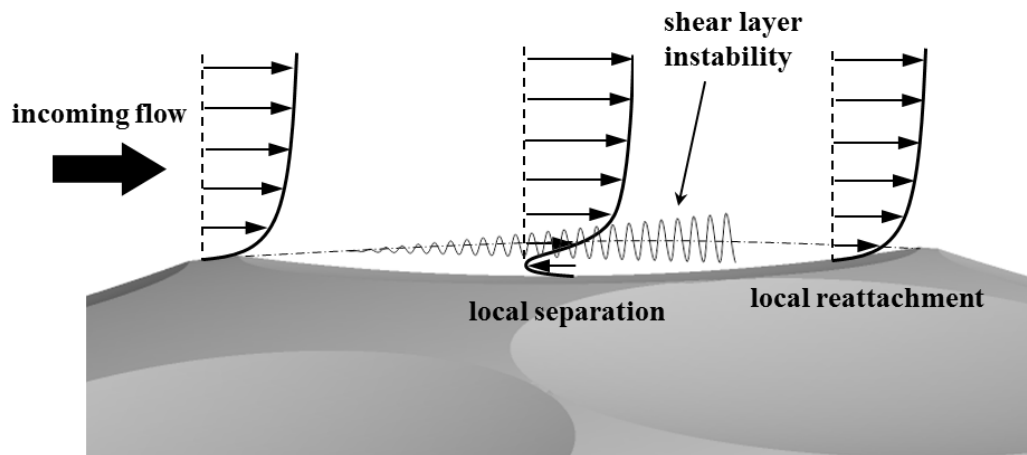


Fig.5-1 Schematic diagram of the mechanism of local flow separation and reattachment inside a golf ball dimple.

The investigation of the lateral force variation and wake flow structure for the stationary cases shows that for both the golf ball and smooth sphere in the subcritical regime, the lateral forces change irregularly with time for both the magnitude and direction. In addition, a large-scale wave motion is pronounced in the wake areas of both models, and the azimuthal position of the waviness-containing planes varies irregularly with time. The wavelengths of the wake structures behind both models are similar to each other, corresponding to their similar dominant frequencies of the lateral force oscillation. In the critical regime, the lateral forces acting on both models exhibit a larger oscillation magnitude when compared to the subcritical cases, and the directions of the lateral forces change irregularly with time. A larger wavelength is observed for the wave motion of the wake flow behind the golf ball, which relates to the lower dominant frequency of the lateral force oscillation of the golf ball when compared to the smooth sphere. In the supercritical regime, both models are subjected to a nonzero lateral force during a long time interval, and the lateral force direction exhibits a rotation trend with time about the streamwise axis that goes across the center of the golf ball/smooth sphere. However, the magnitude of the lateral force acting on the golf ball is visibly smaller when compared to the smooth sphere, which indicates a suppression of the lateral force for the golf ball. Corresponding to the differences

between the lateral forces, the wake structure behind the smooth sphere significantly deviates from the x axis, whereas the wake structure behind the golf ball stays approximately parallel to the x axis.

The ordinary Magnus effect and negative Magnus effect were successfully reproduced in the present simulations for both the self-spinning golf ball and smooth sphere. The results show that, for both models, the ordinary Magnus effect appears in the subcritical and supercritical Reynolds number regimes, whereas the negative Magnus effect appears in the critical Reynolds number regime. The mechanism of the ordinary/negative Magnus effect is directly associated with the boundary layer separations on the top side and the bottom side of the geometries. Particularly, in the present simulations, the top sides of both models rotate in the direction moving with the approaching flow, whereas the bottom sides of both models rotate in the direction moving against the approaching flow. In the subcritical and supercritical regimes, the boundary layers on the top side and bottom side exist in the same state (both laminar or both turbulent). As a result of the self-spinning motion, the near-wall flow gains momentum on the top side while it loses momentum on the bottom side. This further leads to the flow separating at a position further downstream on the top side than on the bottom side, which causes the pressure on the top side experiencing a steeper drop and a lower minimum value than the bottom side. This consequently gives rise to a positive Magnus force acting on both models. In contrast, in the critical regime, the boundary layer on the top side stays laminar whereas on the bottom side it becomes turbulent. This is attributed to the locally higher relative Reynolds number on the bottom side which makes the flow on this side more sensitive to perturbations and consequently promotes the laminar-turbulent boundary layer transition. As a result, the flow separates at a position further downstream on the bottom side than on the top side, which leads to a lower pressure on the bottom side than on the top side in the majority of angular positions. This consequently produces a negative Magnus force acting on both models.

The investigation of the lateral force variation and wake flow structure for the self-spinning cases shows that for both the golf ball and smooth sphere in the subcritical regime, the variation of the lateral force is more regular when compared to the stationary cases, and the lateral force oscillation is more dominant in the lift force direction than in the side force direction. In addition, a large-scale wave motion is pronounced in the wake areas of both models, and the wake structures in the near-wall regions are obviously deflected downwards in the lift force planes. The wavelength of the wake structure behind the golf ball is slightly larger than the smooth sphere, corresponding to the lower dominant frequency of the lateral

force oscillation of the golf ball. In the critical regime, the lateral force acting on the rotating golf ball experiences a visibly smaller oscillation when compared to the stationary case, whereas the lateral force acting on the rotating smooth sphere exhibits a considerable oscillation in the lift force direction. A large-scale wave motion is pronounced in the wake areas of both models, and the wake structures in the near-wall regions are obviously tilted upwards in the lift force planes. Similar to the rotating cases at the subcritical Reynolds number, the wavelength of the wake structure behind the golf ball is larger than the smooth sphere, relating to the lower dominant frequency of the lateral force oscillation exhibited in the golf ball case. In the supercritical regime, the variation of the lateral forces acting on both rotating models is more regular in terms of both the oscillation and direction when compared to the stationary cases. This reveals that the self-spinning motion helps to stabilize the lateral forces in the supercritical regime. However, it was found that the lift force acting on the rotating golf ball is about 40% smaller than the rotating smooth sphere, while the drag forces acting on these two models are similar to each other. This indicates a suppression of the lateral force in the rotating golf ball case, analogous to the stationary case in the same regime. A large-scale vortex shedding is pronounced in the wake areas of both models, and the wake structures behind both models are obviously deflected downwards. However, the progressive wave motion is no longer clearly observed in the supercritical regime.

5.2 Future work

For the next step of the present study, an investigation of the effects of different dimple patterns on the golf ball aerodynamics will be conducted. By comparing the aerodynamic performance between golf balls with different dimple patterns, insights into product optimization could be gained, which is one of the main concerns for a manufacturer.

Another probable extension of the present research is to predict the flying trajectory of a golf ball. Based on the ALE method adopted in the present study, a dynamic-aerodynamic coupling simulation could be conducted for a golf ball moving under real-life conditions, and the three-dimensional flying trajectory of the golf ball could be precisely computed.

References

1. Mehta, R.D., Pallis, J.M. (2001). Sports ball aerodynamics: effects of velocity, spin and surface roughness. *Minerals, Metals and Materials Society/AIME, Materials and Science in Sports (USA)*, 185-197.
2. Achenbach, E. (1972). Experiments on the flow past spheres at very high Reynolds numbers. *J. Fluid Mech.* 54, 565-575.
3. Bearman, P.W., Harvey, J.K. (1976). Golf ball aerodynamics. *Aeronaut. Q.* 27, 112-122.
4. Choi, J., Jeon, W., Choi, H. (2006). Mechanism of drag reduction by dimples on a sphere. *Phys. Fluids.* 18, 041702.1-041702.4.
5. Smith, C.E., Beratlis, N., Balaras, E., Squires, K., Tsunoda, M. (2010). Numerical investigation of the flow over a golf ball in the subcritical and supercritical regimes. *International Journal of Heat and Fluid Flow.* 31, 262-273.
6. Achenbach, E. (1973). The effects of surface roughness and tunnel blockage on the flow past spheres. *J. Fluid Mech.* 65, 113-125.
7. Magnus, G. (1853). Ueber die abweichung der geschosse, und: Ueber eine auffallende erscheinung bei rotirenden körpern. *Annalen der physik*, 164(1), 1-29.
8. Taneda, S. (1957). Negative magnus effect. *Reports of Research Institute for Applied Mechanics*, (20), 123-128.
9. Muto, M., Tsubokura, M., Oshima, N. (2012). Negative Magnus lift on a rotating sphere at around the critical Reynolds number. *Phys. Fluids.* 24, 014102.1-014102.15.
10. Kim, J., Choi, H., Park, H., Yoo, J. Y. (2014). Inverse Magnus effect on a rotating sphere: when and why. *Journal of Fluid Mechanics*, 754, R2, 1-11.

11. Beratlis, N., Squires, K., Balaras, E. (2012). Numerical investigation of Magnus effect on dimpled spheres. *Journal of Turbulence*, (13), N15, 1-15.
12. Achenbach, E. (1974). Vortex shedding from spheres. *J. Fluid Mech.* 62, 209-221.
13. Taneda, S. (1978). Visual observations of the flow past a sphere at Reynolds numbers between 10^4 and 10^6 . *J. Fluid Mech.* 85, 187-192.
14. Sakamoto, H., Haniu, H. (1990). A study on vortex shedding from spheres in a uniform flow. *Journal of Fluids Engineering.* 112, 386-392.
15. Constantinescu, G., Squires, K. (2004). Numerical investigations of flow over a sphere in the subcritical and supercritical regimes. *Phys. Fluids.* 16(5), 1449-1465.
16. Yun, G., Kim, D., Choi, H. (2006). Vortical structures behind a sphere at subcritical Reynolds numbers. *Phys. Fluids.* 18, 015102.1-015102.14.
17. Norman, A.K., McKeon, B.J. (2011). Unsteady force measurements in sphere flow from subcritical to supercritical Reynolds numbers. *Experiments in Fluids.* 51(5), 1439-1453.
18. Davies, J.M. (1949). The aerodynamics of golf balls. *Journal of Applied Physics.* 20, 821-828.
19. Kray, T., Franke, J., Frank, W. (2012). Magnus effect on a rotating sphere at high Reynolds numbers. *Journal of Wind Engineering and Industrial Aerodynamics*, 110, 1-9.
20. Norman, A.K., McKeon, B.J. (2011). The effect of a small isolated roughness element on the forces on a sphere in uniform flow. *Experiments in Fluids.* 51(4), 1031-1045.
21. Moin, P., Kim, J. (1997). Tackling turbulence with supercomputers. *Scientific American.* 276(1), 46-52.
22. Ferziger, J. H., and Peric, M. (2012). *Computational methods for fluid dynamics*. Springer Science Business Media.

23. Smagorinsky, J. (1963). General circulation experiments with the primitive equations: I. the basic experiment*. *Monthly weather review*, 91(3), 99-164.
24. Van Driest, E. R. (1956). On turbulent flow near a wall. *Journal of the Aeronautical Sciences*, 23(11), 1007-1011.
25. Germano, M., Piomelli, U., Moin, P., Cabot, W.H. (1991). A dynamic subgrid-scale eddy viscosity model. *Phys. Fluids A*. 3(7), 1760-1765.
26. Lilly, D. K. (1992). A proposed modification of the Germano subgrid-scale closure method. *Physics of Fluids A: Fluid Dynamics (1989-1993)*, 4(3), 633-635.
27. Constantinescu, G. S., and Squires, K. D. (2003). LES and DES investigations of turbulent flow over a sphere at $Re= 10,000$. *Flow, Turbulence and Combustion*, 70(1-4), 267-298.
28. Constantinescu, G., Chapelet, M., Squires, K. (2003). Turbulence modeling applied to flow over a sphere. *AIAA journal*, 41(9), 1733-1742.
29. Amsden, A. A., Harlow, F. H. (1970). A simplified MAC technique for incompressible fluid flow calculations. *Journal of Computational Physics*, 6(2), 322-325.
30. Hirt, C. W., Amsden, A. A., Cook, J. L. (1974). An arbitrary Lagrangian-Eulerian computing method for all flow speeds. *Journal of Computational Physics*, 14(3), 227-253.
31. Cheng, S. Y., Tsubokura, M., Nakashima, T., Nouzawa, T., Okada, Y. (2011). A numerical analysis of transient flow past road vehicles subjected to pitching oscillation. *Journal of Wind Engineering and Industrial Aerodynamics*, 99(5), 511-522.
32. Schlichting, H. (1955). *Boundary Layer Theory*. McGraw-Hill, New York.

33. Tsubokura, M., Nakashima, T., Kitoh, K., Sasaki, Y., Oshima, N., Kobayashi, T. (2009). Development of an unsteady aerodynamic simulator using large-eddy simulation based on high-performance computing technique. *SAE Technical Paper*. No.2009-01-0007.
34. Wieselsberger, C. (1922). Weitere Feststellungen über die Gesetze des Flüssigkeits und Luftwiderstandes. *Phys. Z.* 23, 219-224.
35. Hunt, J.C.R., Wray, A.A. and Moin, P. (1988). Eddies, streams, and convergence zones in turbulent flows. *Center for Turbulence Research Report*. CTRS88, 193-208.